POLITECNICO DI MILANO

Corso di Laurea in Ingegneria per l'Ambiente e il Territorio

A MULTI-SENSOR APPROACH FOR SURFACE SOIL MOISTURE ESTIMATION

A FIELD STUDY IN EASTERN AUSTRALIA

Relatore: prof. Giorgio Guariso

Correlatore: Dr. Jeffrey Walker

Tesi di laurea di:

Viviana Maggioni	Matr. 666705
Valerio Paruscio	Matr. 666972
Marco Rinaldi	Matr. 666899

Anno accademico 2004/2005

ACKNOWLEDGMENT

La storia di questa tesi ha dell’incredibile, nata in una notte di primavera durante un viaggio organizzato dal Politecnico in Sardegna con tutti i nostri compagni di corso. Festa sulla spiaggia e menti rallegrate dal mirto locale.

“Allora dove si fa la tesi?”

“Mah, non saprei…” (scetticismo)

“Ci vorrebbe un paese anglofono e magari caldo…” (entusiasmo)

“Australia?” (ilarità)

“Andata” (assecondante)

Passano pochi giorni e ci presentiamo nell’ufficio del professor Guariso, cui va il nostro primo grazie, per verificare se effettivamente l’affair è fattibile. Sembra di sì...

Con una mail ci proponiamo al dipartimento di ingegneria ambientale della University of Melbourne: il Dr. Walker (secondo grazie) cerca “volontari” per un progetto che prevede un mese di rilevamento dati nelle sperdute campagne australiane. E’ nostro!

Così lasciamo l’Italia portando nel nostro bagaglio molte aspettative, che non verranno affatto deluse.

A Melbourne siamo stati adottati dall’intero dipartimento, non ci scorderemo mai dell’accoglienza e dell’ambiente così “friendly” che ci ha permesso di riuscire a portare a termine il nostro progetto, aiutandoci e sostenendoci quando tutto sembrava appeso ad un filo. Un grazie speciale a Rocco, per tutto il tempo che ci ha dedicato e per le folli discussioni sulla soil moisture davanti alle care “jag”; a Peru perché stampando questa tesi ci ha permesso di essere qui oggi; a tutti gli amici che in questi anni ci hanno accompagnato rendendo tutto così unico, ognuno col suo viaggio ognuno diverso.

Ai nostri genitori e familiari un grazie di cuore per averci sempre sostenuto nell’inseguire i nostri pazzi sogni.

INDEX

1

INTRODUCTION

Soil moisture is a key variable controlling the exchange of water and heat energy between the land and the atmosphere through evaporation and plant transpiration. As a result, soil moisture plays an important role in development of weather patterns and extreme-event forecasting such as floods and landslides. Measurements of soil moisture provide also information for agriculture and it can be used to infer water stress for irrigation decisions, to aid in yield estimation and to assess drought conditions.

Information on soil moisture may be obtained from three main sources. First, ground-based soil moisture profile measurements may be made continuously at individual points. Unfortunately, these are rarely representative of the spatial distribution, and so they are unsuitable for mapping of large areas. Second, remote sensing may be used to measure soil moisture in the top few centimeters for areas with low to moderate vegetation cover but do not provide any direct information on root zone soil moisture. Third, land surface models may be used to predict the spatial and temporal variation of soil moisture (near-surface and root zone) but those estimates suffer from inadequate model physics, parameter estimates, and atmospheric forcing data. Clearly these different approaches are complementary, and so our approach has been to utilize all three sources of data, by assimilation of the remotely sensed near-surface soil moisture measurements into a land surface model, and relying on the point measurements for verification. While current progress on this approach has been good, its application has been confined to large scale estimates with little appropriate data available for assimilation and/or field verification. Therefore appropriate observation and verification data need to be collected to mature this technology.

Over the past two decades there have been numerous near-surface soil moisture remote sensing studies, using visible, thermal infrared (surface temperature) and microwave (passive and active) electromagnetic radiation. Passive microwave soil moisture measurement has been the most promising technique in this area, due to its all-weather capability, its direct relationship with soil moisture through the soil's dielectric constant, and a reduced sensitivity to land surface roughness and vegetation cover. Due to the long wavelengths required for soil moisture remote sensing, space-borne passive microwave radiometers (both current and planned) have a coarse spatial resolution, being on the order of 25 to 50 km, but have a frequent temporal resolution of 1 to 2 days. While this spatial resolution is appropriate for some broad scale applications, it is not useful for small scale applications such as on-farm water management, flood prediction or meso-scale climate and weather prediction. Thus methods need to be developed for reducing these large scale measurements to a smaller scale. This may ultimately be possible using information from other types of higher resolution sensors (e.g. thermal and visible imagery from the MODerate resolution Imaging Spectrometer (MODIS) or LANDSAT Thematic Mapper), but any downscaling approaches must first be developed and validated with direct high resolution passive microwave measurements and such data must be collected.

The aim of this study is the analysis of soil moisture from L-band passive microwaves remote sensing observations. Ground and airborne data collected during the field campaign NAFE 05, conducted in New South Wales, Australia, in November 2005 are used for the purpose.

Brightness temperature, measured by the Polarametric L-band Radiometer of the aircraft, represents the input for a physically based model that computes as ancillary information soil temperature and vegetation coverage to retrieve soil moisture. Thermal Infrared Radiometers at ground level were used to obtain a relationship between surface and deep soil temperature. A digital Thermocam mounted on the airplane provides thermal images of the area of interest. The estimation of the vegetation parameters was performed using both ground data and visible, near-infrared (NIR), short-wave infrared (SWIR) bands of Aqua-Moderate Resolution Imaging Spectroradiometer (Aqua-MODIS). Vegetation indices based on these bands were evaluated by computing their correlations with ground measured vegetation water content.

This study presents a preliminary analysis of the PLMR derived soil moisture product at 250m resolution across a 2000ha area. This is the first airborne remote sensing study to both provide such high resolution soil moisture data and to take this multi-sensor approach to soil moisture retrieval.

Maps showing the outputs of the model have been compared to the ground measurements to outline the spatial and temporal variability of soil moisture and to test the reliability of the airborne data.

The performance of the model was more than satisfactory: results indicate a very good agreement of the retrieved and measured soil moisture spatial distribution and do not present any systematic overestimation or underestimation. Therefore, the results are encouraging toward the use of PLMR-derived soil moisture for further studies.

1.1 Structure of the work

In chapter 2 the field campaign undertaken in November 2005 in Australia is described.

Chapter 3 presents the physically based model to retrieve soil moisture from microwave L-band observation and the following three chapters describe the main inputs of the algorithm.

The issue of chapter 4 is the calibration of the microwave radiometer, mounted on the aircraft, to obtain correct values of brightness temperature.

In chapter 5, a method to estimate the temperature of the first 5cm of soil from thermal infrared observation is presented.

Chapter 6 illustrates a relationship to obtain the vegetation water content from commonly available remote sensing data.

Chapter 7 shows the procedure to uniform the information from the three previous chapters and presents the results of the study. Furthermore, observed and predicted soil moisture values are compared and sensitivity analysis of some parameters of the model is performed.

Chapter 8 summarises the conclusions of this study.

2

THE FIELD CAMPAIGN

This chapter describes the field campaign NAFE 2005 (National Airborne Field Experiment, http://www.nafe.unimelb.edu.au), conducted in New South Wales, Australia, during the month of November 2005. An overview of the project and a description of the catchment of interest are shown at the beginning of the chapter. Ground sampling strategy and airborne monitoring are then described in all their details, illustrating the data collected and the instruments and devices that were used.

The purpose of the project NAFE is to map near-surface soil moisture at different resolutions making use of passive microwave airborne and spaceborne remote sensors. The ultimate goal is to be able to provide reliable near-surface soil moisture observations at the paddock scale globally. Specifically, this involves capitalizing on future remote sensing missions such as ESA's Soil Moisture and Ocean Salinity (SMOS) satellite scheduled for launch in 2007 and NASA's Hydrospheric States (Hydros) scheduled for launch in 2010.

2.1 Overview and Objectives

Internationally, there has been a significant decline in the number of gauged basins over recent years, yet the demand for hydrologic prediction is greater than ever, particularly as we enter an era of uncertainty due to global climate change. The potential for reliable hydrologic prediction in ungauged basins exists only through an increasing ability to remotely sense land surface states, fluxes, and parameters that impact on basin condition. For instance, it is now possible to measure evapotranspiration rates that determine soil moisture and baseflow, nearsurface soil moisture content that controls rainfall partitioning into infiltration and runoff, snow water equivalent of the snow pack that determines spring-time runoff, vegetation parameters such as leaf area index and greenness that control evapotranspiration, land surface elevation and canopy height that impact on runoff routing and evapotranspiration, and so on.

However, there are still many unanswered questions that need to be addressed, including validation of data products from new sensors, maturing of retrieval algorithms, developing techniques for downscaling, and merging remote sensing data with model predictions through the process of data assimilation.

To answer these important questions it is essential that field campaigns with coordinated satellite, airborne and ground-based data collection be undertaken, giving careful consideration to the diverse data requirements for the range of questions to be addressed.

While there is a clear emphasis on soil moisture remote sensing in the NAFE experiment, the nature of the airborne and the collected supporting data made this campaign applicable to a wide range of environmental remote sensing disciplines and applications.

This coordinated field experiment took place in November 2005 (NAFE ’05), with participants from the University of Melbourne, University of Newcastle, Airborne Research Australia, and several European universities and organizations including the

European Space Agency (ESA), undertaking research on soil moisture, flood forecasting, carbon budgets and ecohydrology. This project is complementary with others around the world, including the series of SGP (Southern Great Plains) and SMEX (Soil Moisture Experiment) campaigns in the United States and coSMOS (Campaign for validating the Operation of SMOS) activities in Europe (http://www.esa.int/esaLP/SEMMM95Y3EE_index_0.html).

2.1.1 Requirements

Future developments should carefully consider different ground based instruments and data types (Fig. 2.1):

- long-term observation of soil moisture profiles and associated meteorological data for evaluation of derived root zone soil moisture
- extensive ground-based near-surface soil moisture and temperature data at a range of spatial scales during airborne campaigns for scaling studies, aircraft and satellite verification and algorithm development
- continuous near-surface soil moisture, soil temperature, and thermal infrared point observation for relating air-to-ground measurements throughout the day
- vegetation biomass/water content and dew observation for determining vegetation and dew effects.

There are also a number of airborne data requirements (Fig. 2.1) to be considered:

- airborne passive microwave, thermal and NDVI data at a range of scales for algorithm development and satellite verification
- airborne lidar data for accurate topography and incidence angle information
- digital photography for land use and land cover information

- airborne observations coincident with ground observations and made as early in the morning as possible to ensure that soil and vegetation temperatures are more closely aligned and have a more uniform soil temperature profile
- airborne observations at a range of altitudes (625ft to 10,000ft) to achieve a range of ground resolutions (62.5m to 1000m for passive microwave and 1m to 20m for thermal and NDVI) for scaling, algorithm development and satellite verification.

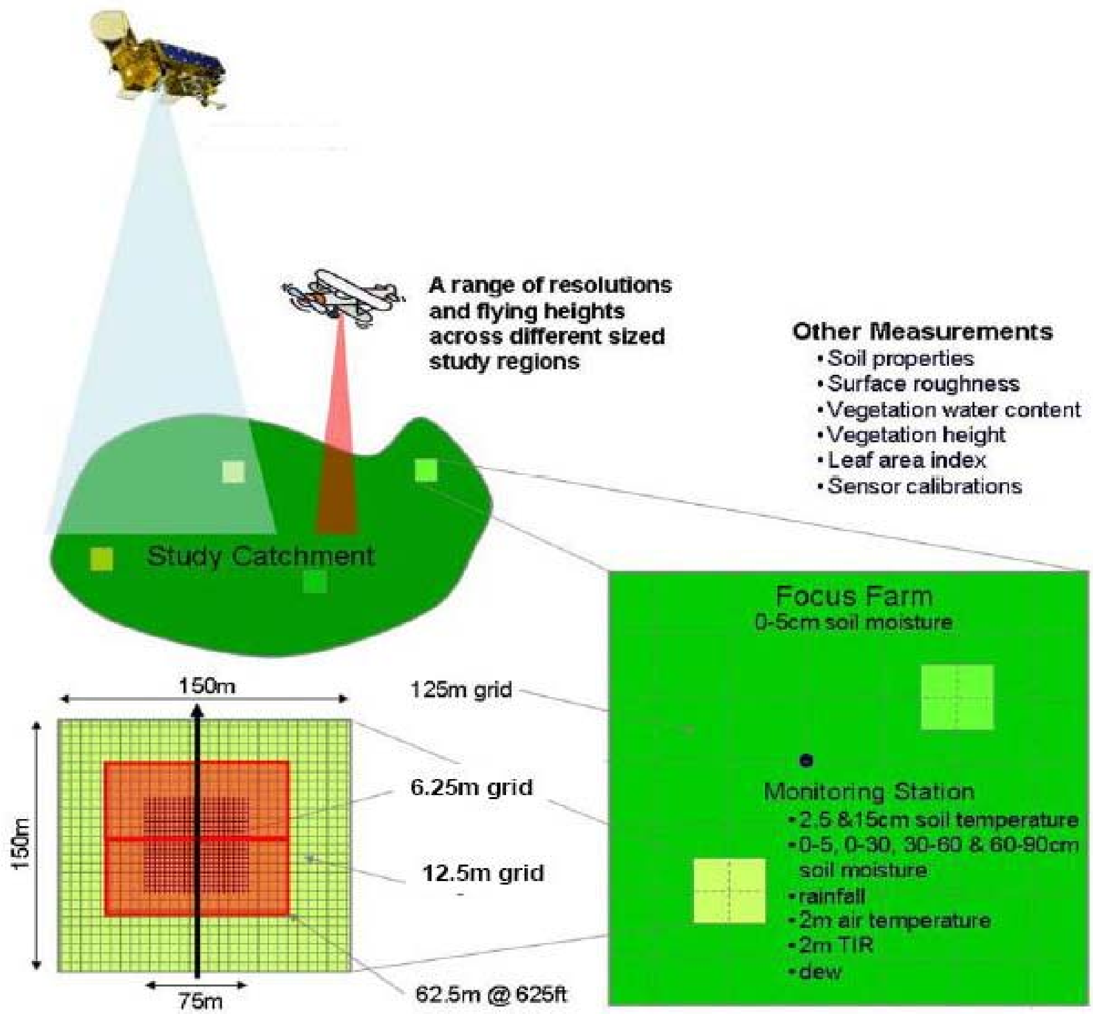

Figure 2.1: Schematic experimental design

2.1.2 NAFE Objectives

The scientific objectives and data requirements of NAFE ’05 have been met by coordinating an aircraft remote sensing campaign with a ground data collection campaign. Furthermore, all collected data supported measurements taken from various spaceborne remote sensing platforms overpassing the study area.

The aircraft remote sensing campaign made use of a small environmental aircraft equipped with passive microwave, infrared and visible sensors to map the whole study area. The characteristics of such sensors in terms of spectral range, incidence angle and field of view are comparable with those onboard various existing and future satellite remote sensing missions. This allows comparability between spaceborne and airborne measurements and therefore ensures applicability of the outcomes of NAFE ’05 to future spaceborne missions. In order to collect data at various resolutions and instrument configurations (in terms of incidence angle), the aircraft flew at different altitudes, resulting in a variety of ground spatial resolutions ranging from satellite-footprint scale down to farm and paddock scale.

Airborne and spaceborne observations have been supported by ground data collected during the one-month long campaign. Ground measurements include near-surface soil moisture for direct validation of the passive microwave remote sensors observations, as well as ancillary data such as vegetation biomass, land cover information, soil temperature and surface roughness. Ground sampling was coordinated with aircraft and satellite overpasses times to minimize temporal lag between observations.

The study area of NAFE ’05 was the Goulburn River catchment, a subhumid to temperate area located in south-eastern Australian, approximately 300km north-west of the city of Sydney. The main study area included a large portion of the northern part of the Goulburn Basin. Two focus areas delimited by the Merriwa River and Krui River catchment boundaries have been selected for more detailed analysis. Within these areas eight farms have been chosen as the object of intensive farm-scale ground and aircraft monitoring (“Farm scale sampling areas”). The ground crew was based in the township of Merriwa, located in the heart of the study area, and set off from there for the daily sampling. The air crew was based in Scone, near the airport used for the aircraft operations.

2.2 River Catchments

The 6540km² Goulburn River experimental catchment is a tributary to the Hunter River in New South Wales, Australia (Fig. 2.2). This subhumid to temperate catchment extends from 31°46’S to 32°51’S and 149°40’E to 150°36’E, with elevations ranging from 106m in the floodplains to 1257m in the northern and southern mountain ranges. The Goulburn River runs generally from west to east, with tributaries from the north and south, meaning the catchment is dominated by easterly and westerly aspects.

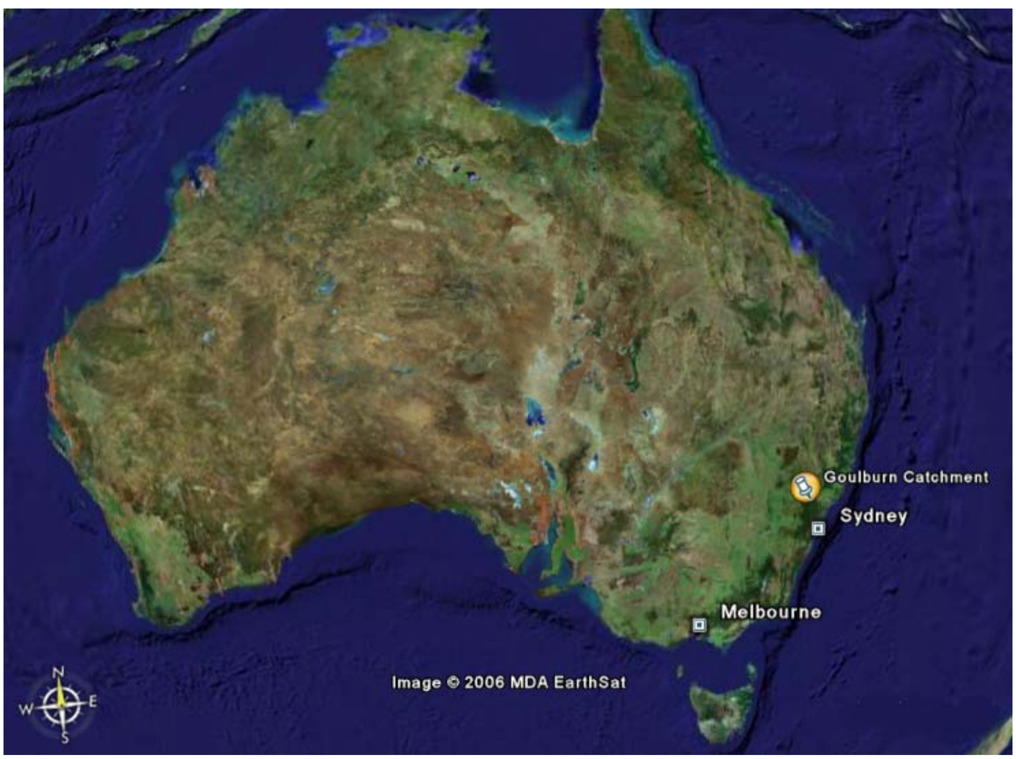

Figure 2.2: Location of the Goulburn Catchment, Australia

The catchment (Fig. 2.3) had two more intensively monitored subcatchments, the Krui River (562km²) and Merriwa River (651km²) in the northern half of the catchment. Additionally, a densely monitored 175ha micro-catchment is located on a property called "Stanley", located in the lower reach of the Krui River catchment.

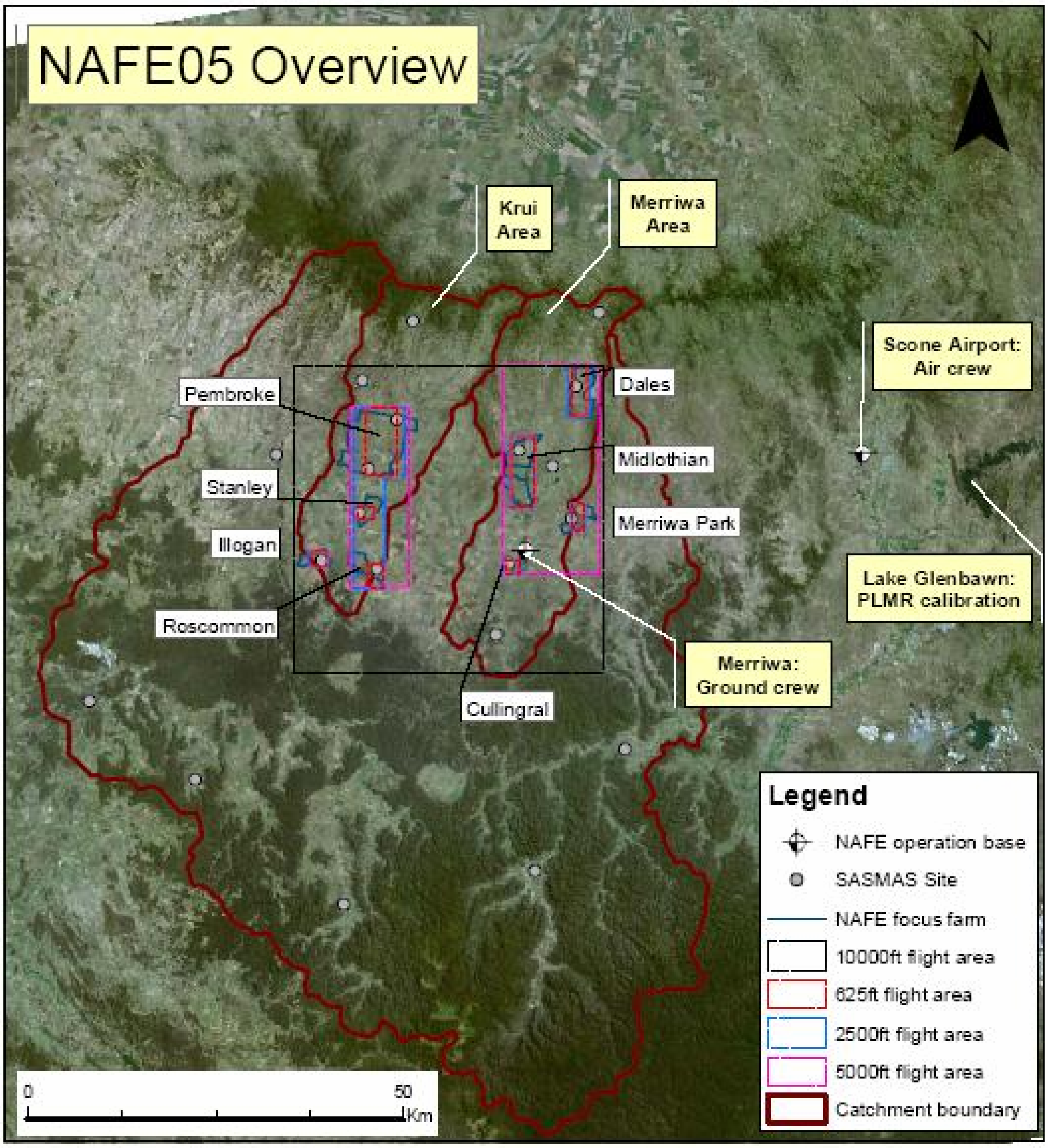

Figure 2.3: Overview of the study area

2.2.1 Climate

The general climate within the region can be described as subhumid or temperate, with significant variation in the annual rainfall throughout the catchment. While the average annual rainfall (Fig. 2.4) in most of the catchments is approximately 700mm, it varies from500 mm to 1100mm depending on altitude. Major rainfall events generally occur in October and November with an average monthly precipitation of 50mm, while the monthly average precipitation in July is 40mm.

Monthly mean maximum temperatures reach approximately 30°C in summer and 14°C in winter, with minimum values of 16°C and 2°C, respectively. Except for elevated areas, frost is unlikely to occur during daytime in winter, but night time minimum temperatures in winter are frequently less than 0°C.

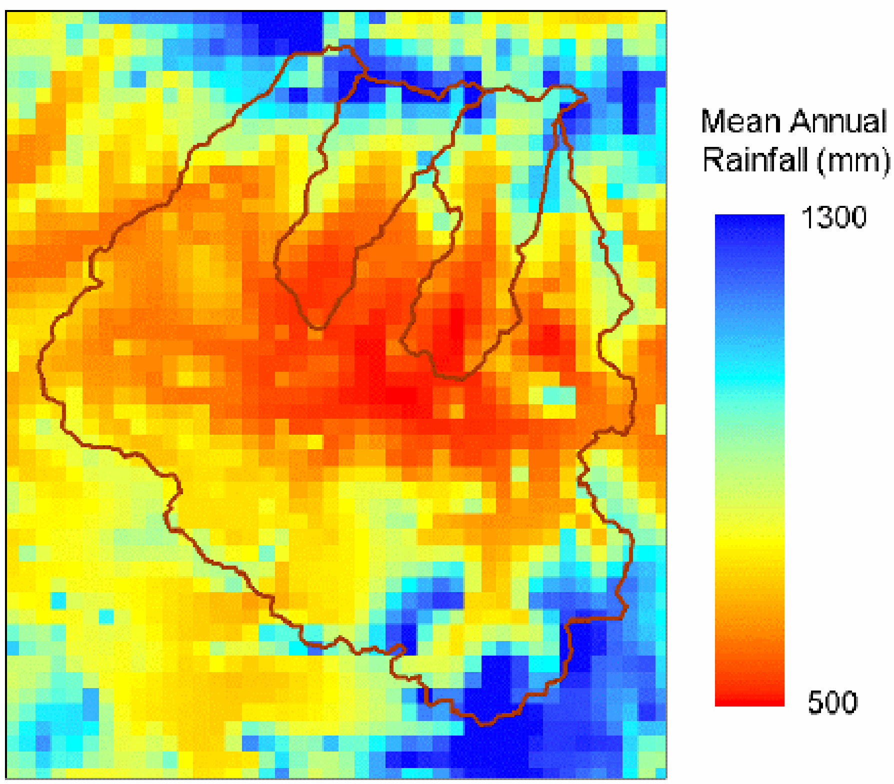

Figure 2.4: Map of the mean annual rainfall for the Goulburn Catchment

2.2.2 Geology and Soils

The geology of the Goulburn River catchment can be distinguished into two types: the northern which is predominantly Tertiary basalt, a product of Cainozoic volcanism which took place throughout much of eastern Australia, and the southern which is dominated by rocks of the Triassic age laid down as sediments in lagoons and consisting of sandstone, conglomerate and shale. The regions geomorphology is largely dependent on its geological and climatic history with four main types of country identified; the Liverpool Range and Merriwa Plateau in the north and the Central Goulburn Valley and Southern Mountains in the south. The actual study area falls in the northern part of the Goulburn catchment, across the Liverpool Range and Merriwa Plateau. Situated at the northern extent, the Liverpool ranges are characterized by a rugged and basaltic landscape. The area rises over 1200m above sea level, and localized plateaus exist despite the characteristic rugged topography. The Merriwa Plateau is located south of the Liverpool Range, presenting a rolling and hilly basaltic topography. Its elevation ranges between 450m to the north and 300m to the south.

The NAFE ’05 study area covers mainly the Merriwa Plateau and the southern fringes of the Liverpool Ranges. The northern part of the NAFE ’05 study area is therefore characterized by black basalt derived cracking clays, while the very southern part of the study area is characterized by sandstone derived soils. Red basalt derived clays are also existent in southern regions of the study area.

2.2.3 Vegetation

Much of the original vegetation in the northern part of the Goulburn catchment has been cleared, the extent of which has largely been influenced by topography and soil type.

In the north where the terrain is rugged (the Liverpool Range), accessibility is restricted and the area has thus remained highly vegetated. To the south, clearing has been more extensive due to the rolling to hilly terrain ensuring greater accessibility (the Merriwa Plateau). Grazing and cropping activities dominate cleared areas, due to the high fertility of basaltic soils. The sandstone derived soils to the far south are largely uncleared as they are less fertile and productive.

2.3 Ground Monitoring

During the 4 week experiment, ground crew has been organized into four teams of four people, each team acting independently within the daily schedule. Each team has been assigned two focus farms, one within the Krui and one within the Merriwa sub-catchments.

The ground component of the NAFE ‘05 field campaign consists of four aspects:

1. Network of continuous soil moisture profile monitoring stations;
2. Supplementary monitoring stations;
3. Spatial soil moisture mapping;
4. Supporting data.

2.3.1 Soil Moisture profile station

The soil moisture and climate monitoring sites existing within the Goulburn River experimental catchment form the basis of all ground based monitoring activities. These monitoring sites have recently been upgraded with telemetry systems, Stevens Water HydraProbe® sensors for top 5cm soil moisture (inserted vertically from the soil surface) and tipping bucket rain gauges. Eight focus farms for detailed measurements were chosen within the Krui and Merriwa sub-catchments according to spatial distribution and characteristics of farms hosting these stations. As the dominant landuses are grazing and cropping, this region is very suitable for soil moisture remote sensing studies due to the moderate vegetation cover. Table 2.1 summarizes the characteristics of each farm.

Table 2.1: Characteristics of the NAFE study farms

Farm name	Area (ha)	Topography	Landuse	Soils
Pembroke	6400	Hilly/Gently rolling	• Grazing • Cropping	Black basaltic clays
Stanley	720	Hilly	• Grazing	Black basalts on flat red basaltic clays on crests
Roscommon	940	Flat/Gently Rolling	• Grazing	Red basaltic clays and sandy soils
Illogan	560	Flat/Gently rolling	• Crop (Barley, Oats, Wheat)	Black basaltic clays with patches of red basaltic clays
Dales	1500	Flat/Hilly	• Grazing	Black basaltic clays
Midlothian	2000	Flat/Hilly	• Grazing • Crop(Sorghum, Lucerne, Wheat)	Black basaltic clays
Merriwa Park	750	Hilly	• Grazing • Crop (Wheat)	Black basaltic clays
Cullingral	220	Hilly	• Crop(Wheat, Lucerne)	Black basalticclays

2.3.2 Supplementary Monitoring Stations

A total of eight of the existing monitoring stations (one at each of the eight focus farms) has been supplemented with additional sensors for the duration of NAFE '05. The primary purpose of this supplementary monitoring was to:

1. provide information on near-surface soil temperature profiles;
2. provide information on leaf wetness in response to dew and precipitation;
3. develop relationships between thermal infrared observations and near-surface soil temperature.

To capture the relevant information, there were nominally:

- four stations with thermal infrared radiometers (Two Ahlborn Thermalert TX® and two Everest Interscience Inc.® Infrared Temp Transducers, Model 4000, Fig. 2.5) duplicate soil temperature sensors at 1cm, 2.5cm and 4cm (Unidata® 6507A/10 sensors), and leaf wetness sensors (Measurement Engineering Australia 2040®);
- two stations with single soil temperature sensors at 1cm, 2.5cm and 4cm, and leaf wetness sensors;
- two stations with single soil temperature sensors at 1cm, 2.5cm and 4cm (Fig.2.6);
- one station with 4 Unidata® 6507A/10 thermocouples attached to a rock (at Stanley farm).

This supplementary monitoring were in most cases installed "within" the enclosure at existing monitoring station sites. In particular cases, they were installed at nearby locations to capture land cover requirements not met at the existing sites; specifically for bare soil and at some crop sites.

Figure 2.5: Thermal infrared radiometer

Figure 2.6: Soil temperature sensors at 1cm, 2.5cm, 4cm

2.3.3 Regional Scale Sampling

Regional ground sampling of near-surface soil moisture have been undertaken using iPAQ based HydraProbe systems at predefined GPS-located points approximately 1km apart (Fig.2.7).

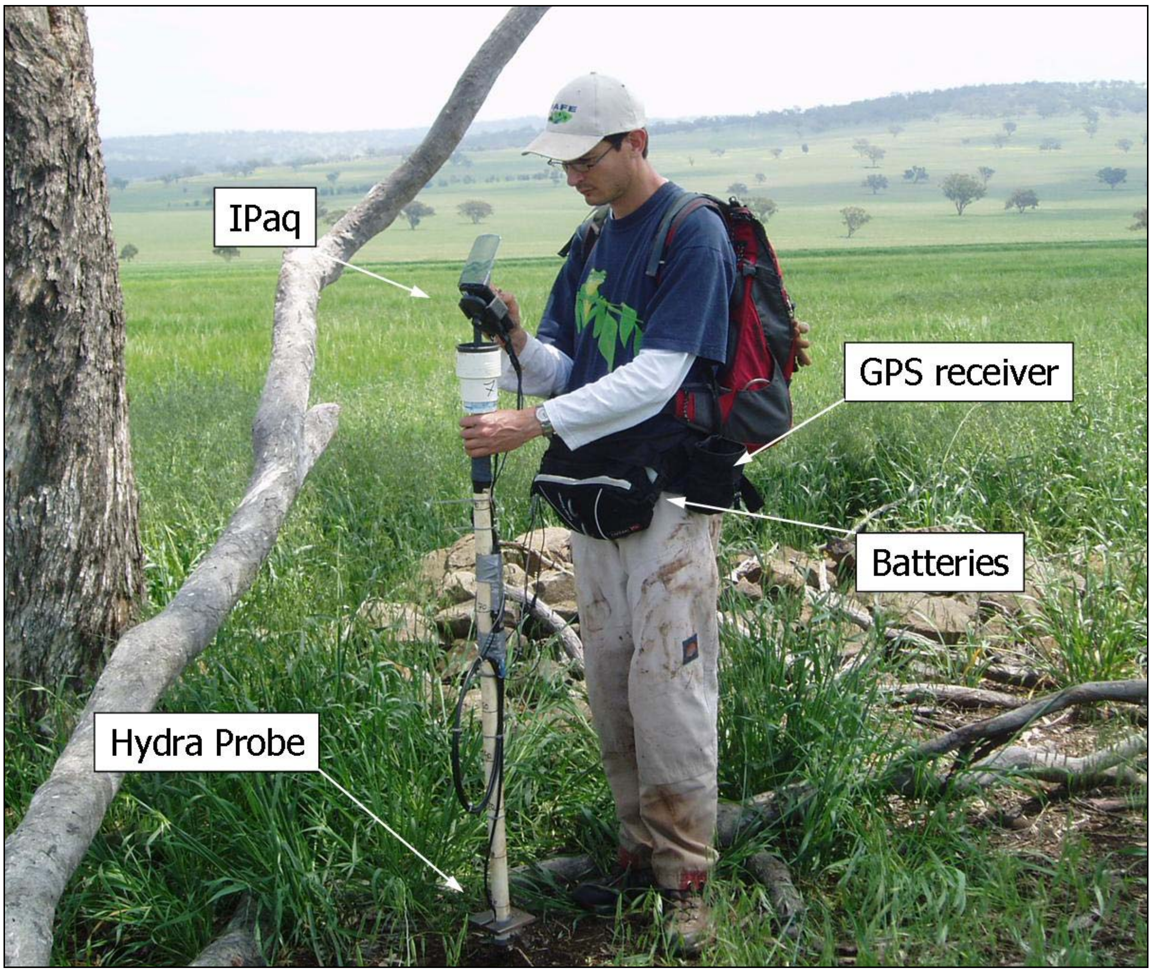

Figure 2.7: Set up of a soil moisture measuring unit

Regional scale sampling occupied an entire day once per week. Concurrently with soil moisture measurements, teams collected the following supporting data across both focus farms in their responsibility during regional sampling days:

- Gravimetric soil moisture samples (also used for soil texture);
- Vegetation biomass samples;
- Vegetation type characterization;
- Land use classification;
- Crop height measurements;
- Leaf wetness observations.

The following variables have been measured once only by each team for both farms, with instrumentation and/or personnel rotated between farms as necessary:

- Surface roughness measurements;
- NDVI measurements;
- Surface rock cover estimation.

2.3.4 Focus Farm measurements

The purpose of farm scale sampling is to provide ground soil moisture and supporting data for verification of the aircraft soil moisture, soil temperature and vegetation mapping at different ground pixel resolutions. Near-surface soil moisture has therefore been measured across the focus farms concurrently with aircraft overpasses at a range of spatial scales. The objective was to cover as much of the farm extent and surface conditions present in the area as possible in a single day, with a combination of spatial resolutions.

Soil moisture measurements have been taken at many locations within the farm at various resolutions (500m, 250m, 125m and 62.5m), covering as much as possible of the range of land use, topographic, soil type and soil wetness conditions present across the farm.

Furthermore, at each farm a small area of 150m by 150m size was the focus of very intensive soil moisture sampling (12.5m and 6.25m).

The 150m x 150m areas ("high resolution" areas) have been sampled at very high resolution, in order to provide highly detailed ground information on the representativeness and variability expected from point soil moisture and vegetation biomass measurements.

Teams also collected the following supporting data at the focus farm on each farm sampling day:

- Gravimetric soil moisture samples;
- Vegetation water content samples;
- Leaf wetness observations and dew amount.

2.3.5 Supporting Data

A number of auxiliary data sets are needed together with soil moisture in order to characterize the surface conditions within the study area. This information is necessary to provide auxiliary data required to model the soil microwave emission and to calibrate the ground sensors that will be used during the campaign.

Thermogravimetric soil moisture samples

Volumetric samples of soil have been collected across the study area for both soil textural analysis and calibration of the Stevens Water HydraProbes®.

These volumetric samples (collected with a sampling ring for the same soil measured with the HydraProbe) have been dried in ovens at the end of each day to calculate the gravimetric water content and the bulk density. The volumetric water content has been compared with HydraProbe measurements taken at the same locations. These samples covered a wide range of soil types and wetness conditions, providing a calibration equation.

Vegetation biomass and water content

The amount of vegetation biomass (Kg/m^2) and vegetation water content (kg of water/ m^2) present above the soil surface strongly affect the microwave emission observed.

Information on the spatial and temporal variation of these two quantities is needed for microwave emission modeling, so that relationships with infrared and visible remote sensing observations can be established. An overview of the sampling approach is as follows:

1. During regional sampling days:
   - A total of 16 vegetation biomass "quadrant" samples have been collected on a grid across the high resolution area on the all farms in weeks 1 and 3. A quadrant of 0.5m × 0.5m was used to obtain these samples (Fig. 2.8). They gave an estimate of spatial variability in vegetation biomass and water content for a specific vegetation type.
   - Two vegetation biomass "quadrant" samples have been collected across each farm, with the aim of collecting at least one sample for every land cover class. Sampling locations were the same for all four regional sampling days so they could be used to assess temporal variation in vegetation biomass and water content.
2. During farm scale sampling days:
   - Two vegetation water content "grab" samples have been collected for the farm reference vegetation at the end of the day. Sampling location and vegetation type remained the same for all the sampling days. These samples

gave an estimate of temporal variability in vegetation water content for specific vegetation types.

- Information about the plant height, using scale on HydraProbe pole was collected.

Figure 2.8: The vegetation sample quadrant

Vegetation type

This information is important for the analysis of visual and infrared remote sensing observations, as well as general site characterization. Dominant vegetation type has been recorded at each sampling site using a predefined list of vegetation types.

Land use and classification

Land use is a useful information that supports the interpretation of remotely sensed data of various nature. It is therefore important to characterize the main land uses in the study area, to complement land use mapping obtained from satellites like Landsat. Land uses has been characterized by visual observation during ragional sampling days, assigning every area sampled to one of the following subclasses (selected as the predominant land use classes in the region)

1. Native pasture
2. Improved pasture
3. Agricultural land: Fallow
4. Agricultural land: Wheat
5. Agricultural land: Lucerne
6. Agricultural land: Oats
7. Agricultural land: Barley
8. Forest land
9. Urban
10. Open woodland

Normalized Difference Vegetation Index (NDVI)

NDVI is a measure of the green, leafy vegetation density or the lushness of vegetation, and is a function of the difference between the visible and near-infrared sunlight that reflects off the vegetation. Ground measurements of this parameter can be used to verify satellite and aircraft observations. Measurements of NDVI have been taken at 50m spacing at the Hi-res areas of each farm with a Model 100BX Radiometer, a four-channel instrument, described in chapter 6 (Fig. 2.9).

Figure 2.9: Model 100BX Radiometer

Surface Roughness

Surface roughness affects the microwave emission from the soil by effectively increasing the surface area of electromagnetic wave emission. Although its effect on observations at L-band frequency has been shown to be very poor, it is important to characterize the spatial variation of this parameter across the different land cover types. It has been estimated once only during the campaign at four locations on each farm in the two orientations North-South and East-West to capture the different roughness characteristics according to land cover type. Measurements have been made using a 1 m long drop pin profiler with pin separation of 25 mm (Fig. 2.10).

Figure 2.10: The pin profiler

2.4 Airborne Monitoring

Airborne measurements have been made using the small, low-cost, two-seater motor glider from the Airborne Research Australia national facility called Small Environmental Research Aircraft (SERA), together with the Polarimetric L-band Multibeam Radiometer and thermal imager. This new infrastructure allowed, for the first time, very high resolution passive microwave (~50m) and land surface skin temperature (~1m) observations to be made across large areas.

There is no other capacity world-wide to make such high resolution measurements together with a range of other supporting data including a first-last return lidar, NDVI scanner and 11MegaPixel digital camera.

2.4.1 Instruments

The PLMR measures both V and H polarizations using a single receiver with polarization switch at incidence angles +/–7°, +/–21.5° and +/–38.5° in either across track (pushbroom) or along track configurations. The beamwidth is 17° resulting in an overall 90° field of view. The instrument has a frequency of 1.413 GHz and bandwidth of 24MHz

The thermal imager is a FLIRTS ThermaCam S60 with spectral range 7.5 to 13µm, accuracy +/–2°C or +/– 2% of reading and thermal sensitivity of 0.08°C. It has an 80° × 60° FOV lens with 1.3mrad IFOV, resulting in approximately 1m data from a 150m flying height.

More observations have been collected using a TSLS AWI/ARA Trispectral line scanner, a Canon EOS-1DS 11MegaPixel digital camera and a laser (near infrared) scanner.

2.4.2 Flight plans

Flight routes and coverages at different altitudes have been optimized in order to meet a number of objectives and logistic constraints. These objectives included:

- to cover as much of the study area at multiple ground resolutions during the campaign so as to obtain spatial soil moisture patterns at different scales for an extensive area (Fig.2.11);
- to map the same area at multiple ground resolutions within the same day to avoid so much as possible temporal differences between maps at different resolutions;
- to obtain patterns of brightness temperature nested between different resolution for scaling purposes; and
- to have high resolution areas falling within the central pixels of the swath at each altitude (beam 1 or 2) to ensure they are not inadvertently missed due to diversions from planned flight paths and wing level attitude, or variations in ground elevation.

The main constraints include:

- to have sufficient overlap between adjacent flight lines in order to avoid areas of no data due to aircraft roll or variations in ground elevation;
- to have sufficient overlap to allow temporal correction of data back to a reference time;
- to have ground sampling points at the centre of aircraft pixels;
- to have a nested network of ground sampling grids linked between different ground sampling resolution.

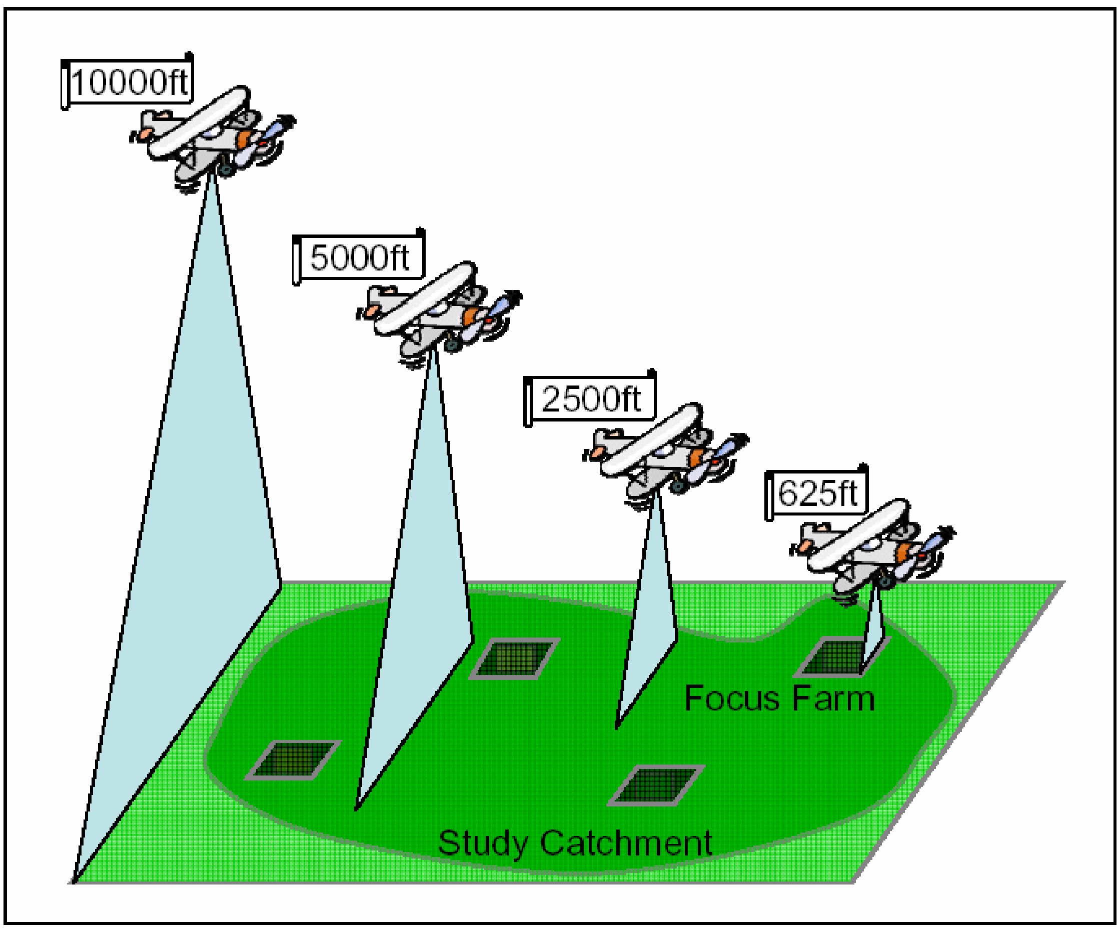

Figure 2.11: Schematic view of PLMR flights.

2.4.3 Low Resolution Mapping

One of the objectives of NAFE '05 is the mapping of soil moisture at satellite footprint scale from an airborne platform. This component of the airborne campaign will provide the necessary link between the passive microwave observations at high resolution and the equivalent spaceborne observation over large areas for scaling purposes. Furthermore, low resolution observations from the aircraft are easier to accurately validate than the satellite observations, due to the smaller ground pixel size achievable (1km against 50km). This allows more accurate verification of the satellite-retrieved soil moisture over large areas by making use of the validated 1km product obtained with the aircraft.

Low resolution mapping flights have been flown at a nominal altitude of 10000ft AGL. Actual altitude above sea level was of 3430m, which results from flying above the median elevation of the terrain in the Northern Goulburn study. Ground pixel resolution varies from approximately 861m to 1066m due to variable terrain elevation, with a mean resolution of 1km. Low resolution flights have been undertaken on various dates with different coverage's during the campaign:

- During regional days, low resolution flights occupied the entire daily flying time and the coverage was the area approximately covered by a satellite footprint.
- During farm scale days, low resolution flight have been undertaken together with intermediate, medium and high resolution flights, with coverage being one of the two sub-catchment study areas, either Krui or Merriwa.

2.4.4 Intermediate resolution mapping

Flights at intermediate altitudes allowed investigation of the scaling nature of the microwave signature of soil moisture and provided the link between regional scale microwave observations and the high resolution mapping, which has been one main scientific objective of the campaign. The acquisition of microwave brightness temperatures at so many different resolutions was unprecedented. Investigation focused on the relationship between brightness temperatures measured at different spatial resolution, down- and up-scaling issues.

Intermediate resolution mapping included flights at a nominal 5,000ft AGL over two subareas in the northern half of the Goulburn River experimental study area, the Krui catchment and the Merriwa catchment. The actual planned flight altitude due to terrain elevation is 1910m ASL. This results from flying over the median terrain elevation of the Northern Goulburn study area. This reference elevation is the same for the low resolution and the intermediate resolution flights, and was chosen in order to maintain consistency between observations at different altitudes. These flights entirely covered the NAFE focus farms and surrounding areas and constituted an adequate medium resolution "frame" to the high resolution mapping of the individual farms.

2.4.5 Medium resolution mapping

Flights at medium altitudes allowed investigation of the scaling nature of the microwave signature of soil moisture and provided the link of the regional scale microwave observations with the high resolution mapping which is a main scientific objective of the campaign.

Mapping at medium resolution has been undertaken at farm scale, at a nominal altitude of 2500ft AGL, providing full coverage of all the NAFE focus farms at a ground resolution of approximately 250m. Actual flight altitude for these flights was variable between farms, due to terrain elevation. Unlike for the low and intermediate flights, terrain elevation has a major impact on the ground resolution obtainable from these altitudes. In particular, due to the different mean elevations of the focus farms, it was not feasible to fly the whole medium resolution flight line set with constant altitude above sea level. This would in fact result in highly variable ground resolution. With the aim to maintain the highest possible consistency between the soil moisture maps, a decision was made to fly at 2500ft (and 625ft for the high resolution flights) above the maximum elevation within each farm. This guaranteed greater uniformity in ground resolution as well as respect of the minimum flight altitude allowed without a low-level clearance, being 500ft. As for the medium resolution flight lines, flight altitude varied between 1050m and 1270m ASL for the respective resulting in a ground resolution between 240m and 308m.

2.4.6 High resolution mapping

One of the most important phases of the NAFE '05 campaign was the monitoring of soil moisture at high resolution. PLMR was flown at a nominal altitude of 625ft AGL to provide a nominal grid of 62.5m average near-surface soil moisture. Such a high resolution in passive microwave remote sensing is unprecedented, and gives the opportunity to study the microwave emission from the soil surface at very high detail.

2.4.7 Extra flights

Some extra flights have been performed to allow further analysis on the microwave emission measurement.

A number of high resolution flights have been performed for the specific purpose of studying the effect of angle on radiometer measurement.

During these flights PLMR has been mounted 90° rotated compared to the standard configuration so as to have the 6 beams looking along the flight direction, 3 forward and 3 backward.

Moreover two short flights in the very early morning have been performed in order to collect data to study the dew effect on radiometer measurement.

3

SOIL MOISTURE RETRIEVAL MODEL

The theory behind microwave remote sensing of soil moisture is based on the large contrast between the dielectric properties of liquid water and dry soil. As the moisture increases, the dielectric constant of soil-water mixture increases and this change is detectable by microwave sensors.

In this chapter the retrieval algorithm for soil moisture (*Jackson et al.*, 1981; *Schmugge*, 1985) from microwave remote sensing is described in all its components and particular attention is given to the model developed for the calculation of the dielectric constant of the soil (*Wang and Schmugge*, 1980).

In addiction the model considers the contribution of surface roughness and vegetation coverage in the attenuation of the microwave emission, integrating studies carried on by *Choundhury et al.*, 1979, *Njoku and Entekhabi*, 1995, *Jackson and Schmugge*, 1991.

3.1 Theoretical background

Microwave remote sensing measures the electromagnetic radiation in the microwave region of the electromagnetic spectrum, which has wavelengths between 0.5 and 100cm. For remote sensing of soil moisture, L-Band passive microwaves (10-30cm) are recognized to provide the most accurate results. The main advantages of microwave remote sensing over remote sensing in the visible and infra-red regions are that the attenuation of the signal received by the sensor by atmospheric gases and clouds is negligible and that vegetation is semi-transparent at microwave wavelength (*Jackson and Schmugge*, 1991), Fig. 3.1. Nevertheless the passive systems can only provide a spatial resolution between 10km and 100km, appropriate for meteorological and climate models. Thus, some downscaling techniques are currently in development to make these data suitable for other purposes, like flood forecasting, agriculture management and meso-scale climate models.

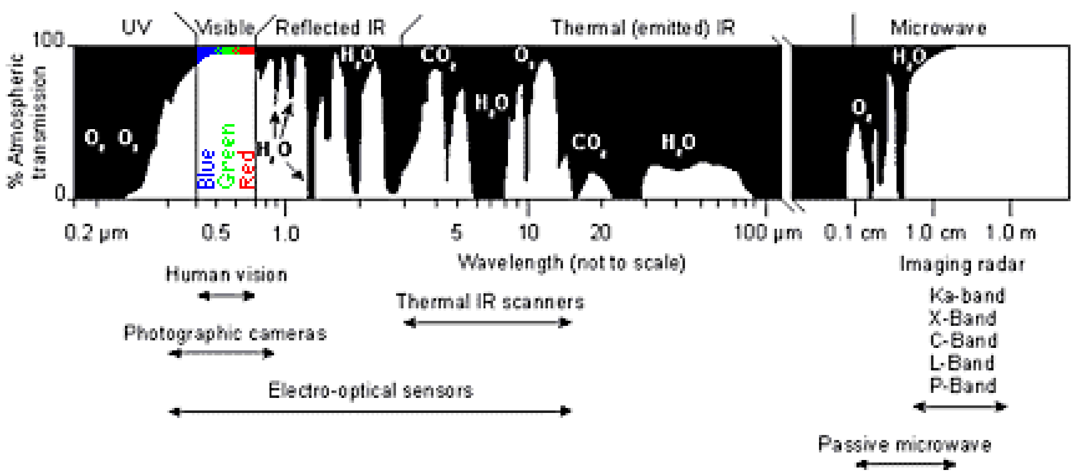

Figure 3.1: Atmospheric transmissivity as a function of the wavelength

A microwave radiometer measures the self emitted and reflected radiation from the earth's surface, whose intensity is characterized by the brightness temperature (T_b). The amount of energy generated at any point within the soil volume depends on the soil temperature and the soil dielectric properties. In addiction as the energy crosses the surface boundary, it is reduced by emissivity coefficient, which is determined by the dielectric characterization of the near surface soil (*Schmugge et al*., 1980).

3.2 Brightness temperature model

Brightness temperature is dependent on the soil moisture and on the temperature profiles of the soil; it is the product of the soil temperature and emissivity of the soil through the Rayleigh-Jeans approximation of Plank's law (*Jackson et al.*, 1981; *Schmugge*, 1985). The value of T_b measured by a radiometer is given by

$$T_{b_p} = \tau(\Gamma_p T_{sky} + e_p T_{soil}) + T_{atm} \tag{3.1}$$

where Γ_p is the surface reflectivity for polarization *p*, e_p is the surface emissivity for polarization *p* and τ is the atmospheric transmission.

For the typical remote sensing applications using microwave, the atmospheric T_{atm} and sky T_{sky} contributions are small compared to the soil one (*Engman and Chauhan*, 1995). Thus by neglecting these two terms the Rayleight approximation may be simplified to

$$T_{b_p} = e_p T_{soil} = (1 - \Gamma_p) T_{soil} \tag{3.2}$$

Although the relationship between emissivity and T_b is linear, soil moisture has a non linear dependence on reflectivity and because the reflection coefficient of the soil is related in a non-linear way to the dielectric constant of the soil (*Engman and Chauhan*, 1995).

The reflectivity is generally predicted by the Fresnel equations:

$$e_h = 1 - \left| \frac{\cos\vartheta - \sqrt{\varepsilon - \sin^2\vartheta}}{\cos\vartheta + \sqrt{\varepsilon - \sin^2\vartheta}} \right|^2 \tag{3.3a}$$

$$e_v = 1 - \left| \frac{\varepsilon\cos\vartheta - \sqrt{\varepsilon - \sin^2\vartheta}}{\varepsilon\cos\vartheta + \sqrt{\varepsilon - \sin^2\vartheta}} \right|^2 \tag{3.3b}$$

where ϑ is the look angle for the instrument measured from nadir (degrees) and ε is the relative dielectric constant of the soil.

In the current study, the model of *Wang and Schmugge* (1980) was inverted to estimate soil water content from the dielectric properties of soil-water-air mixture.

Therefore it is important to define the soil composition, especially regarding clay and sand percentages. In this model values for each constituent are taken from the centroid of 12-USDA Textural Classes (Fig. 3.2) while porosity data from *Rawls et al.*, 1982 in TASAE (Table 3.1).

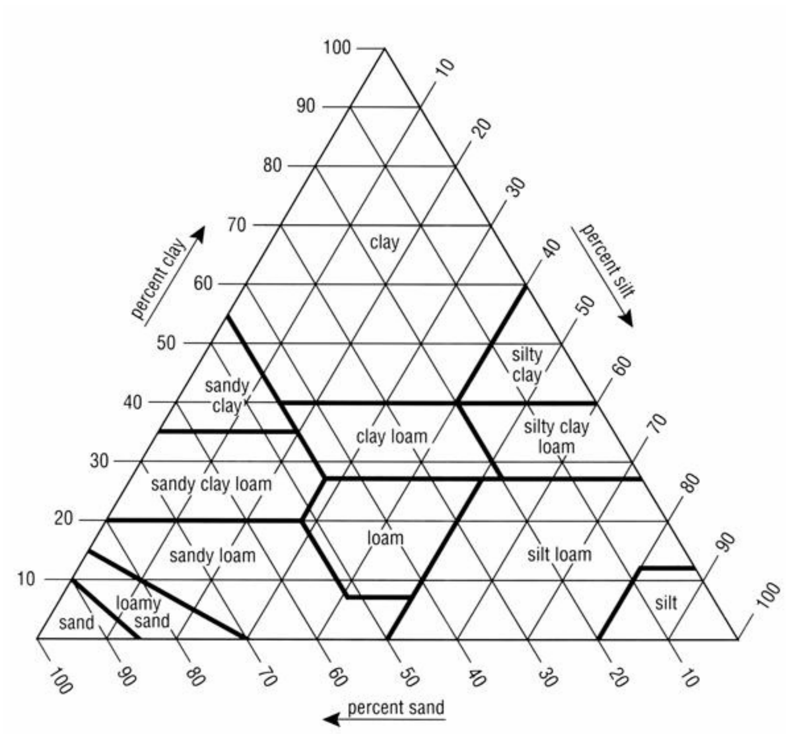

Figure 3.2: Chart showing the percentages of clay, silt and sand in the basic textural classes

Table 3.1: 12-USDA Textural Classes and Porosity

Class #	Soil Type	Clay	Sand	Porosity
1	Sand	5	92	0.437
2	Loamy sand	7	78	0.437
3	Sandy loam	10	65	0.453
4	Silt loam	15	35	0.501
5	Silt	6	10	0.482
6	Loam	20	40	0.463
7	Sandy clay loam	28	60	0.398
8	Silt clay loam	48	7	0.471
9	Clay loam	33	33	0.464
10	Sandy clay	52	43	0.430
11	Silty clay	58	6	0.479
12	Clay	60	20	0.475

The relationship between volumetric soil moisture and dielectric constant consist of two distinct parts separated at a transition moisture value θ_T defined by

$$\theta_T = 0.165 + 0.49\theta_{wp} \tag{3.4}$$

where θ_{wp} is an empirical approximation of the wilting point moisture based on the sand and clay mass fraction given by

$$\theta_{wp} = 0.06774 - 0.00064 sand + 0.00478 clay \tag{3.5}$$

Unique equations describe the relationship between dielectric constant and soil moisture less than and greater than the transition moisture content. For soil moisture less than θ_T, the real and imaginary parts of the dielectric constant ε are:

$$\varepsilon' = \theta \times \left(\varepsilon_i + \frac{(\varepsilon_w - \varepsilon_i)\delta\theta}{\theta_T} \right) + (p - \theta) + \varepsilon_r \times (1 - p) \tag{3.6a}$$

$$\varepsilon'' = \theta \times \left(0.1 + \frac{6.53\delta\theta}{\theta_T} \right) + 0.2 \times (1 - p) \tag{3.6b}$$

Otherwise, if the soil water content is higher than θ_T, the dielectric constant is evaluated in the following way:

$$\varepsilon' = \theta_T \times \left(\varepsilon_i + (\varepsilon_w - \varepsilon_i)\delta\right) + \varepsilon_w \times (\theta - \theta_T) + (p - \theta) + \varepsilon_r \times (1 - p) \tag{3.7a}$$

$$\varepsilon'' = \theta_T \times \left(0.1 + 6.53\delta\right) + 6.63 \times (\theta - \theta_T) + 0.2 \times (1 - p) \tag{3.7b}$$

where ε_r, ε_i, ε_w are the dielectric constants for rock, ice and water respectively, p is the soil porosity and

$$\delta = 0.481 - 0.57\theta_{wp} \tag{3.8}$$

3.3 Roughness correction

The effect of surface roughness on the brightness temperature of a moist terrain has been introduced by modifying the Fresnel reflection coefficient introducing a single parameter to characterize the roughness, the standard deviation of surface height (*Choundhury et al.*, 1979). Surface roughness decreases the reflectivity (increases the brightness temperature) and decreases the difference between the vertically and horizontally polarized brightness temperatures (*Njoku and Entekhabi*, 1995). The sensitivity of brightness temperature to soil moisture decreases significantly as the surface roughness increases, thus corrections for roughness are necessary to obtain accurate soil moisture estimates.

The roughness parameter h is given by

$$h = 4\sigma^2 \left(\frac{2\pi}{\lambda}\right) \tag{3.9}$$

where λ is the wavelength captured by the radiometer ($\lambda = 21cm$ for L-Band microwaves) and σ^2 is the height variance of the surface, measured during the field campaign in four points for each farm, as described in Chapter 2.3.6. For smooth surfaces a typical value of h is 0.1, and for very rough fields a value of h equal to 0.6 is typical (*Choundhury et al.*, 1979, *Wang et al.*, 1983).

Thus the Fresnel reflectivity e_p has been modified as

$$e_p(\vartheta) = 1 - \left(1 - e_p\right)\exp\left(-h\cos^2\vartheta\right) \tag{3.10}$$

where the subscript p designates the polarization and ϑ is the look angle. Table 3.2 shows the values of the roughness parameter h evaluated for the farms of interest. First the height variance σ^2 has been evaluated for each point of measurement in the two directions North-South and East-West. Then an average of these values was taken in order to obtain a single σ^2 per farm to calculate the roughness parameter. These values are consistent with visual observations and impressions felt while sampling those areas.

Table 3.2: Roughness parameter for NAFE farms

	σ^2		σ^2		σ^2		σ^2		$\sigma^2_{average}$	h
FARM	N-S	E-W	N-S	E-W	N-S	E-W	N-S	E-W		
Stanley	0.79	0.27	0.36	1.90	1.40	1.99	1.92	1.75	1.30	0.46
Pembroke	0.61	0.96	0.54	0.82	0.24	1.15	0.25	1.76	0.79	0.28
Roscommon	0.43	0.51	0.26	0.46	0.34	0.25	0.61	0.37	0.40	0.14
Illogan	1.47	0.38	1.97	1.74	0.54	0.17	1.00	1.40	1.08	0.39
Midlothian	0.26	0.32	2.16	0.48	0.54	0.39	1.77	0.53	0.81	0.29
Dales	0.43	0.67	1.16	1.47	0.28	1.16	0.78	0.97	0.87	0.31
Cullingral	0.72	1.23	0.56	0.19	0.46	0.13	0.24	0.38	0.49	0.18

3.4 Vegetation correction

The influence of vegetation on brightness temperature measured by the radiometer is the result of absorption and re-emission, absorbing radiation coming from the soil and emitting radiation itself. For low frequencies (< 5-10GHz) the effects of scattering are negligible. Figure 3.3 shows the radiation components in canopy layer:

1. the direct vegetation emission;
2. soil-surface emission attenuated by the canopy;
3. downward cosmic background and atmospheric radiation attenuated by the canopy;
4. the vegetation emission reflected by the soil and attenuated by the canopy.

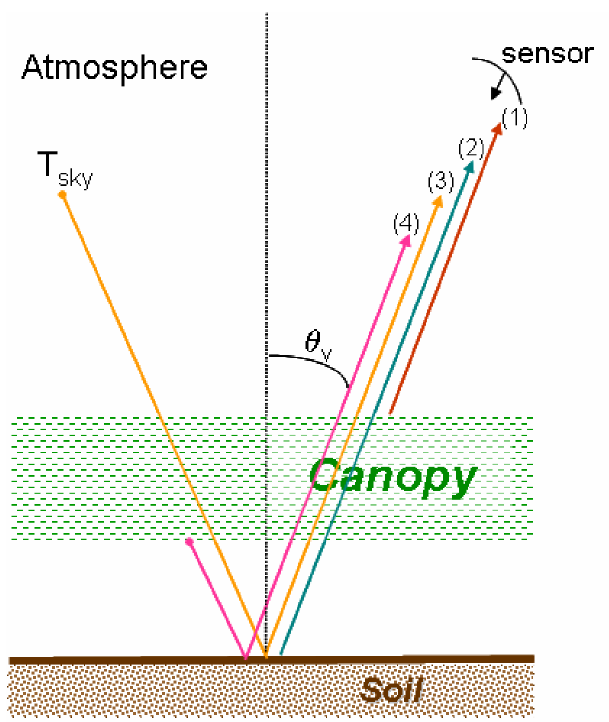

Figure 3.3: Radiation components in a vegetation layer

A model that takes into account the vegetation effects is (*Ulaby et al.*, 1986):

$$T_{b_p} = \left[1 + \left(1 - e_p\right)\gamma_{veg}\right]\left(1 - \gamma_{veg}\right)\left(1 + \alpha\right)T_{veg} + \left(e_p \gamma_{veg} T_{soil}\right) \tag{3.11}$$

where:

- γ_{veg} is the transmissivity of the vegetation layer
- T_{veg} is the physical temperature of the vegetation (K)
- T_{soil} is the physical temperature of the soil
- α is the single scattering albedo of the vegetation.

Albedo represents the fraction of incoming solar radiation that is reflected at the canopy or soil surface. At microwave wavelength the single scattering albedo is close to zero, varying in a range between 0.05 and 0.10. Running the model α has been fixed at the value of 0.05.

The temperature of the vegetation has been considered the same as the soil temperature, whose estimation will be explained in Chapter 5.

The transmissivity of the attenuating vegetation layer is described by a relationship with one way canopy absorption factor, the vegetation opacity, otherwise known as optical depth τ. τ is dependent on the vegetation dielectric properties, plant shape and structure, polarization, look angle and wavelength.

$$\gamma_{veg} = \exp\left[-\tau \sec \vartheta\right] \tag{3.12}$$

where ϑ is the look angle measured from nadir (degrees).

The relationship used in this study for the optical depth is

$$\tau = VWC \times b \tag{3.13}$$

where WVC is the vegetation water content and *b* is a regression parameter (*Jackson and Schmugge*, 1991).

The parameter *b* is unique to the type of vegetation, the free space wavelength and polarization. In Figure 3.4 a plot of *b* for different wavelengths and vegetation types is shown (*Jackson*, 1993): except for native grass, it presents a small variation in the L-Band range and a value of 0.15 is representative of most agricultural crops. Chapter 6 will describe how WVC has been estimated in the study.

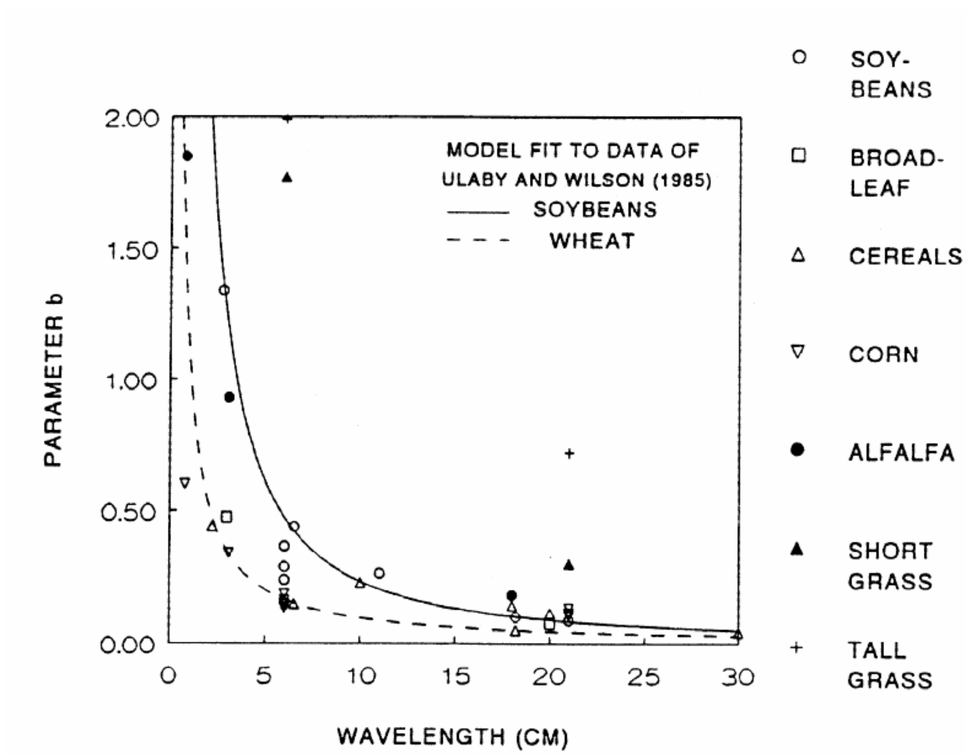

Figure 3.4: Effects of vegetation on parameter b as a function of wavelength (*Jackson,* 1993)

3.5 Model implementation

A MATLAB program has been implemented to run the model; the bisection method was used to search the solution of the equations discussed in the previous paragraphs. This root-finding algorithm works by repeatedly dividing an interval and then selecting subinterval in which the root exists. The efficiency of the bisection method is limited but it ensures stability and convergence to the solution.

Actually, for minimizing the difference between measured brightness temperature and the one calculated by the model, assuming different values of moisture content, the bisection method presents a satisfactory performance. In fact, it provides a solution in less than twenty iterations with an accuracy of 10^{-4}.

4

SOIL BRIGHTNESS TEMPERATURE

The airborne data collection campaign has been successful in meeting the proposed objectives of NAFE ’05. Data collected include bipolarized, L-band passive microwave observations at multiple incidence angle, thermal infrared imaginer, and aerial photography.

One of the first steps toward accurate soil moisture estimation has been to study the influence of brightness temperature acquisition uncertainty on the soil moisture retrieval, as well as to perform a calibration of the PLMR radiometer in order to obtain reliable microwave data.

This chapter illustrates in detail the above steps and presents the resulting calibrated soil brightness temperature for both V and H polarization for the 20 days of the NAFE ‘05 field campaign.

4.1 Brightness temperature sensitivity to soil moisture

The amount of energy emitted by the ground surface in the microwave domain depends on several factors besides the soil water content. In particular, the soil moisture retrieval model used in this study involves up to ten variables. This fact makes it hard to understand how a single factor can influence the brightness temperature measured by the radiometer.

Nevertheless, a rough estimate of the relation between brightness temperature and soil moisture is needed in order to understand how the uncertainty of the radiometric observation can affect the soil moisture retrieval. This relation will be used as criterion to evaluate the proposed calibrations for the radiometer.

4.1.1 Assumption and constant parameters

Some preliminary assumptions are needed in order to make a sensitivity assessment. The number of variables has been reduced to four maintaining those, which have been considered a priori the most significant in the soil moisture retrieval: vegetation water content, soil moisture, incidence angle and soil temperature. The remaining variables have been assumed constant.

- The surface roughness has been set to 0.3, which is an average value over the ground surface roughness measurements made during the NAFE '05 field campaign over the study area. Microwave emission is strongly affected by the soil roughness, but this parameter is also difficult to measure, due to his strong spatial variability.
- The scattering albedo, whose effect on the measured brightness temperature is known to be weak at L-band wavelength, has been assigned a value of 0.05, which is a standard value often used in literature in the case of the vegetation cover type most common in our study area.

- The soil type has been assumed constant as well. Silty clay loam has been chosen as the more common soil type in the Goulburn catchment after analysis of 12 soil texture samples taken in the area.

Some extreme scenarios have been chosen, fixing extreme values of the four main variables, in order to represent the whole range of conditions occurred during the NAFE'05 field campaign. Intermediate input values have always shown to give intermediate results.

- The Incidence Angle was given a lower value of 0° and an upper value of 40°, which correspond to an increase of about 3° due to roll, pitch and yaw compared to the standard conditions.
- The vegetation was given a range of values between 0kg/m^3 (bare soil), and 3kg/m^3 which is an average value for a strongly vegetated surface.
- Soil moisture values were varied between 0.05 v/v, which correspond to a dry soil, and 0.4 v/v, which is a very wet soil.
- Soil temperature was set to 280K for a cold soil and 315K for a hot soil.

The error in soil moisture content as a function of the uncertainty in brightness temperature is plotted in Figure 4.1 for all the scenarios proposed.

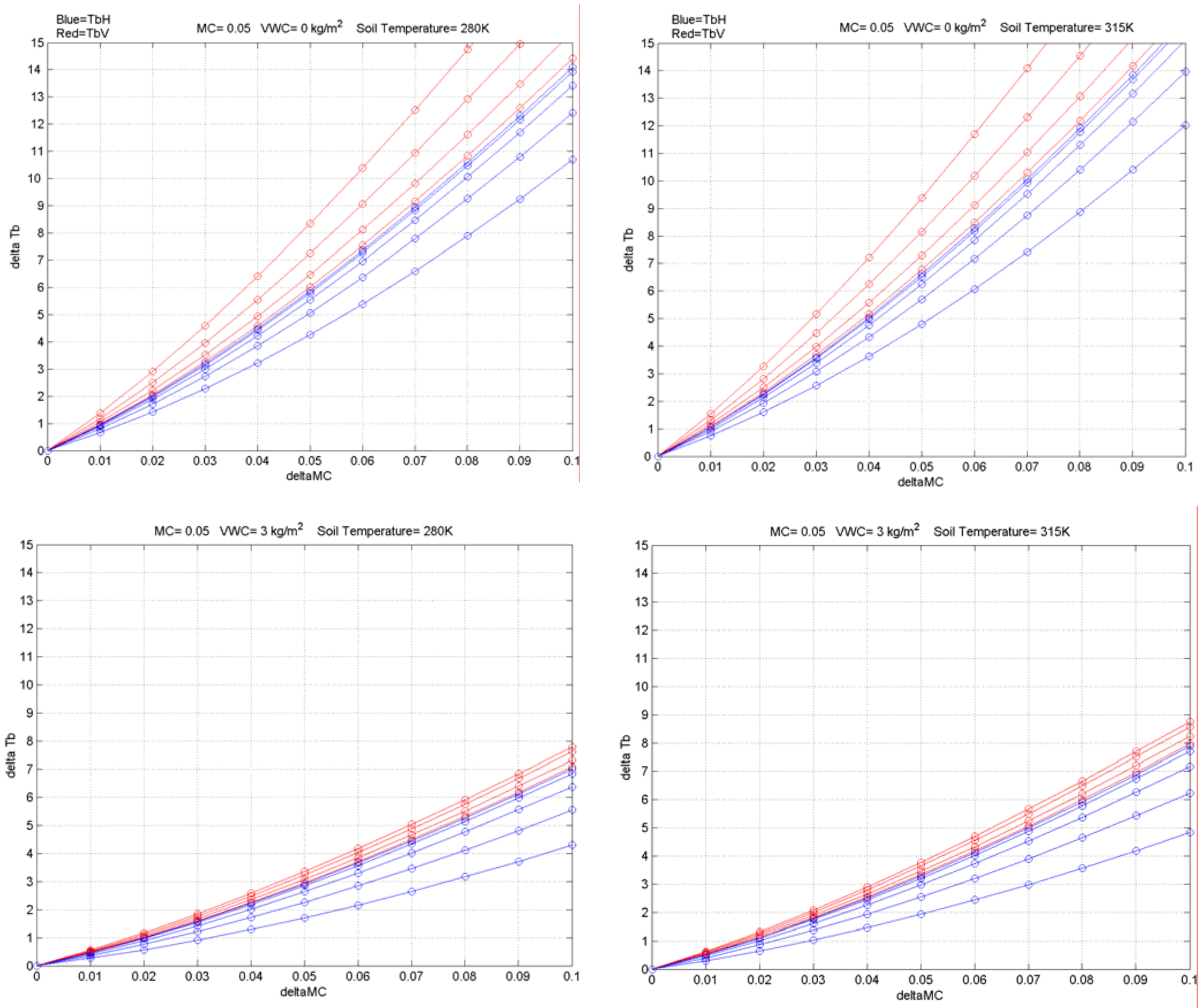

Figure 4.1(a): Angular variation of the error in brightness temperature against error in soil moisture for dry soil scenarios.

Each plot shows for both H and V polarization the sensitivity for different angles. It can be noticed that for dry soils (Figure 4.1a) the variation due to different angle is much higher than for wet ones (Figure 4.1b). Moreover the slope of these relation is strongly dependent on vegetation water content and for high values of this variable the slope has the lowest value, which means a big propagation of the error.

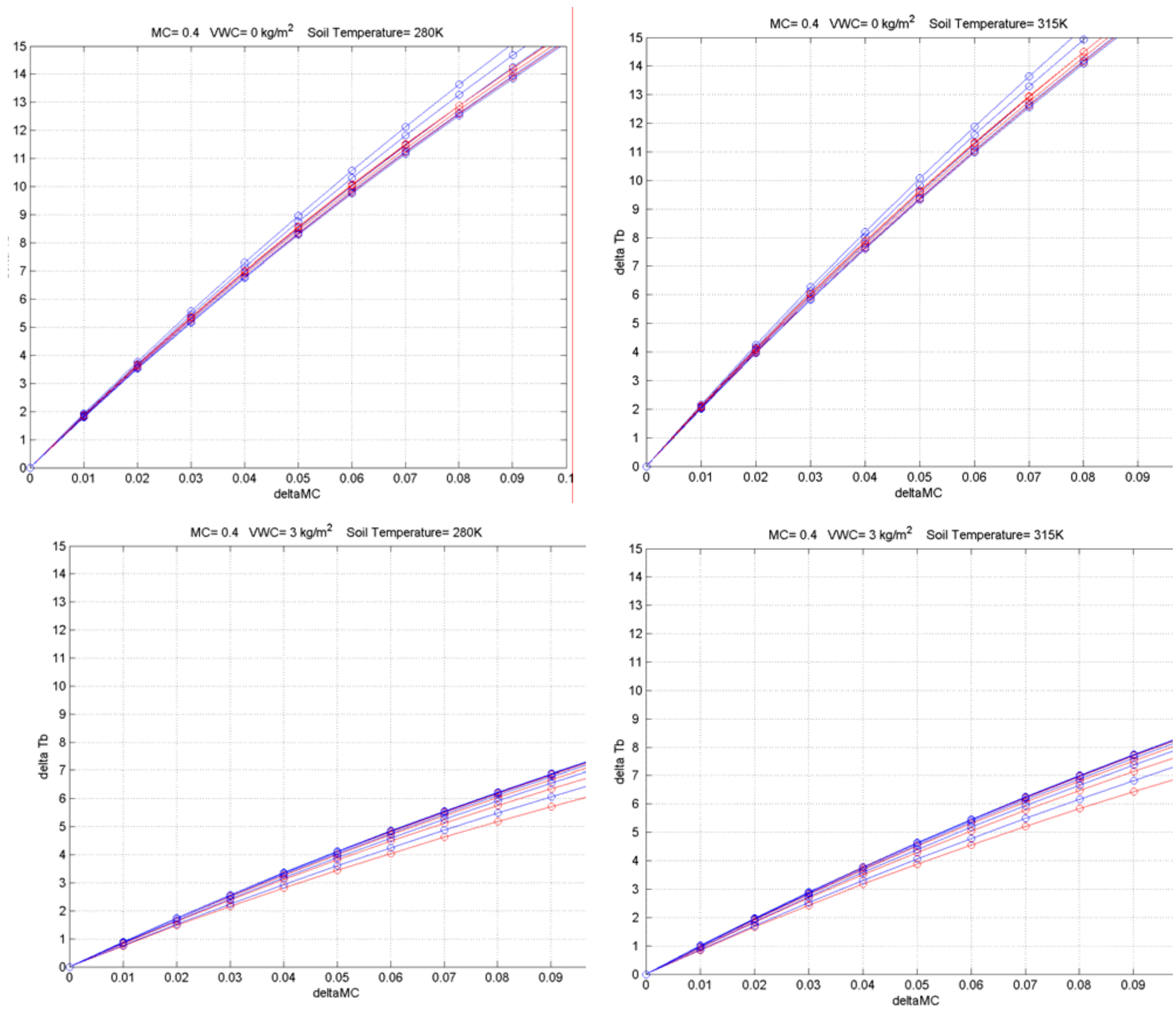

Figure 4.1(b) Error in brightness temperature against error in soil moisture for wet soil scenarios

The next step is to extrapolate from this analysis acceptable errors in brightness temperature. An acceptable error is considered the one that produce 4% accuracy in soil moisture, which is the proposed goal for the future SMOS mission. The Tables 4.1a and 1b summarize the results of this analysis for each scenario investigated.

		Moisture Content				Vegetation Water Content
		dry		wet		
Soil Temperature	**cold**	4.5	6.4	6.7	7.0	0
	hot	5.0	7.2	7.6	7.9	
	cold	2.2	2.6	3.4	2.8	3
	hot	2.5	2.9	3.8	3.2	
		0	**40**	**0**	**40**	
		Incidence Angle				

Table 4.1a Acceptable errors in different scenarios for H polarization.

		Moisture Content				Vegetation Water Content
		dry		wet		
Soil Temperature	**cold**	4.5	3.2	6.8	7.3	0
	hot	5.0	3.6	7.6	8.2	
	cold	2.2	1.3	3.4	2.9	3
	hot	2.5	1.5	3.8	3.3	
		0	**40**	**0**	**40**	
		Incidence Angle				

Table 4.1b Acceptable errors in different scenarios for V polarization

As shown in these tables, for the V polarization the "worst" scenario is cold and dry soil, with a high value of vegetation water content and for high values of incidence angle. For the H polarization the "worst" scenario is similar, but for low incidence angle. In the worst scenarios therefore the brightness temperature uncertainty should not be higher then 1.3K at V polarization to reach the proposed 4% soil moisture accuracy, whereas at H polarization the uncertainty it can be up to 2.2K

Over the NAFE ’05 study area the conditions corresponding to these “worst” scenarios have occurred rarely. The most common set of input variables can be considered the one with medium-hot soil and low vegetation water content. For this frequent condition, the maximum error in brightness temperature measurement can be up to 3.6K for the V polarization and 5.0K for the H. Finally, we can also say that, as the tables show, commonly an error up to 8K can be tolerated.

4.2 Box, water and sky points investigation

Calibration of the PLMR is performed by making observations of a target whose brightness temperature is known. By plotting these observed values against the known brightness temperatures of the objects, a linear regression can be subsequently calculated and then used to correct the raw data for gain and bias.

The targets used for calibration are a blackbody (a box), the sky and a water body. Observations of the blackbody and the sky were taken from the ground before and after each flight, whereas observations of the water body and again of the sky were collected during the flight. In the following part terms like water-point, sky-point, and box-point will be used, meaning the points obtained with actual and measured values for the calibration targets.

4.2.1 Box

The box available during the campaign was assumed to have blackbody properties, in the sense that its emissivity in the microwave L-band domain was considered to be equal to one. This allows direct comparison between the box-emitted brightness temperature detected by the PLMR and the box physical temperature.

The box-points have been collected every day before and after the flight averaging up to 20 minutes of PLMR acquisition data. This procedure has been carried on in order to obtain a stable value, since temperature of the medium surrounding the box can affect this measurement. The data collected have been also cleaned up from noises and malfunctioning of the recording system.

The box physical temperature has been recorded with a logger installed just beneath the box. (Figure 4.2)

Figure 4.2 The radiometer collecting box-observations for the calibration.

The box-points have been the most important ones since their values are the closest ones to the soil brightness temperature. Fortunately, they are also the more reliable ones, since this measure took place in quite stable and controlled conditions.

4.2.2 Water

The water-points have been obtained during the flight collecting measurement of brightness temperature while flying above Lake Glenbawn, a water body approximately 100km East of the study area.

The measured value has been calculated averaging a 2 minute long observation cleaned up from easy recognizable non-water measures (vegetation in the water and shores mainly). The Figure 4.3 shows the raw water brightness temperatures. According to the theory (*Jackson and Le Vine*, 1995), the water points fit two parabola, which are tangent for observation made at nadir

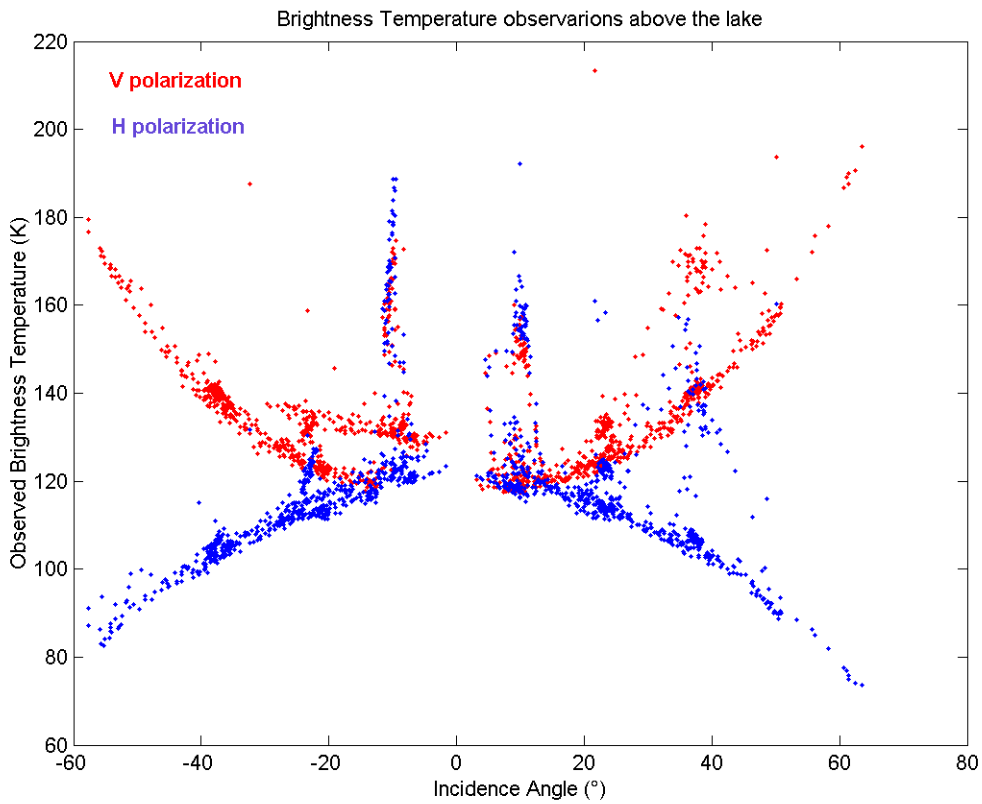

Figure 4.3 Radiometer observation of the water body plotted as brightness temperature against incidence angle.

The PLMR observation has been compared to what was supposed to be the actual brightness temperature of the water, which has been calculated with a well-known water emission physical model (*Klein and Swift*, 1976). This model takes into account the salinity, which can be retrieved from conductivity, and the temperature of the lake. Measurements of these variables have then been taken during the field campaign by a temperature and salinity measuring station installed at the center of the lake (see Figure 4.5).

Furthermore, the lake have been monitored once a week by doing 100m spaced temperature and salinity measurements along two, 2km long north-south and east-west orientated transects, centered on the monitoring station, in order to account for the spatial variability of water salinity and temperature.

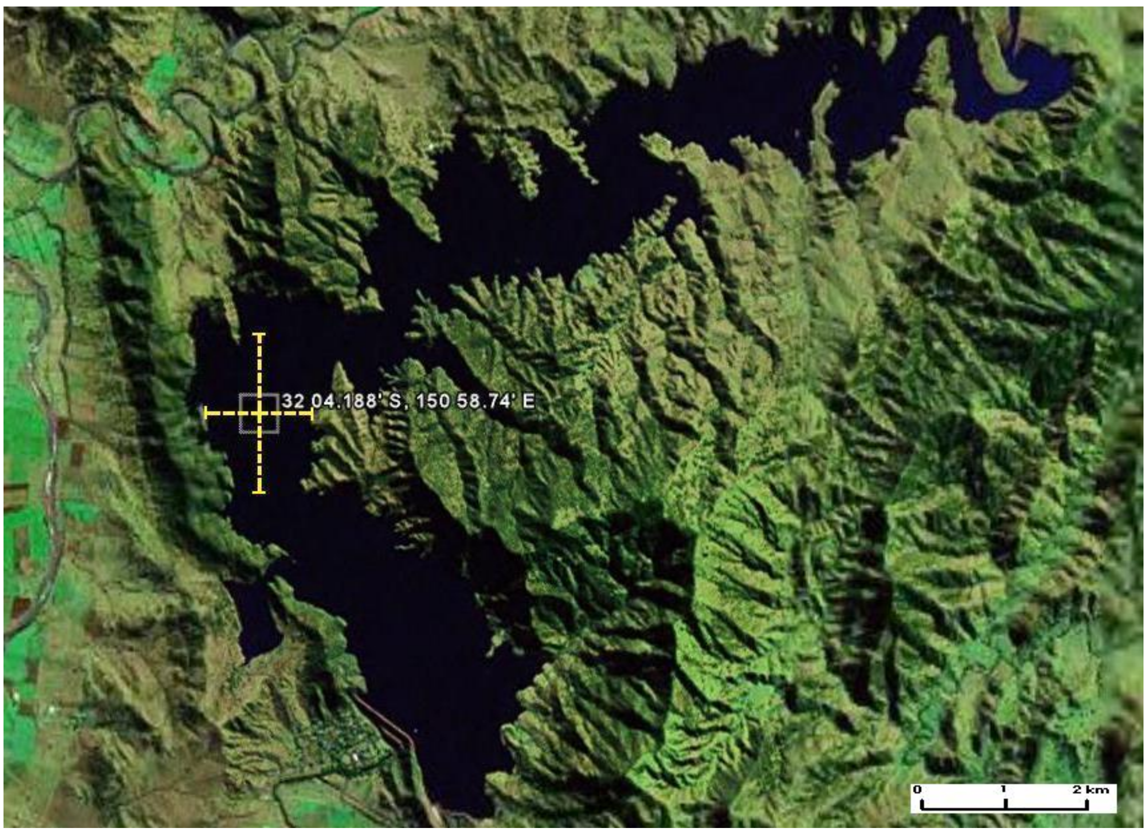

Figure 4.4 Transect location show by a satellite image

Additional information about lake temperature can be obtained by the thermal infrared camera installed on the aircraft.

The brightness temperature model has been set up thanks to an improved model for the dielectric constant of saline water at microwave frequencies (*Klein and Swift,* 1976).

The ionic conductivity of water is defined by the following relationships:

$$\sigma(T,S)=\sigma(25,S)\exp(-\Delta\beta)$$

where

$$\sigma(25,S)=S(0.182521-1.46192\times10^{-3}S+2.09324\times10^{-5}S^2-1.28205\times10^{-7}S^3)$$

$$\Delta=25-T$$

and

$$\beta=2.033\times10^{-2}+1.266\times10^{-4}\Delta+2.464\times10^{-6}\Delta^2-S(1.849\times10^{-5}-2.551\times10^{-7}\Delta$$
$$+2.551\times10^{-8}\Delta^2)$$

where T is the water temperature in degrees centigrade, S is the salinity in parts per thousand and σ is the ionic conductivity in mhos/meter.

Once conductivity and temperature are known, salinity can be retrieved with an optimization process, which minimizes the error between measured conductivity and computed one.

Water dielectric constant has been then computed by

$$\varepsilon(T,S)=\varepsilon(T)\alpha(S,T)$$

where

$$\varepsilon(T) = 87.134 - 1.949 \times 10^{-1} T - 1.276 \times 10^{-2} T^2 + 2.491 \times 10^{-4} T^3$$

and

$$\alpha(S,T) = 1 + 1.613 \times 10^{-5} ST - 3.656 \times 10^{-3} S + 3.21 \times 10^{-5} S^2 - 4.232 \times 10^{-7} S^3$$

This model can be used for the entire microwave spectrum and has been proved more accurate in the lower part of it, where L-band is located (*Klein and Swift*, 1976).

Assuming the lake water to be an infinite flat source of microwave the emissivity related to an incidence angle θ can be obtained through the Fresnel effect for both V and H polarization

$$e_V = 1 - \left| \frac{\varepsilon \cos(\vartheta) - \sqrt{\varepsilon - sen(\vartheta)^2}}{\varepsilon \cos(\vartheta) + \sqrt{\varepsilon - sen(\vartheta)^2}} \right|^2$$

$$e_H = 1 - \left| \frac{\cos(\vartheta) - \sqrt{\varepsilon - sen(\vartheta)^2}}{\cos(\vartheta) + \sqrt{\varepsilon - sen(\vartheta)^2}} \right|^2$$

and then the brightness temperature

$$T_B = eT$$

Unfortunately, due to a malfunctioning of the lake permanent logger the salinity and temperature needed by the water model have been available only for half of the campaign. This fact affected the design of the calibration.

4.2.3 Sky

Measurements of sky brightness temperature have been collected before, during and after the flight. The ground sky points have been obtained averaging up to 20 minutes of upward looking PLMR data (Figure 4.5) and cleaning them by sun noise and in order to obtain a stable value, which can be disturbed by the temperature change of the instrument.

Figure 4.5 Upward looking radiometer collects a sky-point for the calibration.

The measurement during the flight has been obtained by performing some steep turns with the aircraft, achieving a roll close to 90° at both sides in order to look at the sky.

These data have been compared with the theoretical brightness temperature of the sky, which has been estimated with an atmosphere model that describes the microwave interaction with atmospheric constituents. *(Ulaby, Moore and Fung, 1981)*

In the microwave spectral region, the atmosphere is practically transparent even in the presence of clouds and moderate rain event. The layer of interest is the lower part of the atmosphere, as this it is the layer which contains most of the total atmospheric mass and therefore influences upward measurement of the sky brightness temperature.

The model takes into account the effects of temperature, pressure and those gases that show significant absorption bands in the microwave spectrum, which are oxygen and water vapor. This model uses widely the 1962 U.S. Standard Atmosphere.

Temperature profile

The variation of atmospheric temperature with height shows a cyclic pattern, which can be used to subdivide the earth's atmosphere in a number of layers according to their thermal behavior.

The lower layer of earth's atmosphere, the troposphere with height up to 10Km has a temperature lapse rate of about 6.5K/km.

The next layer is the stratosphere, which extends approximately from 10 to 47km. In the lowest 10km the temperature is basically constant and then it increase with height between 20 and 32km above sea level with a gradient of 1K/km.

At a height z in km above sea level, the temperature T(z) in K is then given by

$$T(z)=\begin{cases} T(0)-6.5z & 0\le z\le 11km \\ T(11) & 11\le z\le 20km \\ T(11)+(z-20) & 20\le z\le 32km \end{cases}$$

where T(0) is assumed constant at 288K.

Pressure profile

Assuming air to be an ideal gas, the pressure profile can be obtained trough air density profile and temperature profile with the state equation.

A simpler approximation that provides value within 3% of the recorded ones is to fit the pressure profile with an exponential function

$$P(z)=P(0)\exp\left(\frac{-z}{H_3}\right)$$

where H_3=7.7km is the *pressure scale height* and P(0)=1013.25mbar.

Water vapor density profile

The water vapor can be roughly modeled with en exponential function of the height. The critical parameter is the water vapor density at sea level that vary from 10^{-2}gm^{-3} in cold and dry climate up to 30gm^{-3} in hot and humid climates. The average surface value for middle latitude is ρ_0=7.72gm^{-3}.

The altitude profile of water vapor can be obtained then with

$$\rho_v(z)=\rho_0\exp\left(\frac{-z}{H_4}\right)$$

where the scale height H_4 has been set to 2km.

Water vapor absorption coefficient

From the water vapor and temperature profile the total water vapor absorption coefficient for frequency below 100GHz can be obtained (in dB km^{-1})

$$k_{H_2O}(f) = k(f,22) + k_r(f)$$

Where the first term is the absorption coefficient of the 22.235GHz line and the second one is the residual absorption coefficient representing the contributions of all higher-frequency water vapor absorption lines.

Merging the two individual equations, the following formula is obtained:

$$k_{H_2O}(f) = 2f^2\rho_v\left(\frac{300}{T}\right)^{3/2}\gamma_1 \times \left[\left(\frac{300}{T}\right)\exp\left(\frac{-644}{T}\right)\left[\frac{1}{\left(494.4-f^2\right)^2+4f^2\gamma_1^2}+1.2\times10^{-6}\right]\right]$$

where k_{H_2O} is in dB km^{-1}, the frequency considered f and the linewitdh parameter γ_1 are in GHz, T is in Kelvin, ρ_v is in gm^{-3} and P is in mbar.

Oxygen absorption coefficient

Except for water-vapor variations, the relative composition of the atmosphere is fairly constant up to 90km above sea level. The oxygen concentration is then considered 0.21 by volume.

The microwave absorption spectrum of oxygen consists of a large number of absorption lines spread out over the 50-70GHz frequency range and an additional line at 119GHz. Below 45GHz the contribution of the 119GHz oxygen absorption line may be neglected. The absorption coefficient can be obtained with the formula

$$k_{O_2}(f) = 1.1 \times 10^{-2} f^2 \left(\frac{P}{1013}\right)\left(\frac{300}{T}\right)^2 \gamma \times \left[\frac{1}{(f - f_0)^2 + \gamma^2} + \frac{1}{f^2 + \gamma^2}\right]$$

The linewidth parameter γ is given in GHz by

$$\gamma = \gamma_0 \left(\frac{P}{1013}\right)\left(\frac{300}{T}\right)^{0.85}$$

where γ_0=0.59.

Total atmospheric gaseous absorption and emission

The total gaseous absorption coefficient is given by

$$k_g(f) = k_{H_2O}(f) + k_{O_2}(f)$$

Assuming cloud-free conditions and nonscattering atmosphere the opacity of an atmosphere layer with height z' can be written as

$$\tau(0, z') = \int_0^{z'} k_a(z) dz$$

and the downwelling atmosphere radiation at height z' along a path at a zenith angle θ.

$$T_{DN}(\vartheta) = \sec(\vartheta)\int_0^\infty k_a(z')T(z')e^{-\tau(0,z')\sec\vartheta}dz'$$

The final sky brightness can be then computed with the cosmic radiation correction

$$T_{SKY}(\vartheta) = T_{DN}(\vartheta) + T_{COS}e^{-\tau(0,\infty)\sec(\vartheta)}$$

where T_{COS}=2.7K.

The exponential shape of the sky brightness temperature, for different scenarios is shown in figure 4.5

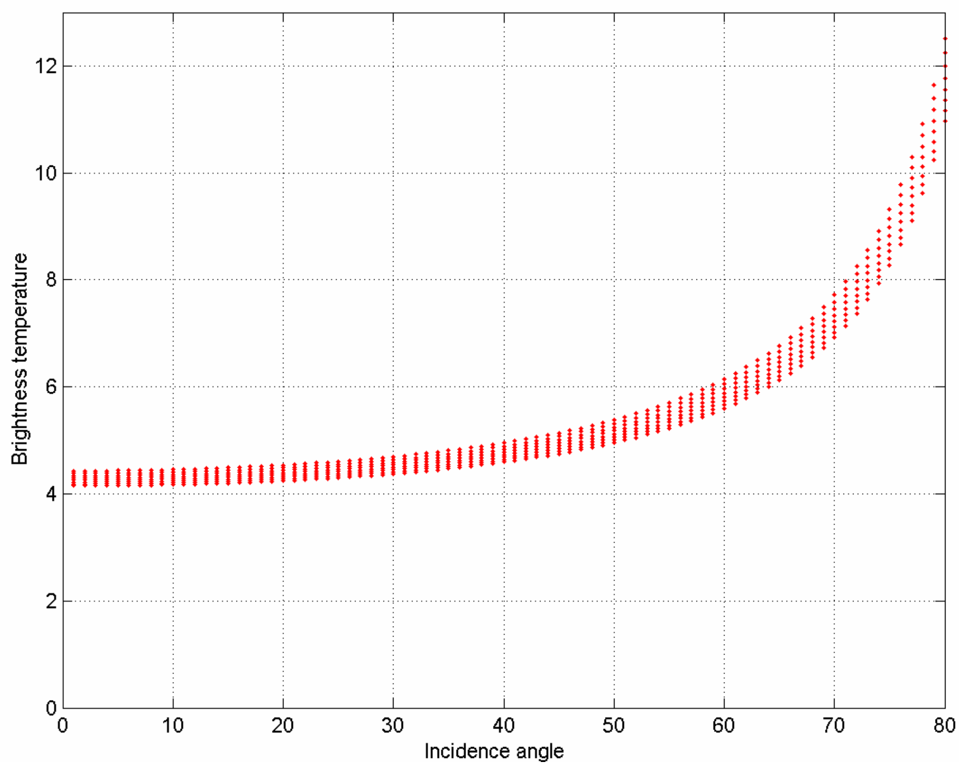

Figure 4.6 Modeled sky brightness temperature versus the incidence angle for different soil temperature and water vapor density at sea level

4.3 Calibration

As described in the previous paragraphs, six PLMR observations have been collected every day for calibration purposes. These observations are available for six different beams and both V and H polarization. The aim of this section is to perform individual calibration for each beam, each polarization, and each day. To find a calibration means to choose the best combination of the collected calibration points in order to obtain the most reliable linear regressions to correct the raw soil brightness temperature.

The easiest approach to the calibration would have been using the all six points. Nevertheless, the points collected during the flight have been considered not suitable for the analysis: in fact, the water points are not available for the whole period of the campaign, and using them just for a part of the calibration would affect the consistency over time of the general results. Moreover, the sky in flight observations has been available every day but only for the extreme beams; the need to keep consistency between the beams makes these data not suitable for the analysis.

The four ground-points have been then used as first calibration since they have been collected in controlled conditions and thus they are the most reliable ones. This is truer for the pre-flight points, since the post-flight ones can be influenced by the fast change in instrument temperature passing from the sky to the ground. This issue has been investigated during this study, but it has shown such an unsteady influence that a real temperature correction has not been developed. Moreover, it has to be noticed that typically this effect involve errors smaller then 0.5K.

A possible problem of the four ground-points calibration is that it does not take into account any flight point. This means that flight conditions like thermal changes or bumping flight conditions, which could affect the radiometer functioning, are not considered.

In order to check whether the four points calibration can be reliable for in flight measurements the water data have been used as testing series.

The calibrations have been applied to the water brightness temperature measures and the obtained points have been compared with the raw ones. To make this test manageable the water observation have been converted to nadir thanks to the formula

$$T_B(0) = \frac{e_0}{e_\theta} T_B(\vartheta)$$

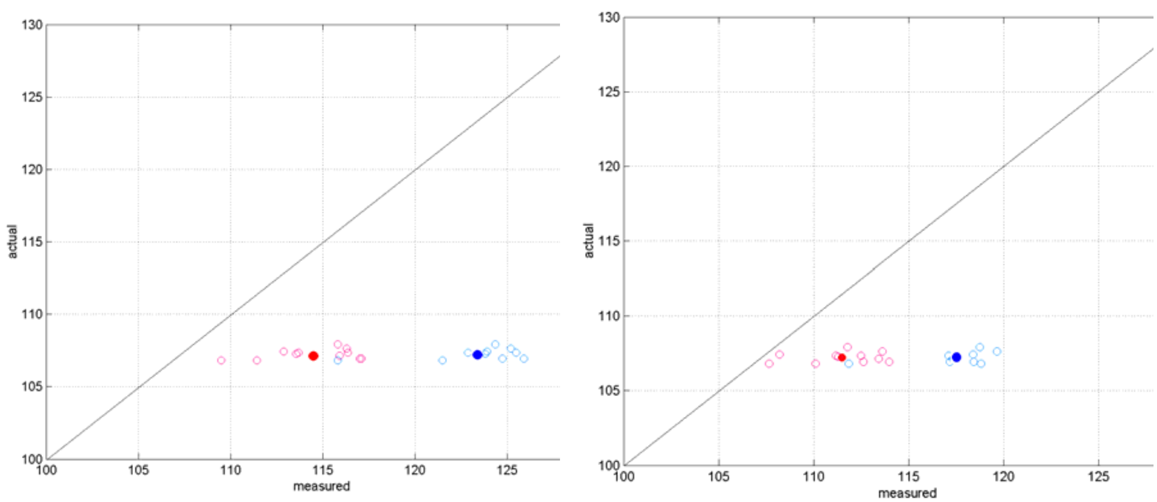

Figure 4.7 Uncalibrated and calibrated water-points for the H and V polarization.

As expected, the calibration-corrected water observations are closer to the real values. The average improvement due to the calibration is shown in Table 4.2.

Table 4.2 Average results of the first calibration test.

	uncalibrated	calibrated	actual	correction	%	error left
H polarization	123.6 K	114.6 K	107.2 K	9 K	55	7.4 K
V polarization	117.4 K	111.9 K	107.2 K	5.5 K	54	4.7 K

Even if the calibration seems to increase the reliability of the measures, the errors left are still bigger than what has been set as goal in the first paragraph of this chapter.

A second attempt for retrieving a calibration has been to use two box points and the water one. The lack of water data on some days affects the usefulness of this option. Nevertheless, if this approach had been successful, the water data could have been retrieved using thermal infrared measurement and guessing a lake salinity, which has shown fairly slow changes. The three points calibration have been developed and tested on the in-flight sky observations as done with the previous attempt.

The average results are shown in Figure 4.9 and Table 4.3.

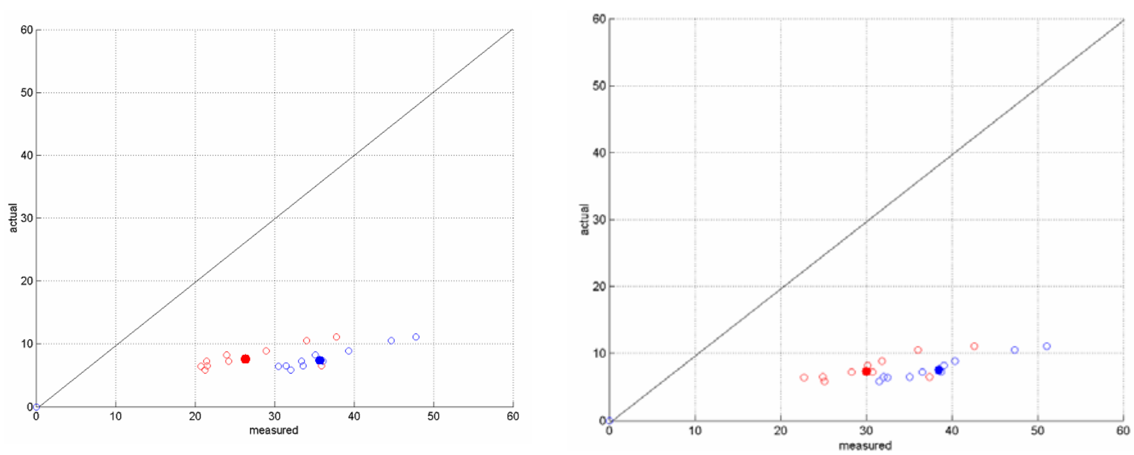

Figure 4.8 Uncalibrated and calibrated sky-points for the H and V polarization

Table4.3 Average results of the second calibration test

	uncalibrated	calibrated	actual	correction	%	error left
H polarization	35.8 K	26.2 K	8 K	9.6 K	35	18.2 K
V polarization	38.4 K	30.0 K	8 K	8.4 K	27	22 K

The error left in this case is even worst. This analysis could be affected by a fairly unreliable training series, which has been collected in ”bumpy” flight condition.

The two proposed calibrations have then been compared using as criteria the difference in calibrated values obtained for hypothetical measures of 250K and 300K, which are two extreme values for the whole campaign. The figure 4.8 shows the distribution of the error that occurs when switching between the two calibrations. It can be noticed how the error generally increases for both the polarization at 250K. At 300K the two calibrations are fairly similar, and this can be easily explained since both of them use the box points.

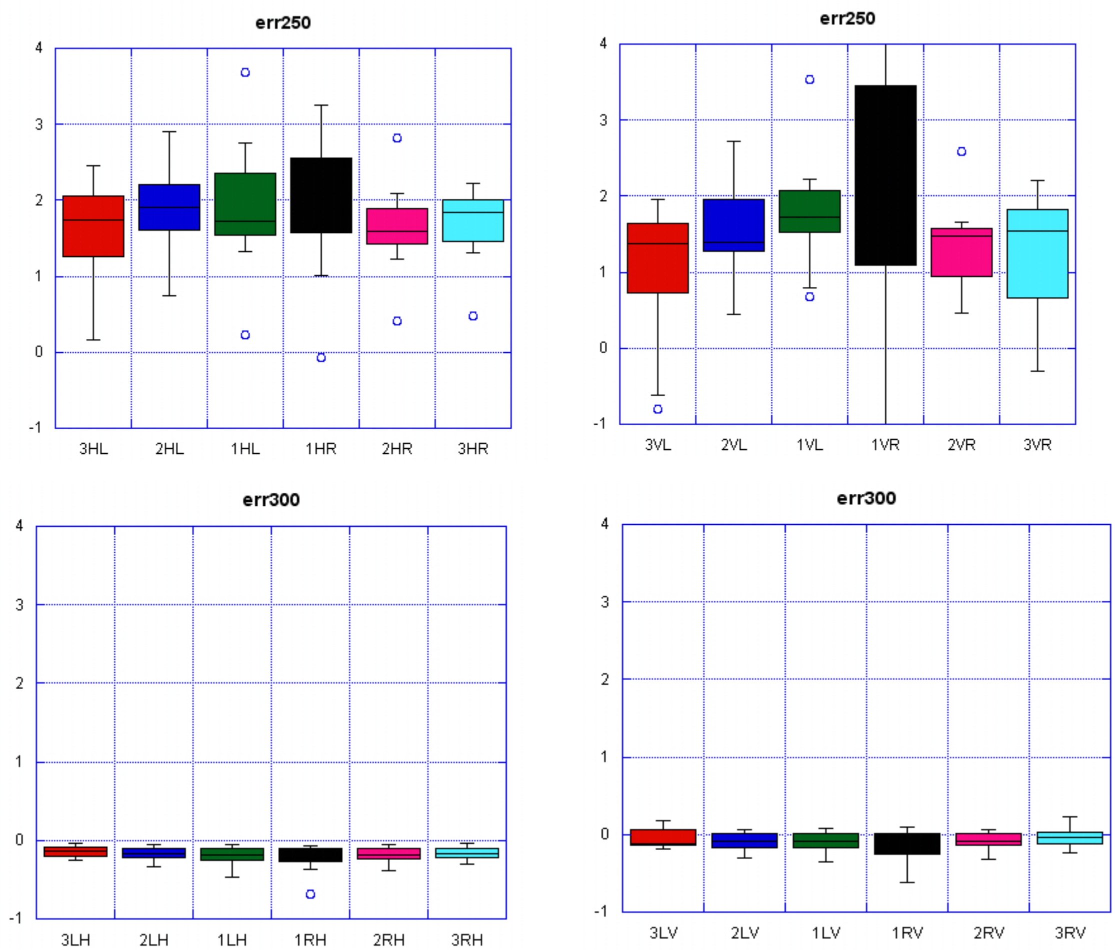

Figure 4.2 Percentile error distribution switching from the first to the second proposed calibration.

Further analyses have been done in order to understand whether simpler calibration under a logistic point of view could have been equally reliable.

The possibility of a two-points calibration, collecting ground point only once a day before the flight has been investigated using the same approach just shown. The results shown in Figure 4.9 say that especially for the H polarization this approach seems to be practicable, whereas for the V polarization the error in the observation can increase of a few K and the four-points calibration is then recommendable.

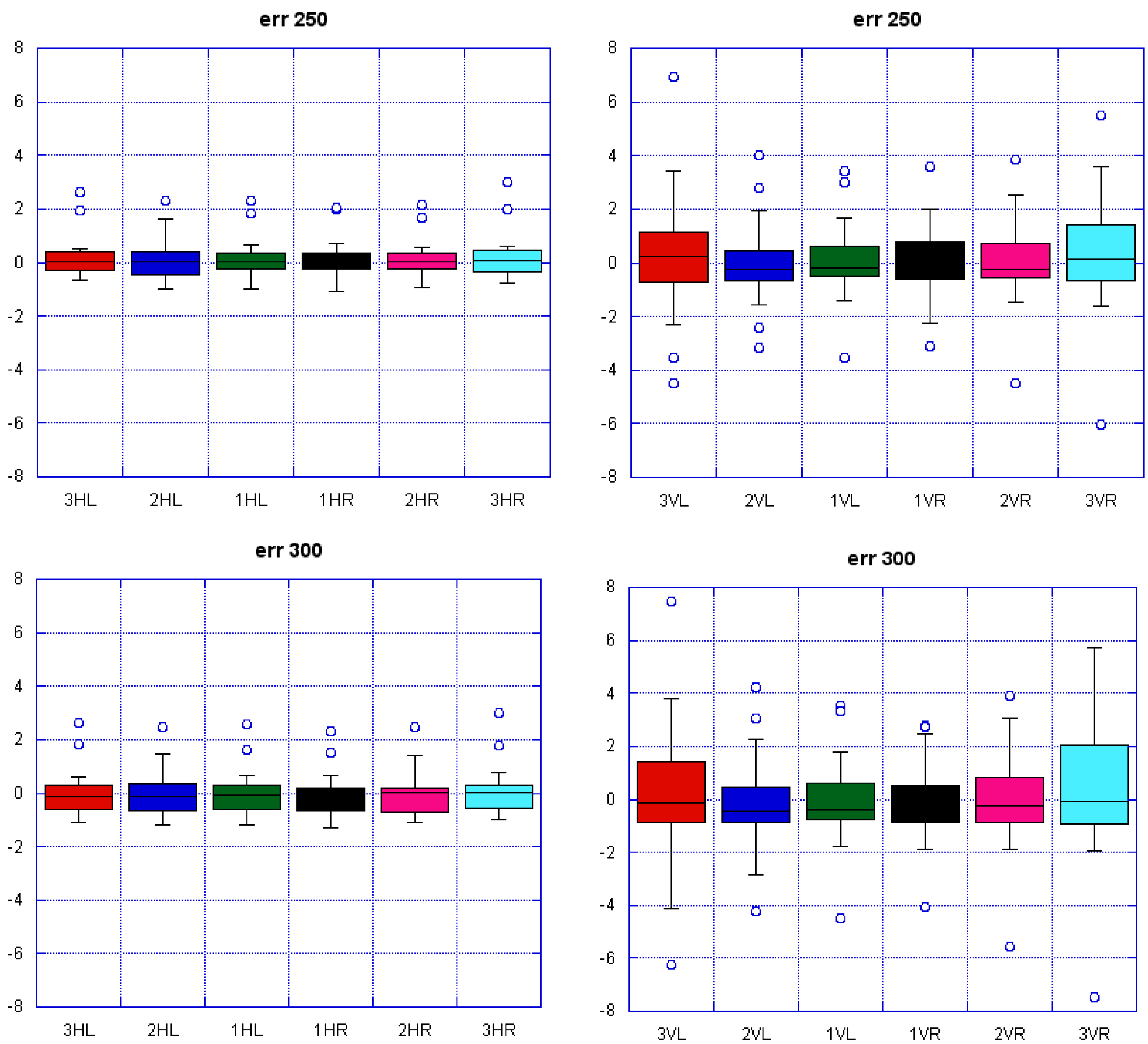

Figure 4.10 Percentile error distribution switching from the four-points to the two-points calibration.

A further possibility, investigated for future use, is whether it is possible to apply a unique calibration over a monthly measurement campaign. Again, the same approach has been used and results are shown in Figure 4.10.

Once more, the H polarization shows a more stable behavior and a unique calibration for the whole campaign could have been actually used. The V polarization at the other side needs definitely a daily four points calibration in order to achieve the proposed reliability or at least get close to it.

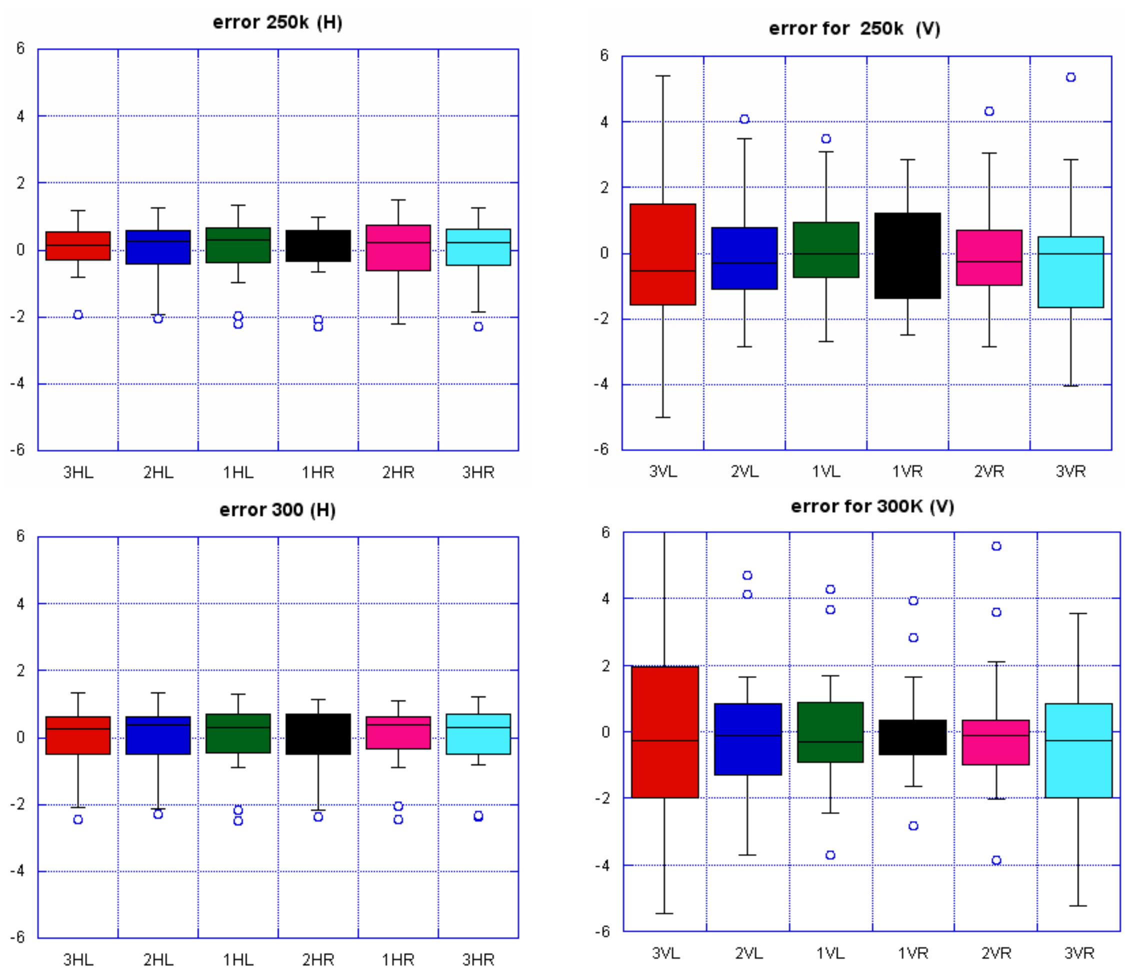

Figure 4.11. Percentile error distribution switching from the daily to a unique calibration.

No further investigation seemed to be promising. Then the four-point calibration has been chosen for the NAFE ‘05 data and proposed for future similar campaign, for both V and H polarization. This choice has the following motivations:

- The in-flight points contain more information about flight condition, but the lack of data in the time series would affect strongly the calibration.

- The ground data for the four-points calibration are available for the whole campaign.
- The box-points seem to be such reliable pivotal points that all the possible configurations using them look good.
- Even if the H polarization can be calibrated with just two-points, the V polarization is a limiting factor, needing the four-points calibration.
- The unique calibration for the monthly campaign could be feasible for the H polarization, but again the V polarization is a limiting factor since his higher instability, and a daily calibration is required.

As outcome of this investigation, daily series of georeferenced brightness temperature points has been obtained. These series are coupled with ancillary information of the incidence angle, which is a fundamental input for the soil moisture retrieval model as well.

5

SOIL TEMPERATURE

The soil temperature T_{soil} is used to normalize the brightness temperature T_b detected by the L-Band radiometer and obtain a value of the soil emissivity, following the law T_b=e T_{soil} as described in Chapter 3. In this study, T_{soil} is interpreted as the temperature of the top 5cm of soil.

Soil water content and soil temperature are both main factors in determining the ground surface emission in the microwave domain. If the purpose is to retrieve the soil water content from passive microwave observations, an estimation of the soil physical temperature is then required offline.

A viable option for estimating the top 5cm of soil temperature is by airborne thermal infrared observation of the ground surface. The process is not straightforward due to the not linear relationship between soil skin temperature detected by the radiometer and the top 5cm soil temperature. This relationship has been therefore investigated in this chapter. The result of this section is the development of a linear regression between the two quantities modulated by time-dependent parameters.

Furthermore, images from the Thermal Imager mounted on the aircraft have been used to develop maps of soil temperature for the area of interest.

5.1 Objectives

The method to estimate the top 5cm soil temperature (T_{soil}) over an area of interest is presented in this chapter.

The physical temperature over the top 5cm of soil is adopted to normalize the measured brightness temperature at L-Band and obtain a value of soil surface emissivity. This emissivity is in turn modelled as dependent on soil water content. One approach is to estimate soil temperature from soil moisture and temperature sensors at different depths, but point data are very rare and generally widely spaced, meaning that estimation of the top 5cm soil temperature with this approach would lead to poor information on spatial variability.

A different approach would be to measure temperature using a thermal infrared (TIR) sensor: TIR is frequently observed from airborne and spaceborne platform and its global application is relatively easy, though atmospheric effects due to water vapour need to be taken in account. This approach is the one used in this study, by relating the TIR measurements with the top 5cm soil surface temperature.

A relationship between temperature T_{TIR} detected by thermal infrared at ground level and the temperature of the top 5cm of soil (T_{soil}) has been developed on the base of the data collected in the field campaign by the stations described in Chapter 2.3.2.

To capture the spatial distribution of soil temperature during the NAFE'05 field campaign, the SERA aircraft was equipped with a digital thermal imager, mounted in a pod under the wing, which provides snapshot images of the ground in parallel with the L-BAND radiometer. The acquisition frequency for the thermal imager was of one shot per second.

The relationship between T_{TIR} and T_{soil}, extrapolated using data from the ground station, has been applied to the images of the thermal camera, to have an estimation of the top 5cm of soil over an area of interest.

5.1.1 Accuracy required in soil temperature estimation

A preliminary study was conducted to assess the accuracy required in the estimation of soil temperature in order to achieve a 4% accuracy in soil moisture retrieval: the 4% is the proposed goal for the future SMOS mission. Fig. 5.1 shows the results of this analysis, and indicates that for extreme moisture content conditions soil temperature must be estimated with an error lower then 4K (very dry) and 7K (very wet), meanwhile in standard conditions that error can be higher (8K).

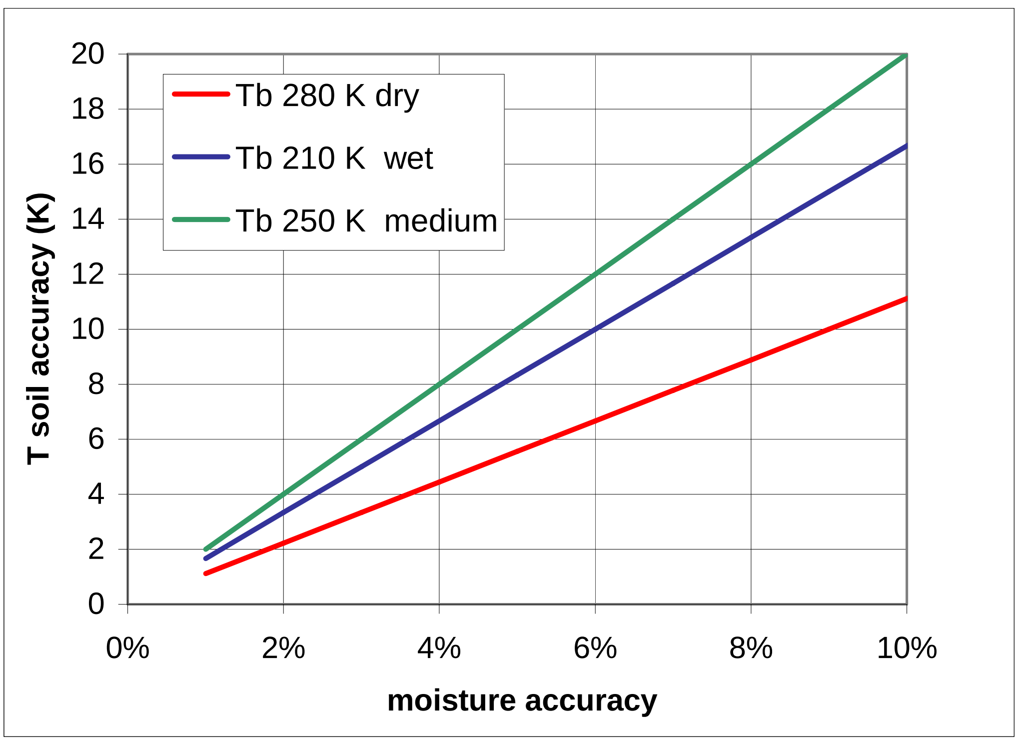

Figure 5.1: T_{soil} accuracy required for the estimation of soil moisture

5.2 Ground instruments

To develop a relationship between thermal infrared observations and near-surface soil temperature, thermal infrared data were recorded by 4 radiometers (two Ahlborn Thermalert TX® and two Everest Interscience Inc.® Infrared Temp Transducers, Model 4000) mounted on 2m tall towers at four different sites. At each site, 3 soil temperature sensors were installed within the TIR device field of view (FOV) at 1cm, 2.5cm and 4cm (Unidata® 6507A/10 sensors). These stations have been operative for the entire month of November (i.e. the whole duration of the field campaign), and logged temperature values every 20 minutes. Their location was carefully chosen so as to capture the dominant land covers of the study area, specifically bare soil, wheat, lucerne and native grass.

Figure 5.2: An example of installation during NAFE' 05

Technical features of the thermal infrared devices are shown in the table 5.1:

Table 5.1: Technical features of the thermal infrared device

	Ahlborn Thermalert	Everest Interscience
Spectral response	8-14 μm	8-14 μm
Accuracy	± 1% of reading	±0,5% of reading
Temperature resolution	0,1K	0,5K
Output	mA	mV

The two sensors have also different FOV: the Ahlborn Thermalert, from 2m tower, can detect the radiation emitted from a circular portion of the ground surface approximately 50cm in diameter, while the Everest Interscience, from the same height, measures the radiation of a target 1.5m in diameter.

Since the devices have different output, a calibration is required to compare the results of the data collected. Laboratory calibration was conducted prior installation and repeated at the end of the campaign to detect any malfunctioning. The following paragraph describe the calibration procedures.

5.2.1 Calibration of the thermal infrared sensor

The four infrared devices were set to target a basin of water with submerged Unidata® sensors to control the physical temperature of the target. A large range of temperature was cover adding boiling water or ice: a logger connected to all sensors provided the dataset record.

A linear regression for each Thermal Infrared Sensor was thus calculated: these relationships convert the output of the devices (mV and mA) into Celsius degrees.

$$T_{TIR}(\,^{\circ}C\,) = slope \times (mA \text{ or } mV) + offset.$$

Table 5.2 reports the value calculated.

Cleary, a calibration using a black body would have given more accurate results but, for the purpose of this study, the approximation for water emissimity equal to one is considered appropriate. Furthermore, the same assumption will be established for natural surface as vegetation and soil.

Slope and offset are show in the table 5.2 with the RMSE of the calibration.

Table 5.2. Calibration parameters for the thermal infrared devices

Device n° & location in the campaign	Slope	Offset	RMSE
1 Lucerne	6.211	- 48.147	0.40
2 Native grass	4.925	- 32.517	0.25
3 Wheat	0.115	- 3.259	0.18
4 Bare soil	0.116	- 3.812	0.17

The plots in fig 5.3 show the calibration curve: devices n°3 & 4 have a more homogeneous behaviour compared with the first and the second, probably due to more recent production.

The temperature calculated from this calibration will be called T_{TIR}.

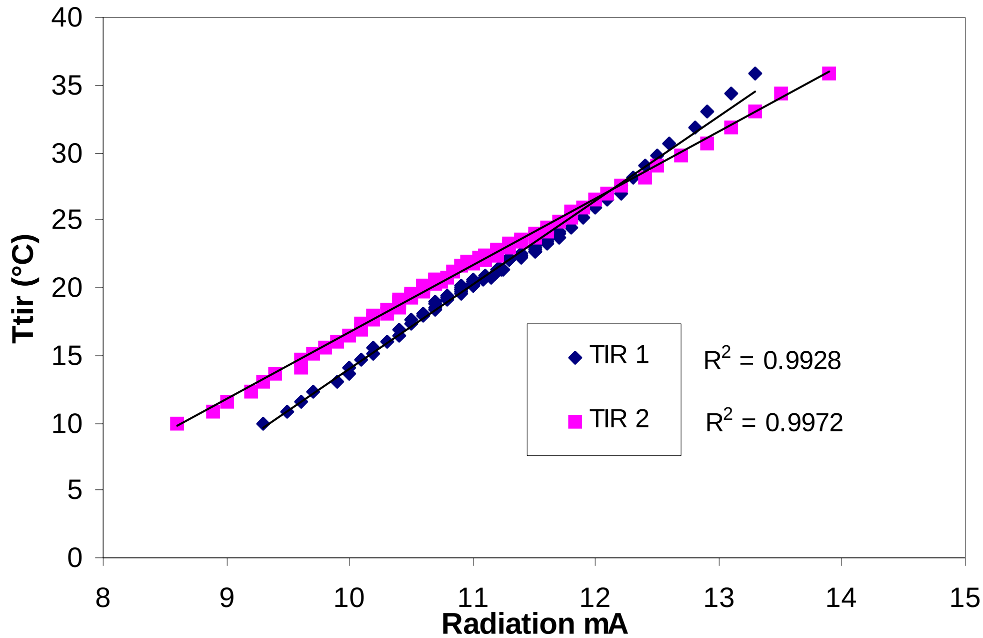

Figure 5.3(a): Calibration curves for the radiometers 1 and 2

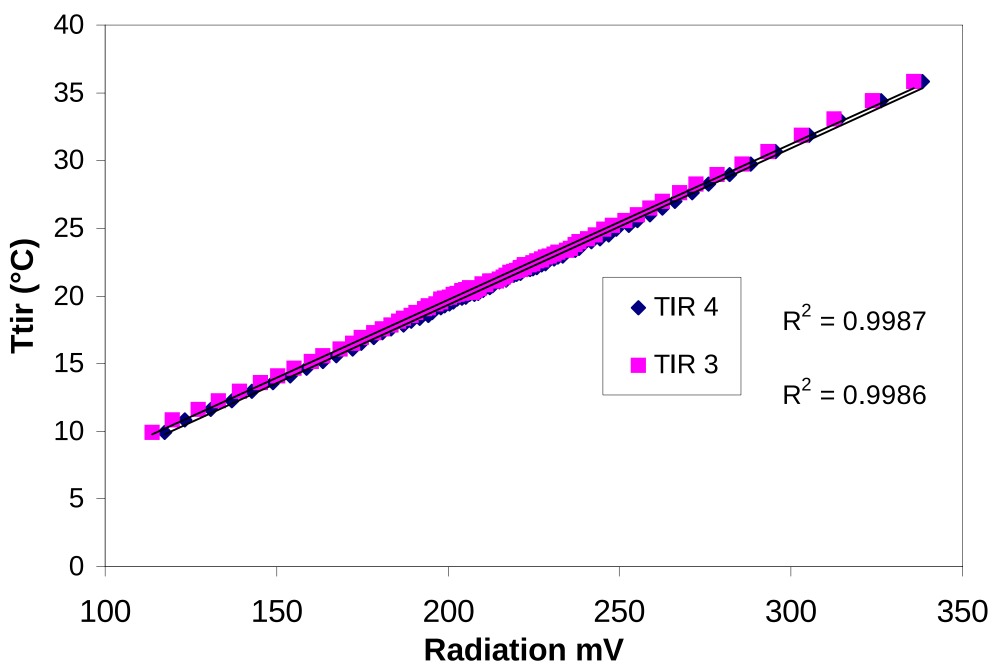

Figure 5.3(b): Calibration curves for the radiometers 3 and 4

5.3 NAFE campaign data

This section presents a brief overview of the data collected during the field campaign. Table 5.3 shows the amount of data successfully recorded.

Table 5.3. Days successfully recorder (out of 31) for infrared devices (TIR) and for buried thermometers (Tsoil).

	TIR	T soil
Lucerne	17	17
Native	6	30
Wheat	26	26
Bare soil	29	30

As can be noticed, the TIR on native grass was damaged early in the campaign, probably by rain, while on the lucerne, the devices stop working due to a "cow attack". A typical trend of data collected is shown in Fig. 5.4, in Appendix E all the stations.

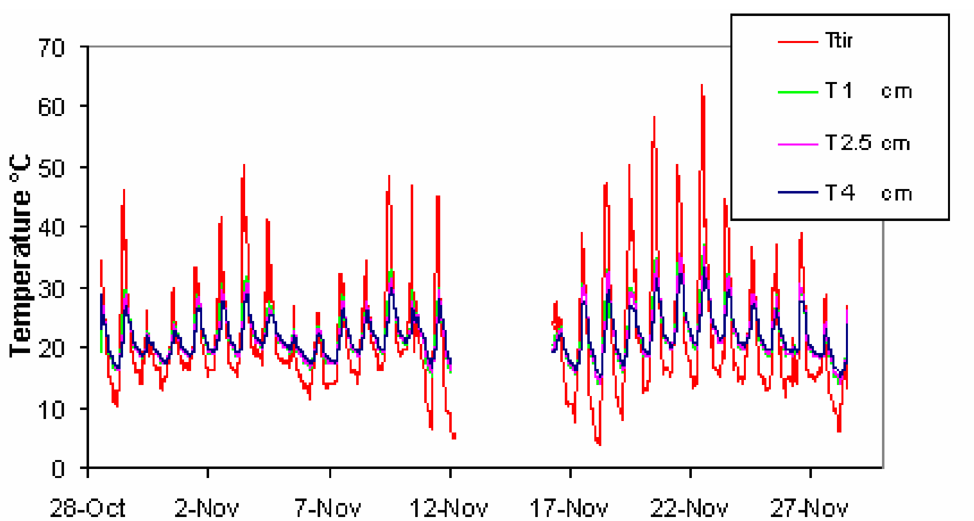

Figure 5.4: Data collected at the station on wheat

The red line in fig. 5.4 represents the temperature T_{TIR} calculated from the thermal infrared device applying the calibration showed in the previous paragraph: as expected T_{TIR} overestimate the amplitude of the diurnal soil temperature cycle, reason why a relationship needs to be applied to correct these values and obtain a value of T_{soil}. In the model for soil moisture retrieval, only a value of soil temperature is used to normalize the brightness temperature: hence is necessary to choose which, amongst the soil temperature measurements at different depths, is more representative of the 5cm soil layer and more suitable to be fed into the soil moisture retrieval algorithm.

The approach chosen here is to consider a weighted average of the measured value on the basis of the thickness of the layer represented:

$$T_{soil} = T_1 \times 1.75 + T_{2.5} \times 1.5 + T_4 \times 1.75$$

Where T_1, $T_{2.5}$, T_4 are the temperature detected at the indicated depth.

5.3.1 Ground temperature sensors

Diurnal variation in soil temperature is affected by the nature of soil, type of surface cover and incoming radiation. Figure 5.5 shows diurnal soil temperature at 3 depths in a clay soil for a given day of the campaign and the calculated T_{soil}, as show in the previous paragraph.

As shown in the plot, before sunrise the soil temperature is lower at the surface and increases with depth. Because of the lag time associated with soil heat flux when the surface temperature is changing, at higher depths the soil temperature continues to cool down for a certain period of time after the heating of the surface due to the sun start, and the opposite trend is encountered in the afternoon.

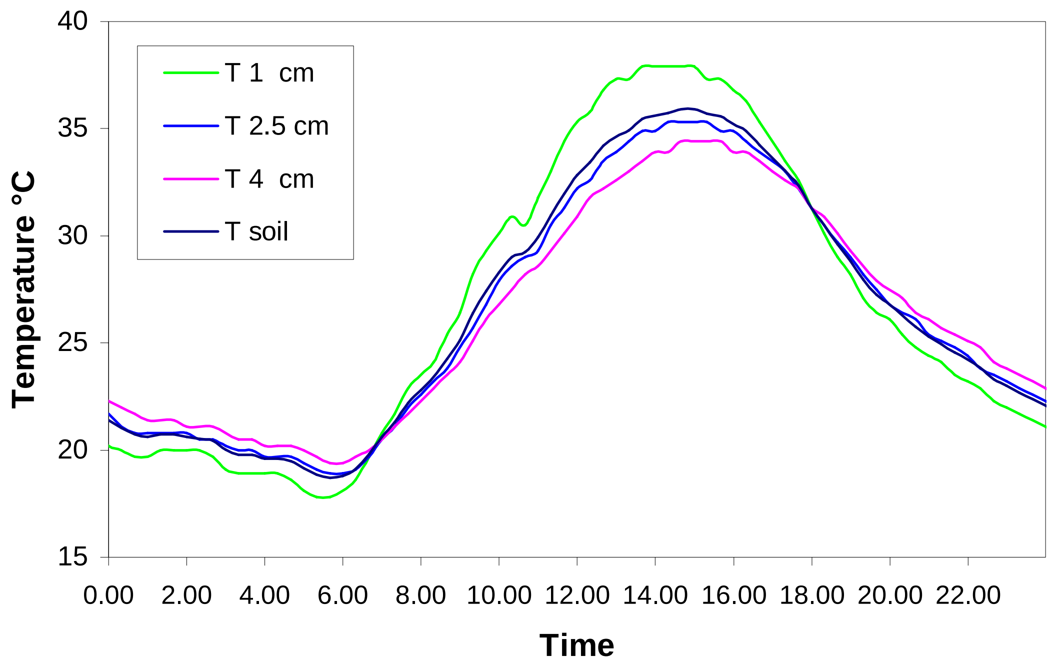

Figure 5.5: Trend of soil temperature at different depths

The difference in temperature measured between the shallowest and the deepest thermometer can rise up to 10 degree during the warmest hour of the day. In dry condition this effect is more accentuated. The thermometers at 1cm depth are subject to greater variation in 24 hours compare to the deeper ones.

For the purpose of this study, we assume appropriate the weighted average between these tree devices to obtain a value of T_{soil}, assumed as representative of the physical temperature for the first 5cm layer.

5.4 Relationship between T_{soil} and T_{TIR}

This section analyzes the relation between temperature measured by thermal infrared and by thermometers in the ground. Fig. 5.6 shows the typical daily trend for T_{soil} and T_{TIR}.

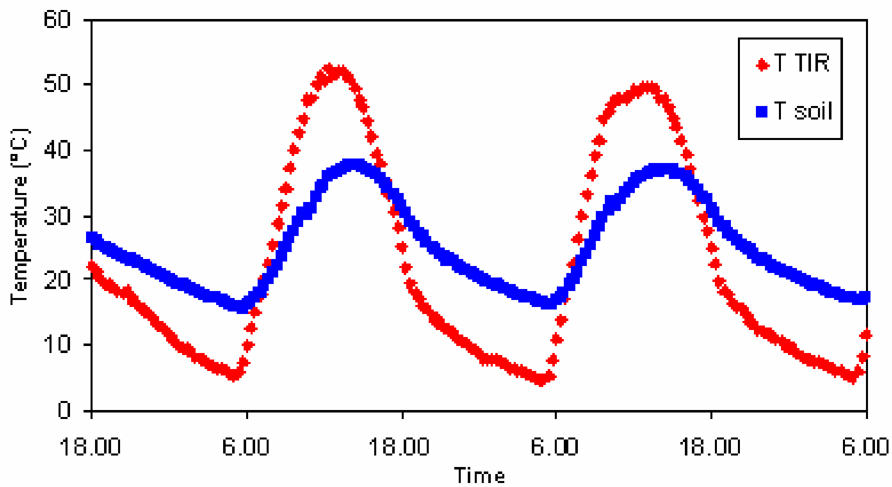

Figure 5.6. Trend of Tsoil and T_{TIR}

Considering the thermal infrared temperature as surrogate for the soil top 5cm temperature would lead to overestimation during the hours with sunlight and to underestimation at night. A time lag is evident between the two curves; although this information would be important in the contest of temporal modeling of surface temperature, its importance for remote sensing application is reduced since more than a prediction of the dynamic of the soil temperature, the value of the soil temperature is required at the moment of the correlated observation. It can be roughly stated that the information given by thermal infrared measurements "anticipates" the thermal response of deeper layers of soil, but that is of no importance for our application, given that the airborne TIR measurement that will be used will be a "snapshot" in time of the surface, without information on the antecedent conditions.

5.4.1 The diurnal cycle

The data collected, can be visualized also as T_{soil} function of T_{TIR}, as shown in Fig 5.7

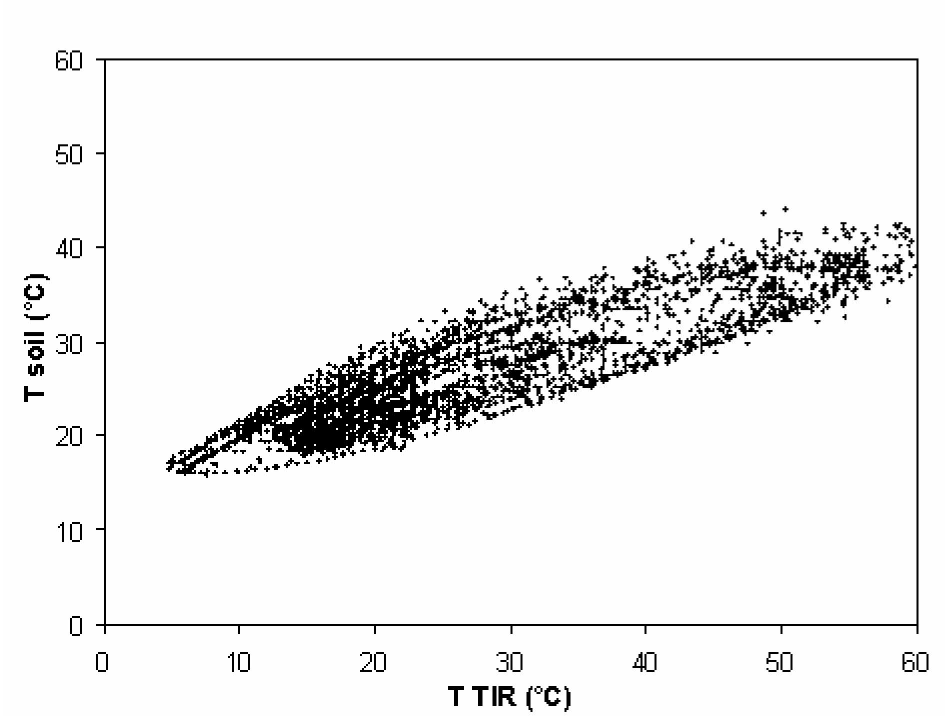

Figure 5.7: Relationship between T_{TIR} and T_{soil}

The relationship clearly presents a hysteretic behaviour, which has to be related to the solar radiation. If we split the data into two series, one with records between 5AM and 2PM and the second with the remaining data, the two series lie on the two arcs of the hysteresis cycle (Figure 5.8).

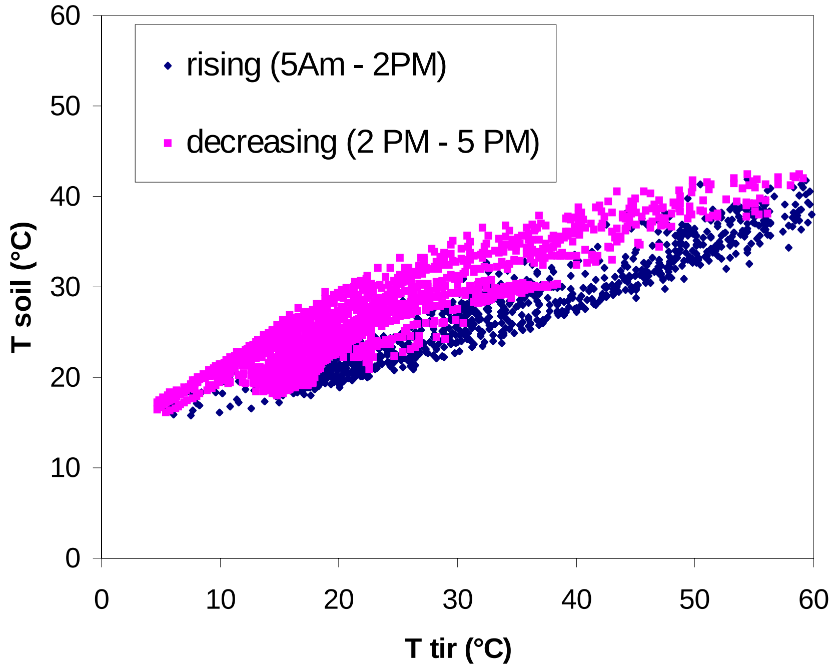

Figure 5.8: The hysteresis arcs.

An interpolation curve can be fitted for the two arcs but the level of scattering is very high: the next section analyses the impact of the soil moisture on the cycle.

5.4.2 The impact of soil moisture on the diurnal cycle

The presence of water plays an important role in mitigating the excursion of soil temperature because of its high heat capacity, which is the capacity of a substance to store heat. The plot in figure 5.9 shows the relation between moisture content, detected with the SAMSAS permanent station, and the daily range of temperature collected under native grass coverage.

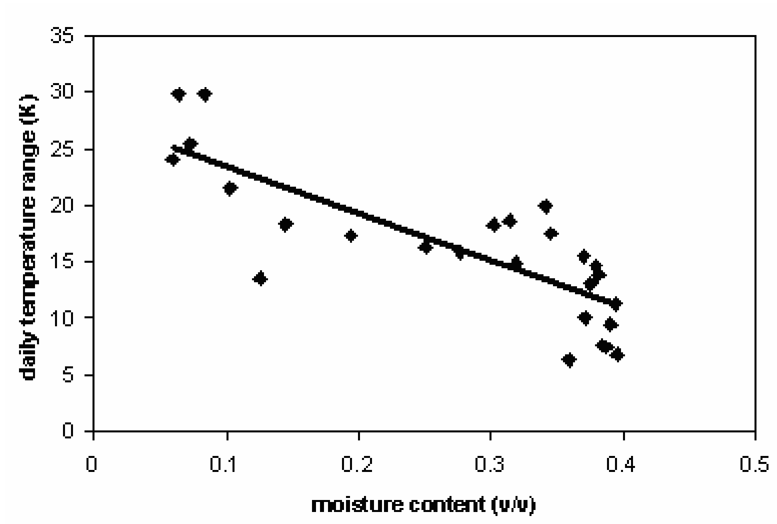

Figure 5.9. Range of daily temperature as function of soil moisture

The soil moisture dependence of the arcs of the hysteresis cycle was explored and it is shown in plot 5.10 for the "raising" series.

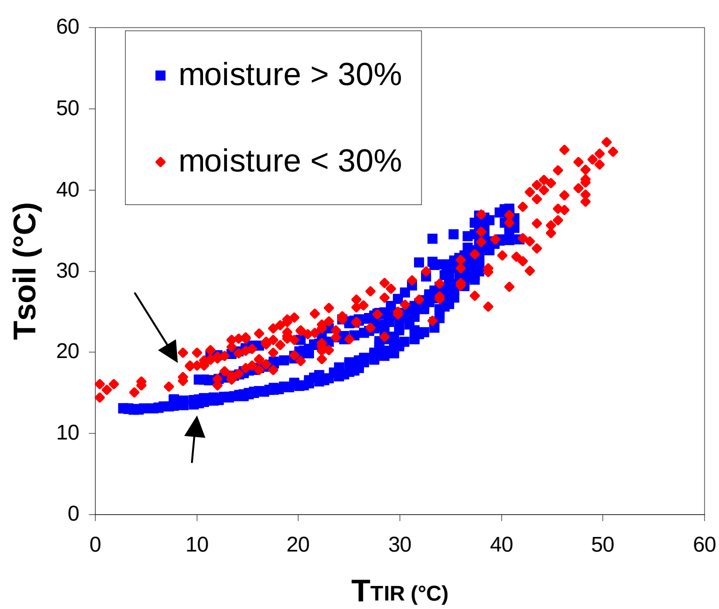

Figure 5.10: The raising series with soil moisture effect

For low value of moisture content, the range of temperature recorded is higher than for moisture content greater than 30%. In this case, it is interesting to note that the distance between the blue lines for a range of T_{TIR} between 10ºC and 25ºC (see the arrow) can result in a T_{soil} varying of 10ºC

5.4.3 Vegetation coverage effect

Vegetation cover also affects this relationship: thermal infrared stations placed on different vegetation types present different responses to the ground signal. This is mainly due to two reasons:

- Different types of vegetation can have a different temperature and furthermore different emission in the thermal infrared band
- The amount of bare soil that the devices can detect is related to the fraction of vegetation coverage: high value of canopy coverage normally leads to lower radiation from the ground.

Soil and vegetation temperature data were collected once for each farm with thermal infrared gun in the late morning AND/OR early afternoon. Commonly, vegetation temperature is a lower then that of soil. Nevertheless, doubts concerning the daily evolution of this ratio and the small number of data compromise the use of this valuable datasets in this study. Also consideration about the emissivity must be taken: soil emissivity is normally close to one in the wavelengths between 6 and 14 μm (*Fuqin Li et al.*, 2004) and vegetation emissivity may be estimate as 0.985 (*Sobrino et al.*, 2001). Hence the hypothesis to assume the value of emissivity equal to one for all the surfaces observed can be assumed as acceptable. The differences in the thermal infrared signals are assumed related directly to the kinetics temperature of canopy and soil: for the purpose of the study, vegetation temperature is assumed to be equal to the soil skin temperature.

5.4.4 Empirical relation T_{TIR} - T_{soil}

This section presents an empirical linear relationship between T_{TIR} and T_{soil}, which allows estimating T_{soil} from a single value of T_{TIR}, whether the time of the observation is known.

This approach has been developed from the NAFE '05 datasets; therefore care should be taken in applying them to wider scales and different study areas or climatic conditions. Additional data will be collected in 2006 in a similar field campaign to address this issue.

The proposed method interpolates the recorded data with a linear regression, considering the measurement acquired at the same time of the day (6AM, 7 AM, 8 AM, etc) during the whole acquisition period. 24 parameters for slope and intercept were found. In this way, the T_{TIR} detected will be converted in T_{soil} by a linear relationship with slope and offset depending on the time of the aircraft observation:

$$T_{soil} = slope(t) \times T_{TIR} + offset(t)$$

The approach could also be described as query based: when an observation with thermal infrared is performed, to obtain the value of the soil temperature is necessary to apply the transformation choosing parameters on the base of the time of the observation. The day has been divided in 24 parts and parameters change every 60 minutes (Fig 5.12).

The plots 5.11 show the result of the regression: different colors indicate different vegetation covers.

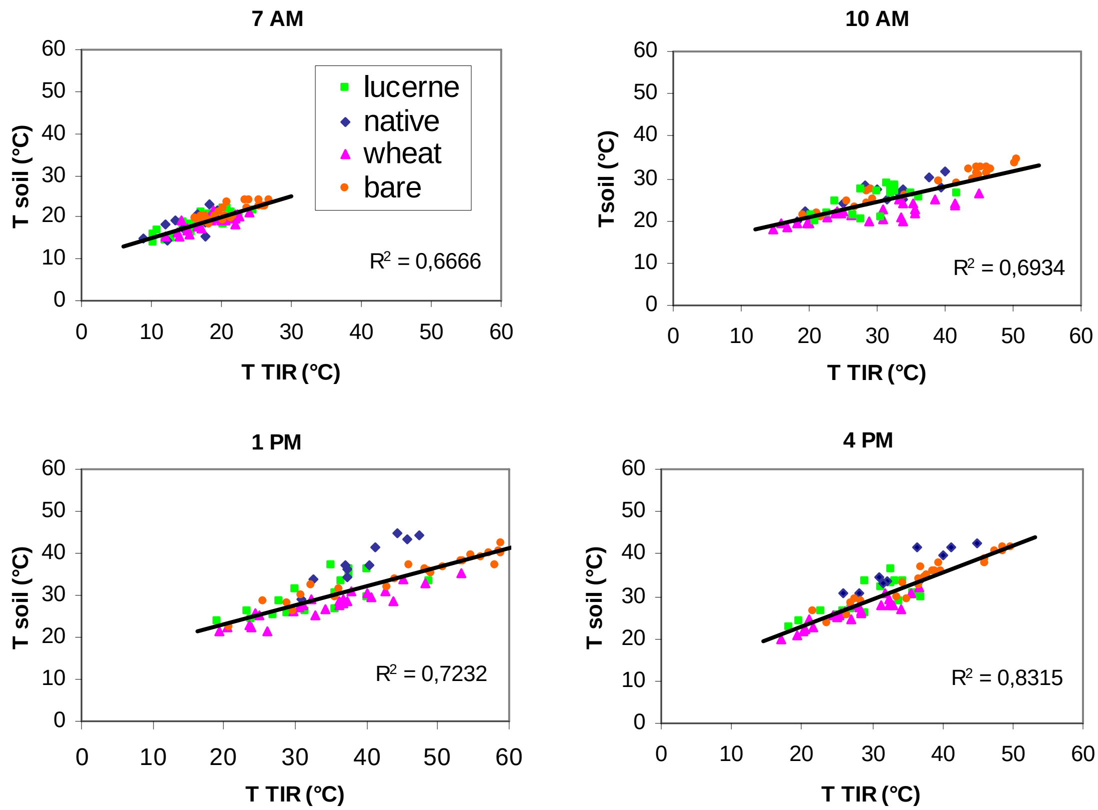

Figure 5.11: examples of liner regression for given hours of the day

The grade of scattering is more accentuated in the plot of 1PM as expected. With the sun at the zenith, differences in soil type and vegetation coverage result in different answer of the thermal infrared and soil temperature. It can be notice a light overestimation of the soil temperature on wheat (10AM, purple triangle) and an underestimation of soil temperature for native grass coverage (1PM, blue dot). It was excluded to produce different relations for native and crop, since the success of this operation would be connected to a high-resolution map of the soil use.

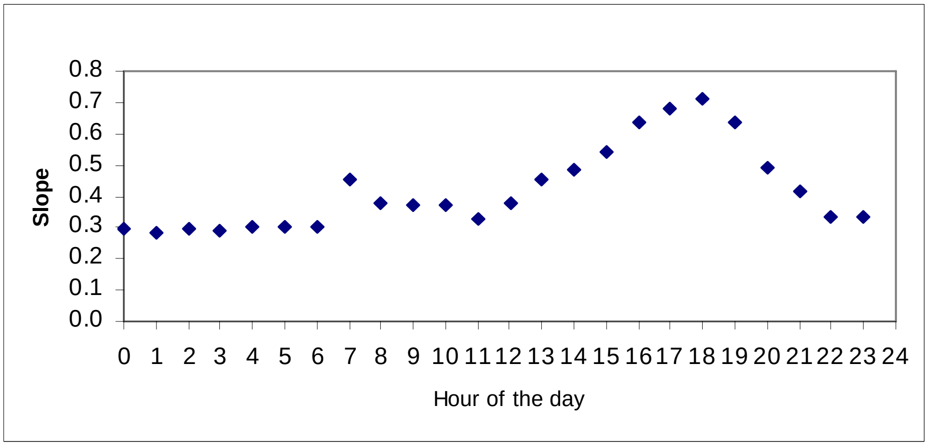

Figure 5.12(a): Slopes of the linear regression as function of time

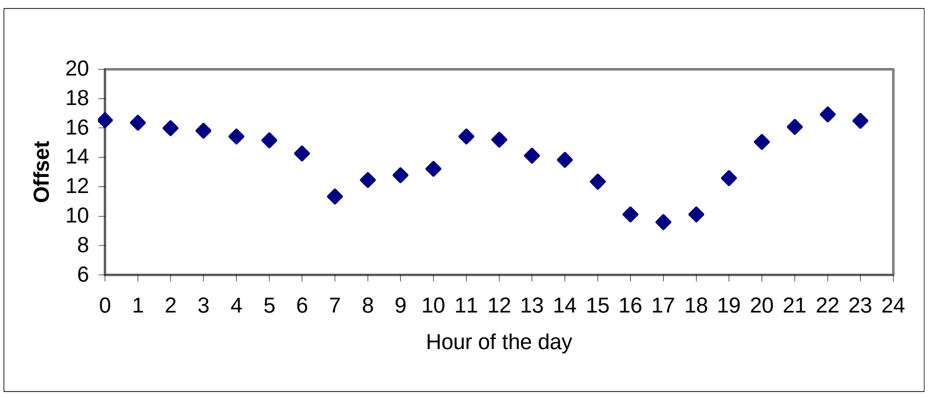

Figure 5.12(b): Offsets of the linear regression as function of time

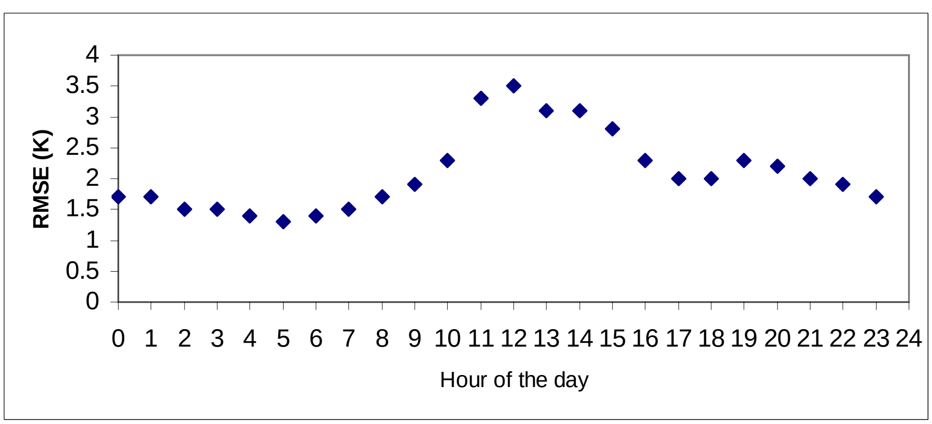

Figure 5.13: RMSE as function of time

The plot 5.13 shows the error estimating soil temperature from T_{TIR} : most of the aircraft observations in the NAFE campaign were performed between 7 and 11AM. Good accuracy in estimation of soil temperature can be reach until 10AM circa, with a RMSE < 2.5K, while higher errors can occur in the last observations.

5.5 Surface soil temperature mapping

The relationship between T_{TIR} and T_{soil} presented in the previous paragraph has been applied to the infrared temperature detected by the airborne thermal imager. A comparison between temperature detected at the ground by TIR tower and by the camera on the airplane for the same areas is show in the plot 5.14: RMSE between the infrared temperatures is 4.7K, which generates an error in the thermodynamic temperature of 2.7K, below the accuracy required for T_{soil} to retrieve soil moisture with 4% accuracy.

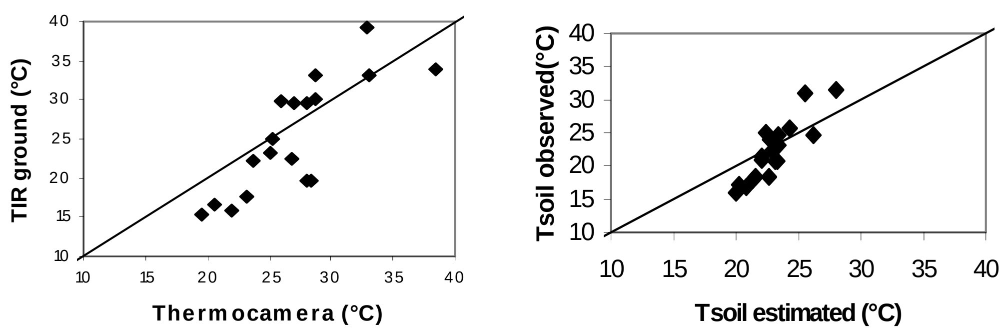

Figure 5.14: Comparison between ground TIR and thermal imager

Error in estimation of Tsoil, applying the relation shown in the paragraph 5.3, can rise up to 5K: this will affect the accuracy of the moisture retrieval but, with the available data, a clear relationship between ground TIR and airborne thermal imager was not found.

The raw thermal imager data are not georeferenced, meaning that they are not provided with attached spatial information: the georeferencing process has been conduct with software ArcMap for the area of interest, making use of ground target points of known coordinates which could be recognized in the thermal images.

A rough correction was set up to mitigate the lens distortion and further distortions at the edge of the FOV. Based on the results provided by the calibration with black body at 295K, the difference of temperature between the black body and each pixel was added to the relative pixels in each imagines before proceed with the georeferencing process. At the same time, atmospheric effect on the thermal imagines must be investigated: in the band between 8 and 12μm aerosol, absorption and scattering are negligible while water vapour is principally responsible for atmospheric effect. In fact, clouds are clearly visible in the thermal images and their effect is to totally mask the ground signal. Information on atmospheric variables, particularly air temperature and water vapour profile, are needed to perform a correction: nevertheless, for the purpose of this study atmospheric effect are not taken into account for flights below 5000ft. Maps have been produced only for clear free clouds days, and assumptions about the soil temperature in cloudy days need to be assumed.

In Fig 5.15 an example of the result of the georeferencing operation on the raw thermal imager data is presented: the Midlothian farm is “covered” georeferencing the images from thermal camera. The areas of no data at the centre of the image are due to the not perfect overlap between the areas mapped during the two consecutive flight lines. This could not be guaranteed due to the difference between the FOV of the L-band radiometer (90 degrees) and the thermal imager (80 degrees).

The map was then upscaled to a 500m and 250m spacing grid, that was subsequently to be fed into the soil moisture retrieval algorithm, allowing assignment a value of temperature to the no data areas (Chapter 7).

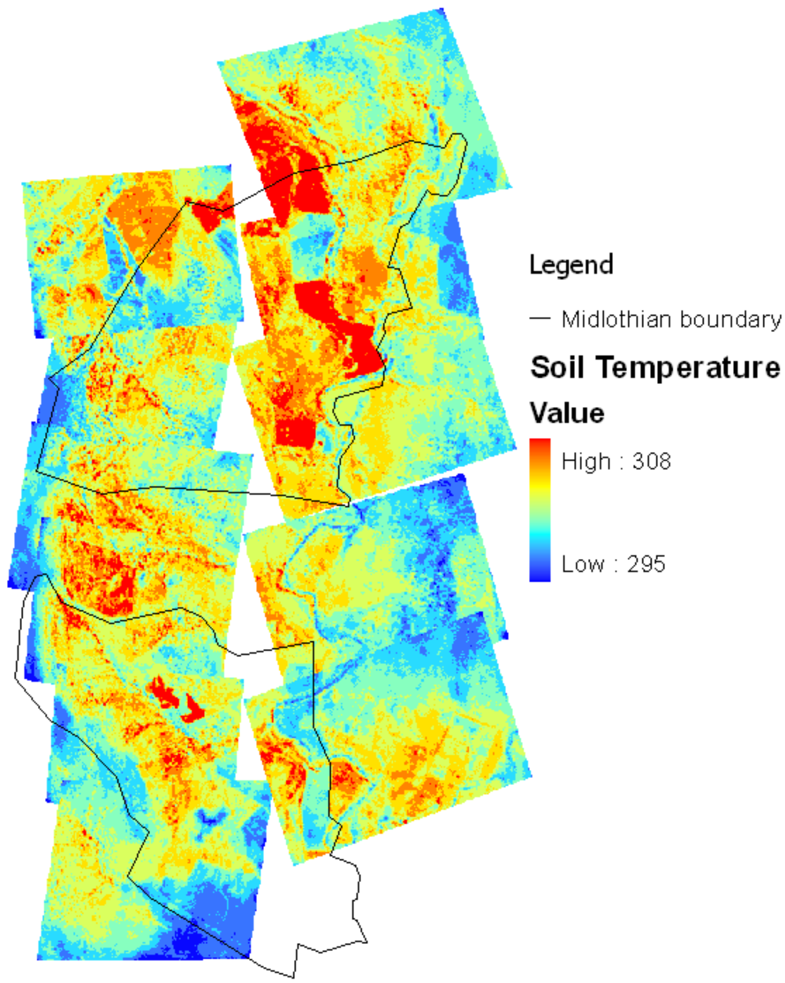

Figure 5.15: example of the georeferencing process of the images from the thermal camera

6

VEGETATION EFFECT

The vegetation layer absorbs and scatters the microwave radiation emitted by the ground surface, as well as being a source of microwave radiation itself. Vegetation effect is therefore an important factor to be considered in passive microwave soil moisture retrieval.

Vegetation effect is usually quantified through a parameter called vegetation optical depth or vegetation opacity τ. The value of τ depends on the vegetation type, the vegetation water content (VWC) and the wavelength of the radiation.

The model used in this study and described in Chapter 3 takes advantage of a previously developed relationship between τ and VWC of the form $\tau = b*VWC$ (*Jackson and Schmugge*, 1991) where *b* is an experimentally derived parameter, dependent on the vegetation type and the wavelength. Estimates of VWC and observations of vegetation type are therefore required in order to apply this model to soil moisture retrieval algorithms. This chapter shows how VWC estimates were assessed by building relationships between ground-based observations and satellite reflectance data.

6.1 Objectives

Remotely sensed reflectance data have been used to produce estimates of VWC over the study area. This was achieved by building relationships between ground measured VWC and reflectances in the visible, IR and NIR bands and subsequently upscaling the VWC to the whole study area making use of satellite imaginery acquired at the same bands.

A vegetation index (VI) that can provide estimates of VWC is typically a ratio between the difference and the sum of radiances in two different bands: a reference wavelength where the water absorption coefficient is low and a measurement wavelength where water absorption is moderate or high and the penetration into the canopy is maximized (Fig.6.1).

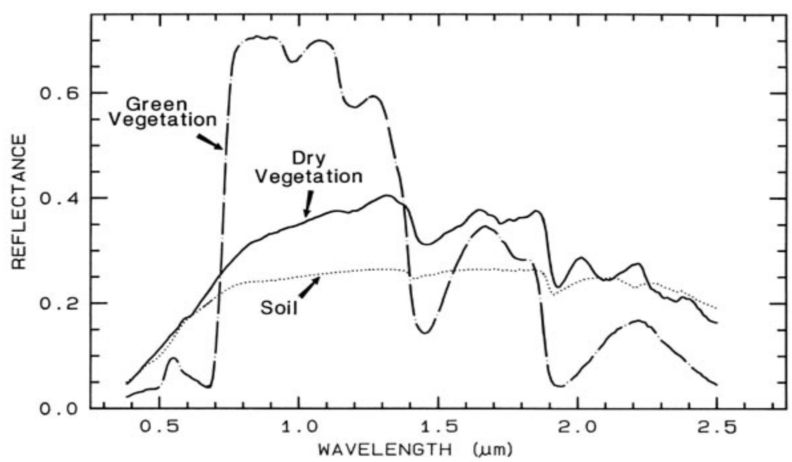

Figure 6.1: Spectral reflectance of natural surfaces

The most common VI is the Normalized Difference Vegetation Index (NDVI), and this has been the first index analyzed in this work. NDVI was proposed by *Rouse et al.* (1973) and is calculated from the near-infrared (NIR) and red (RED) bands as follows:

$$NDVI = \frac{NIR - RED}{NIR + RED}$$

The NIR ($\lambda = 858$nm) has been chosen as reference band because it is relatively insensitive to vegetation water content changes. However, several studies indicated that NDVI has a reduced sensitivity to changes in VWC in the case of dense vegetation coverage (*Gamon et al.*, 1995; *Chen and Brutsaert*, 1998), as shown in Figure 6.2. In fact, the response in the NIR and RED regions are due respectively to the high reflectance plateau of vegetation canopies and the strong chlorophyll absorption region. Therefore, NDVI may be better described as a greenness index rather then a VWC index, because it represents mostly chlorophyll content rather than water content. Therefore, it has a limited capacity for VWC estimation, considering that each plant has its own relationship of VWC and chlorophyll content and a variation of chlorophyll content does not imply a variation in VWC.

Due to these limitations, and in order to be able to capture the wide range of canopy conditions present at the Goulburn study area, an additional index was investigated, the Normalized Difference Water Index (NDWI), based on the Short Wave Infra-Red (SWIR) bands, that are water absorption dominated and, as a result, more sensitive to VWC changes (*Jackson et al.*, 2003).

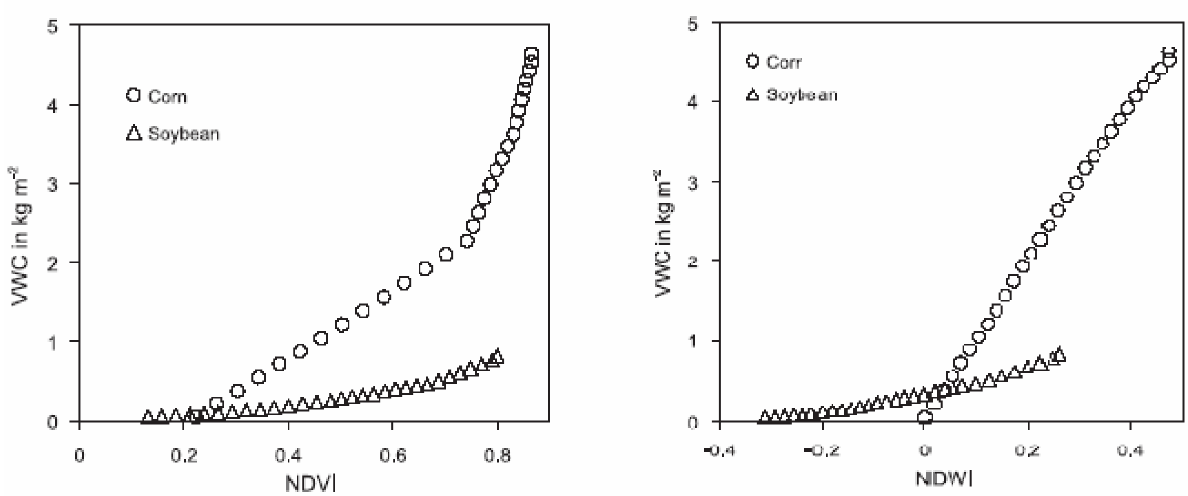

Figure 6.2: Relationships between VWC and VIs (Jackson et al., 2003)

In this study, two NDWI indices using different short wave infrared wavelengths channel have been considered:

$$NDWI_{1640} = \frac{NIR_{858nm} - SWIR_{1640nm}}{NIR_{858nm} + SWIR_{1640nm}} \qquad NDWI_{2130} = \frac{NIR_{858nm} - SWIR_{2130nm}}{NIR_{858nm} + SWIR_{2130nm}}$$

The Moderate Resolution Imaging Sensor (MODIS) on NASA's Terra and Aqua satellites provides observations at these bands at a daily time step and spatial resolution of 500m.

Land cover is also important when using NDVI and NDWI to assess VWC as the relationship varies with the vegetation type. Therefore, a land cover map of the area of interest was produced using a supervised classification that makes use of ground observation of land use and vegetation type, as it will be shown in paragraph 6.6.

Moreover, a preliminary study was conducted to assess the accuracy required in the estimation of VWC in order to achieve a proposed 4% accuracy in soil moisture retrieval that is the goal of SMOS project. Fig. 6.3 shows the results of this analysis, and indicates that for extreme moisture content conditions (very dry or very wet soil) the error that can be committed is 0.8kg/m^2; while in standard conditions that error can be higher (1kg/m^2). The different colored lines represent different soil moisture conditions: red stands for dry soil, blue for wet soil, pink and cyan for intermediate conditions.

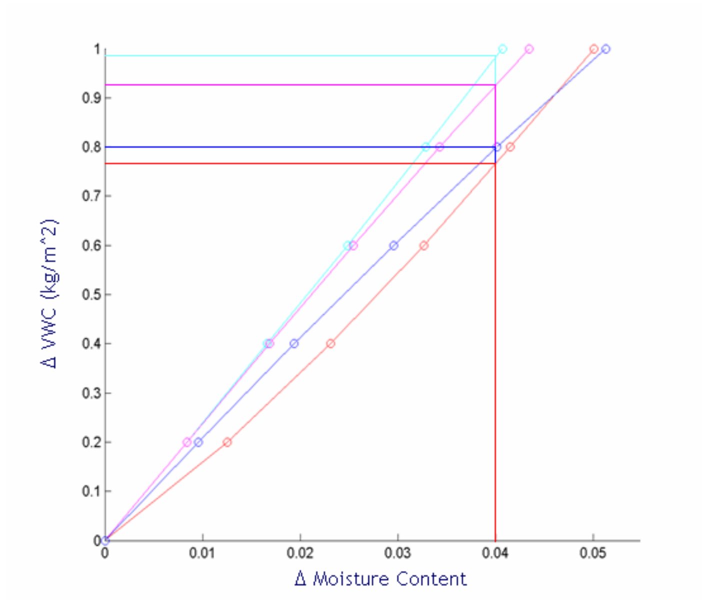

Figure 6.3: Variation in VWC function of variation of soil moisture

6.2 Ground Data

In order to develop relationships between MODIS-based vegetation indices and VWC and to assess the performance of these estimators, ground VWC data collected during NAFE 05 were used. Vegetation types of the High-Resolution areas where samples have been collected, as described in Paragraph 2.3.6, are reported in Figure 6.4.

Vegetation samples have been weighted just after having been collected to measure their wet weight, then they were dried at air temperature (40˚C) in an oven for seven days and then reweighed.

Wet and dry weights of vegetation biomass were used to compute VWC, which can be physically defined as the mass of water per ground unit area (kg/m²).

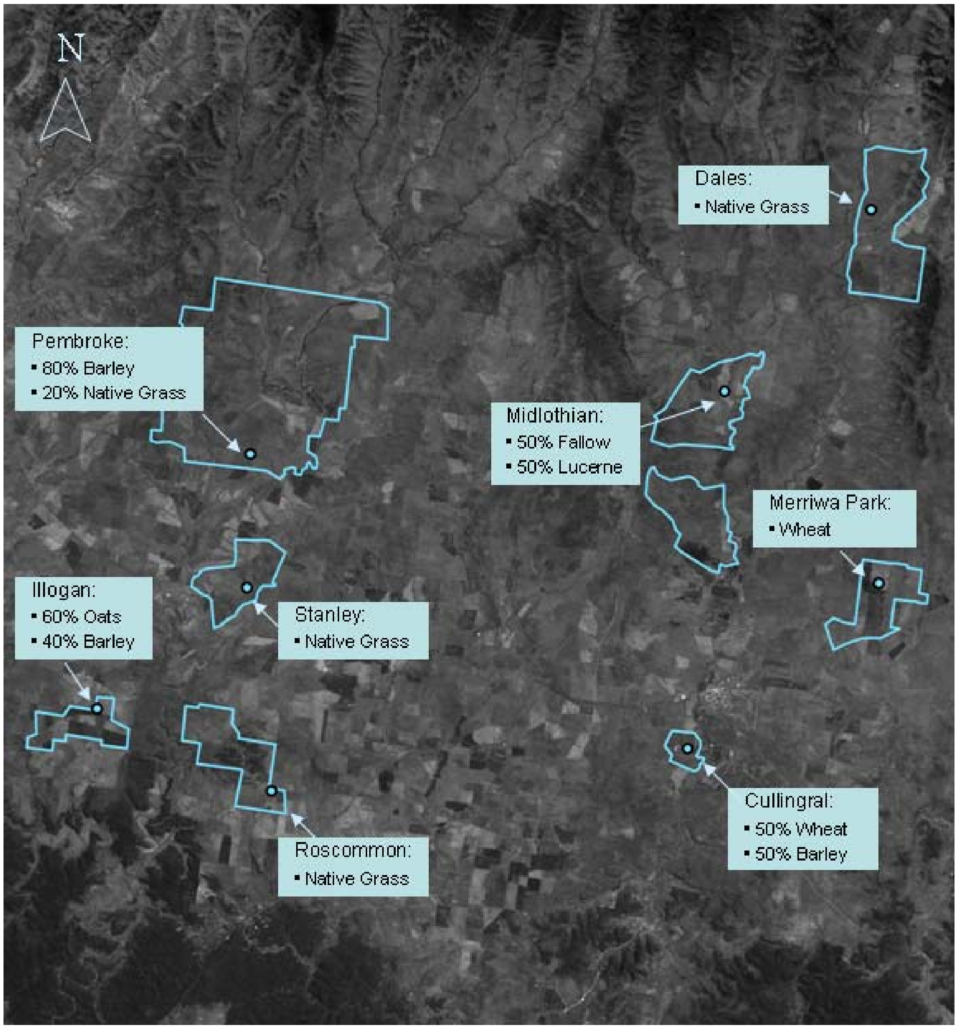

Figure 6.4: Vegetation type at the high-resolution areas

Figure 6.5 illustrates the values of vegetation dry biomass in each farm of the Merriwa Catchment during the four weeks of the field campaign. Plots for the Krui area are shown in Appendix C. The graphs show some statistics of the data collected: the median, the minimum and the maximum values of dry biomass are displayed for each farm and in some cases also the 25^{th}, 75^{th} percentiles and outliers. Dry biomass is almost constant during the whole period of observation and it is very clear how its values are higher for crop, whose mass is bigger than the one of native grass.

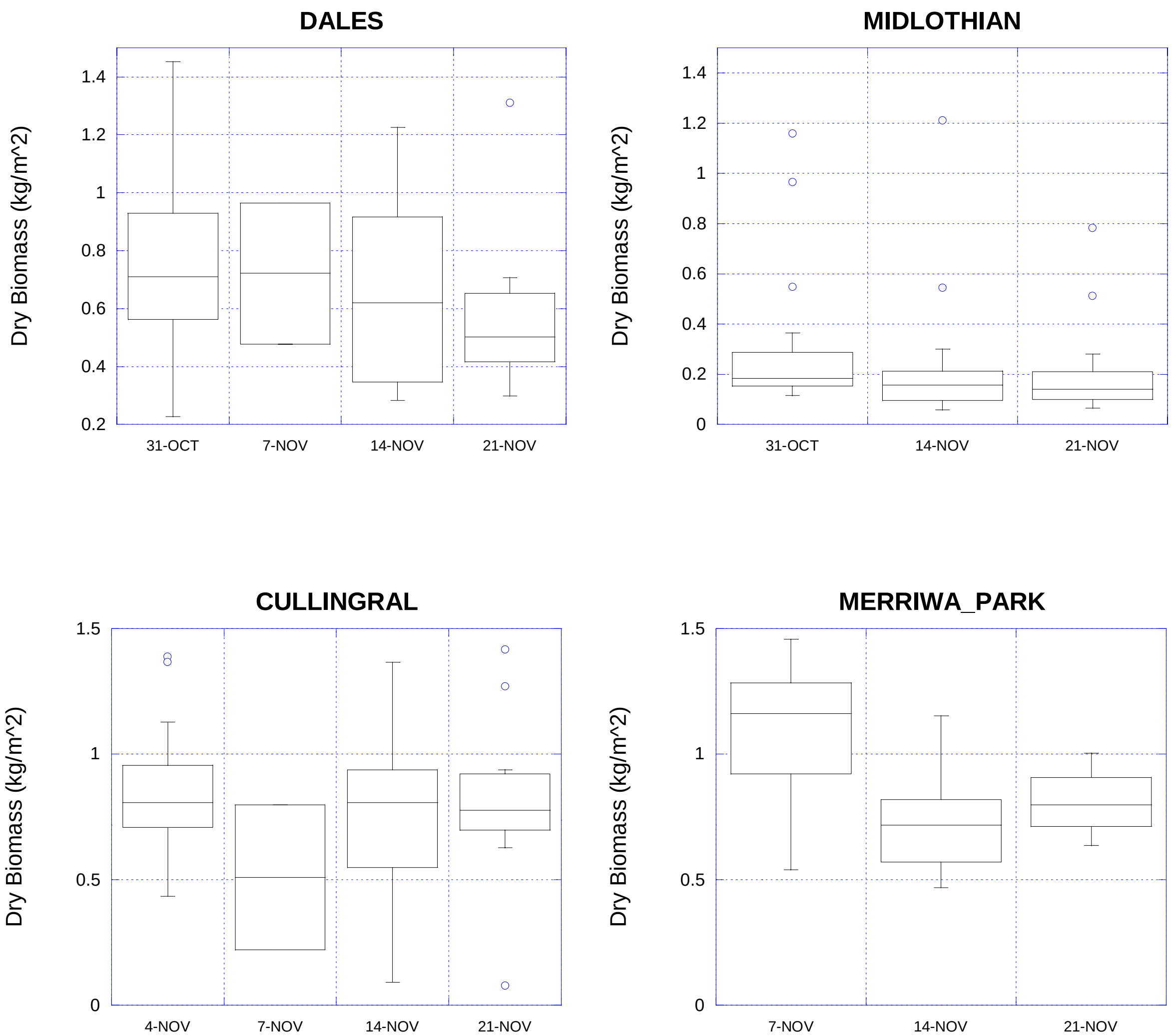

Figure 6.5: Vegetation Dry Biomass (kg/m²) during the month of the field campaign

Figure 6.6 shows the values of vegetation water content, retrieved from ground sampling for the farms of Pembroke, Illogan, Dales and Midlothian; graphs for the others farms are reported in Appendix C. Measured VWC is strongly dependent on vegetation type of each farm. At the Pembroke farm, VWC assumes the highest value due to the tall barley crops present on the area; at the Midlothian farm, instead VWC values are very low, because the crop here was a mix of short Lucerne and fallow. Nevertheless, data confirm that VWC of native grass is lower than VWC of crops. The decreasing of VWC values in time is associated with the rainfall regime of the month, with heavy rainfalls during the first week of campaign followed by a dry period.

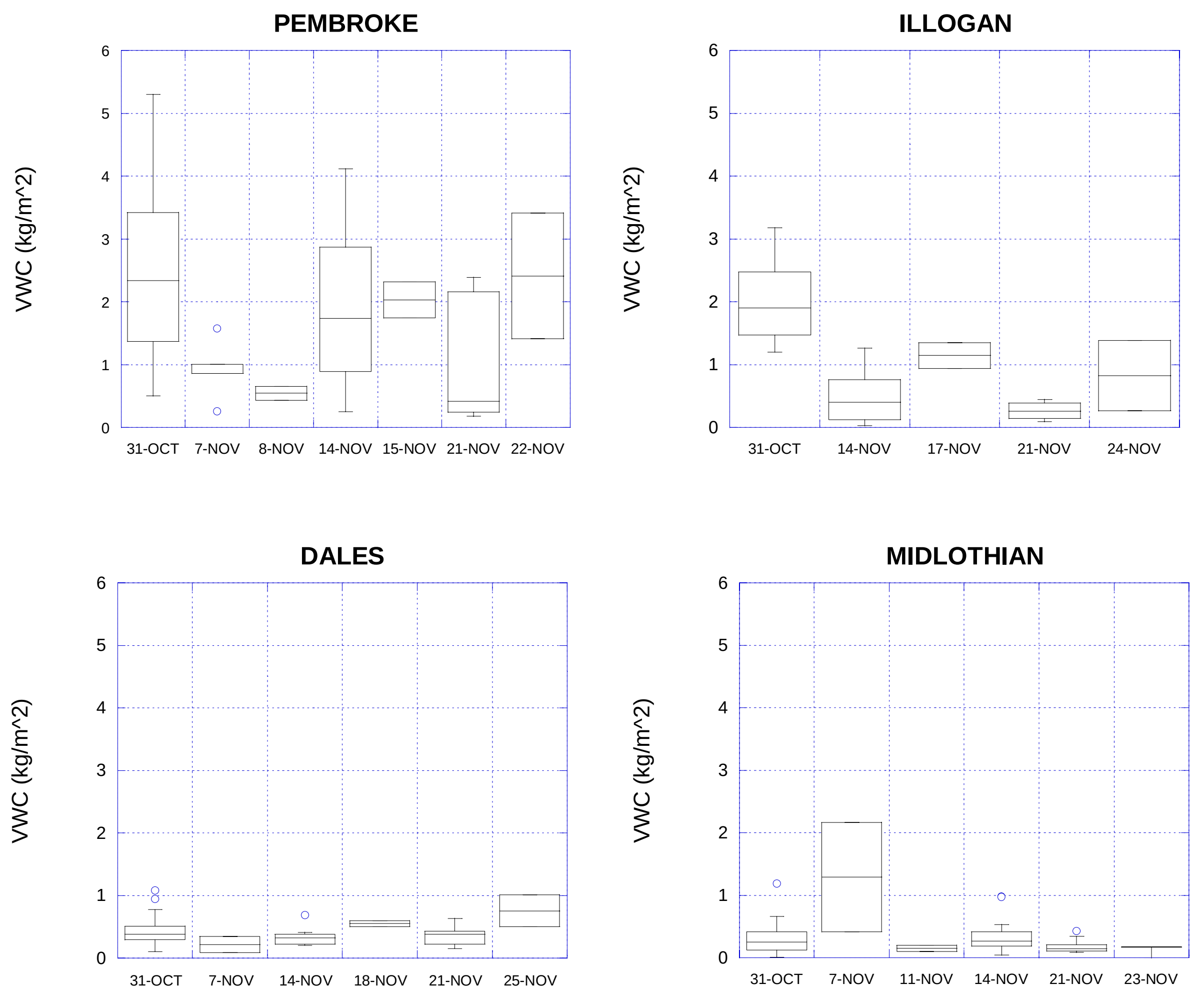

Figure 6.6: Vegetation Water Content (kg/m²) during the month of the field campaign

In addition, measurements of NDVI have been undertaken across the eight farms with a Model 100BX Radiometer, a four-channel instrument (Table 6.1) in the same points where VWC samples have been undertaken.

Table 6.1: Radiometer Channels

100BX Channel Number	Wavelength Range (nm)
A	450-520
B	520-600
C	630-690
D	760-900

To calibrate the instrument, a gauge of the reflectance of a white plate was taken before each measurement of vegetation radiance and to have a more accurate estimate of the NDVI three values of reflectance in RED and NIR bands were collected in each point.

6.3 Satellite Data

Aqua-MODIS Surface Reflectance Products (MYD09GQK) were obtained directly from the NASA DAAC data pool (http://edcdaac.usgs.gov/main.asp).

MODIS product is provided as daily reflectances in two bands (1-2) at 250m spatial resolution and in five bands (3-7) at 500m resolution (Table 6.2). MODIS product also includes Vegetation Indices as NDVI, but with a temporal resolution (16-day) not suitable to our purposes, and therefore was not used in this study. NDVI was calculated from reflectances in red and near-infrared bands.

Table 6.2: MODIS Bands

MODIS Band #	Wavelength Range (nm)
1	620-670
2	841-876
3	459-479
4	545-565
5	1230-1250
6	1628-1652
7	2105-2155

The MODIS Surface Reflectance products are computed to provide an estimate of the surface spectral reflectance for each band as it would be measured at ground level in the absence of atmospheric scattering or absorption. The algorithm generating this product corrects the effect of atmospheric gases, aerosols and thin cirrus clouds.

MODIS data in HDF format downloaded with Sinusoidal Projection have been reprojected to ArcView Raster (bil extension) with Universal Transverse Mercator (UTM) Projection Zone 56S using ENVI 4.0, producing daily reflectance maps of the Goulburn Catchment during the month of the study.

MODIS scenes are not available every day because of cloud coverage, therefore only a cloud-free selection of the available data was used in this study. MODIS scenes for the month of November on the Goulburn Catchment are showed in Figure 6.7.

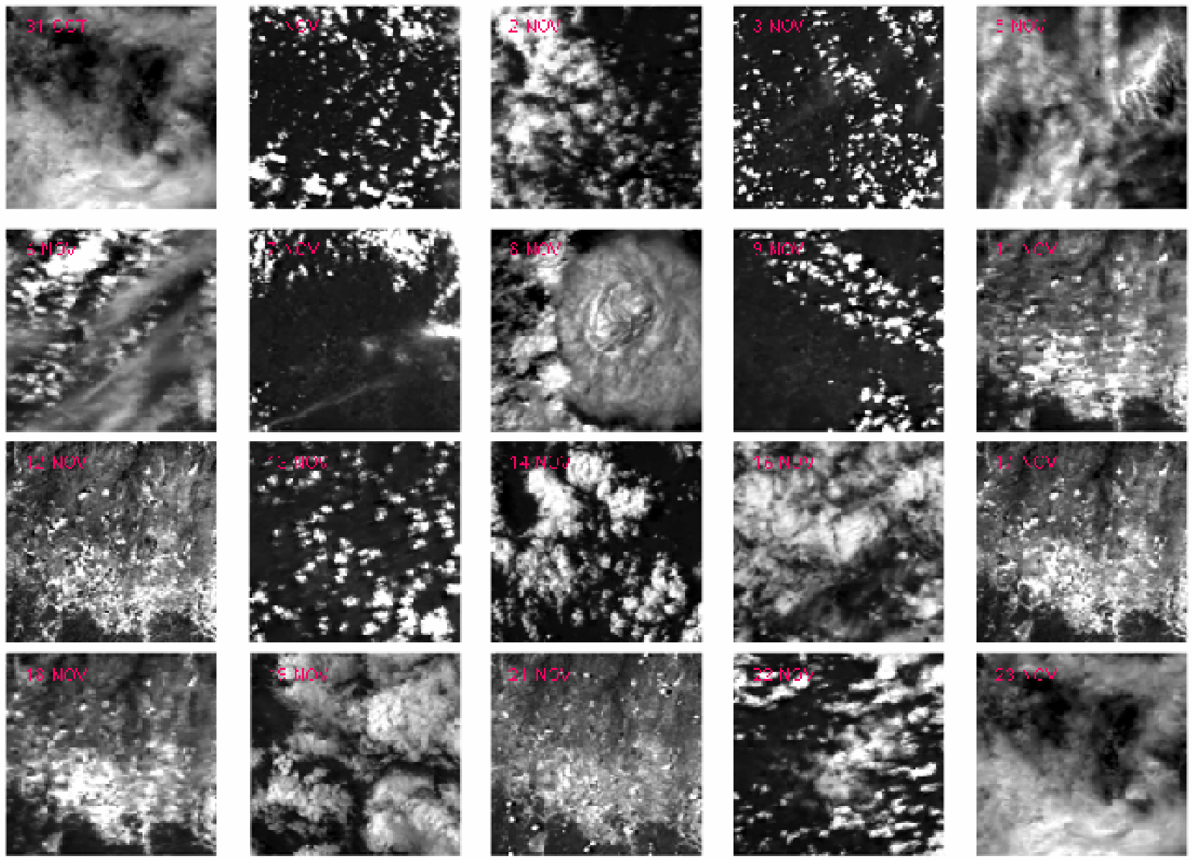

Figure 6.7: MODIS Reflectance in band 1, Goulburn Catchment

6.4 Vegetation Indices

At a first stage, Normalized Difference Vegetation Index was calculated both from MODIS and ground collected reflectance data. The spatial resolution of MODIS (250m) for reflectance in bands 1-2 is quite different from that of the ground radiometers (50m), so a direct comparison of the retrieved NDVI may result incorrect. Therefore ground based NDVI values have been aggregated to give a mean value for the entire high resolution area and only then compared to the MODIS 250m pixel.

As Figure 6.8 shows, there is a strong correlation between ground NDVI and MODIS NDVI, calculated in the same date in which the ground measurements were undertaken.

In the plot, different colors distinguish crop fields (red symbols) from native ones (blue symbols). Most median values of the ground-based NDVI for the both vegetation types are very close to the equivalent MODIS value; this gives confidence in using ground-based NDVI as representative of MODIS NDVI product in the following analysis.

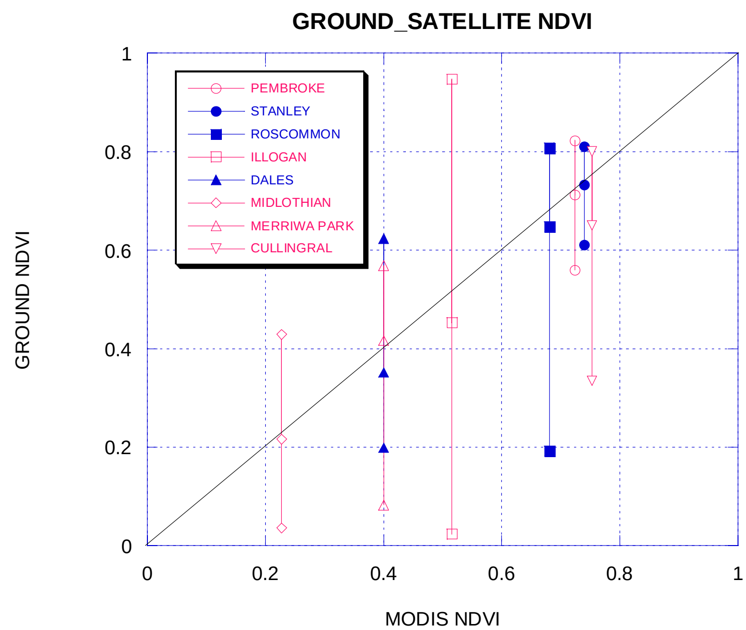

Figure 6.8: MODIS NDVI versus ground-measured NDVI

On the line with literature works (*Jackson et al.*, 2003), $NDWI_{1640}$ and $NDWI_{2130}$ have been evaluated from daily MODIS 500m reflectance data in bands 6 and 7 in order to find a relationship between VWC and VI that is representative of a wide range of canopy.

Raw temporal series of the three VIs during the period of the field campaign are shown in Figure 6.9 together with rainfall data collected at the SASMAS stations. The rainfall histogram shows minimum, mean and maximum values of the rain measured across the eight farms. All series present a good correlation with rainfall regime.

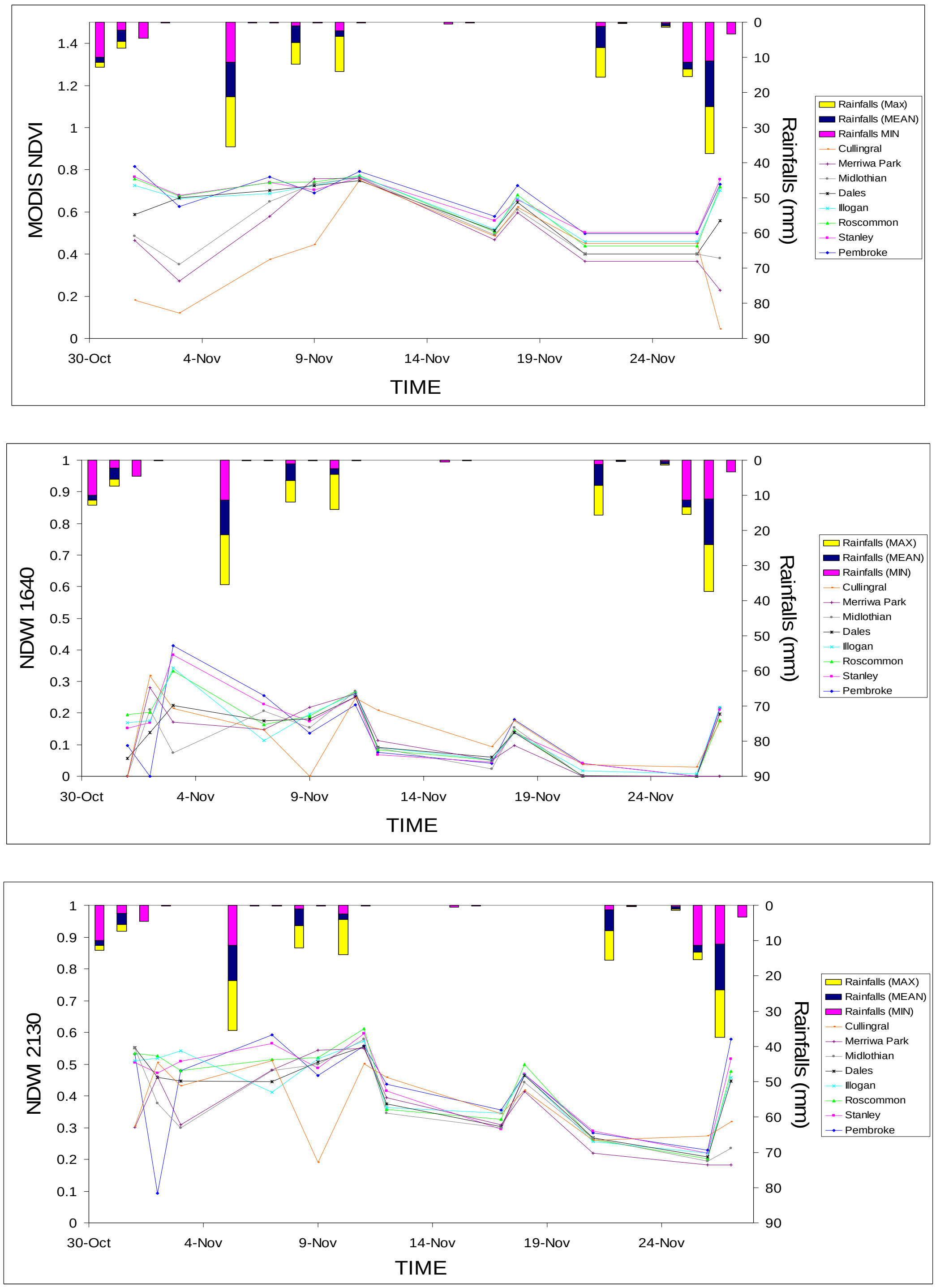

Figure 6.9: MODIS derived Vegetation Indices during the month of November

6.5 VWC estimation using VIs

Relationships between the VIs and VWC were developed by comparing each vegetation index with the ground VWC data in Figure 6.10. Regression curves are shown in these graphs, while correlation coefficient R^2 and Root Mean Square Error (RMSE) are listed in Table 6.3. Land cover is important when using NDVI and NDWI to estimate VWC, because the relationships vary by vegetation type, thus native grass and crop have been distinguished.

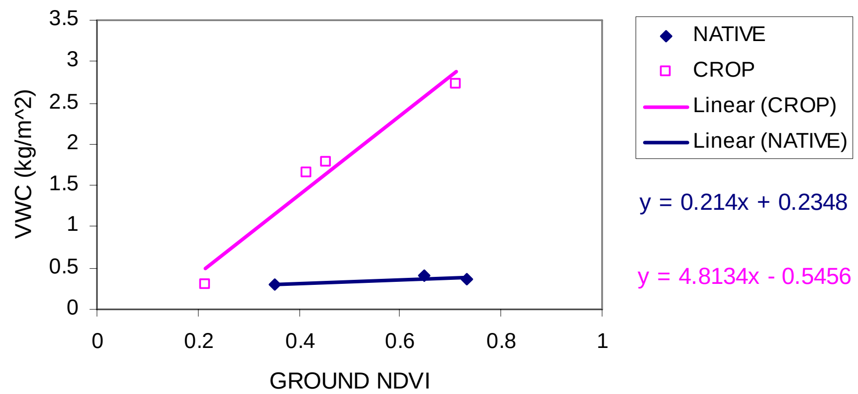

Figure 6.10 (a): VWC as function of ground-measured NDVI

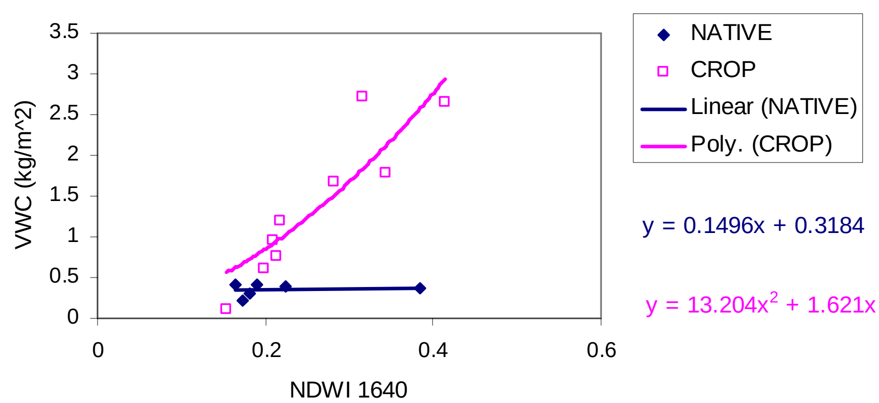

Figure 6.10 (b): VWC as function of MODIS derived $NDWI_{1640}$

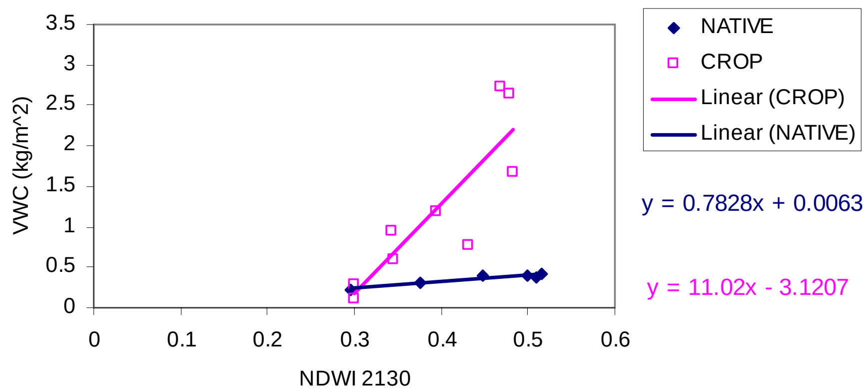

Figure6.10 (c): VWC as function of MODIS derived $NDWI_{2130}$

Table 6.3: Summary of statistics for estimating VWC from VIs

	NDVI		NDWI 1640		NDWI 2130	
	Native Grass	Crop	Native Grass	Crop	Native Grass	Crop
R-squared	0.6998	0.9573	0.0295	0.7931	0.9036	0.7457
RMSE (kg/m²)	0.0228	0.1794	0.0654	0.3861	0.0206	0.4531

The NDVI index shows the highest correlation coefficient R^2=0.9573 and the smallest RMSE=0.1794kg/m² for crop, however because of the saturation of NDVI at high VWC, $NDWI_{1640}$ was considered a better choice and its function was regarded as the best fit curve to estimate crop VWC (R^2=0.7931, RMSE=0.3861kg/m²). As for native grass, $NDWI_{2130}$ shows the best R^2=0.9036 and the lowest RMSE=0.0206kg/m².

6.6 Vegetation type

To estimate VWC all over the Goulburn Catchment a map of the land use was required to distinguish areas with crop from that with native grass.

A land cover classification was performed using a supervised procedure. Information about vegetation type was collected during the field campaign at different locations in the whole area (Fig. 6.11). These observations were used as representative areas (Region of Interest) for each class of the thematic map to be plotted as output. The classification was processed by satellite imaginery processing software ENVI.

A Maximum Likelihood Classification has been applied to a Landsat satellite image of the catchment. This kind of classification assumes that the statistics for each class in each band are normally distributed and calculates the probability that a given pixel belongs to a specific class. No threshold probability was selected, so all pixels have been assigned to the class that had the highest probability.

Fig. 6.12 shows the vegetation coverage classification produced for the whole Catchment of interest. The resulting classes include:

- Urban;
- Crop;
- Native Grass;
- Forest; and
- Open Woodland.

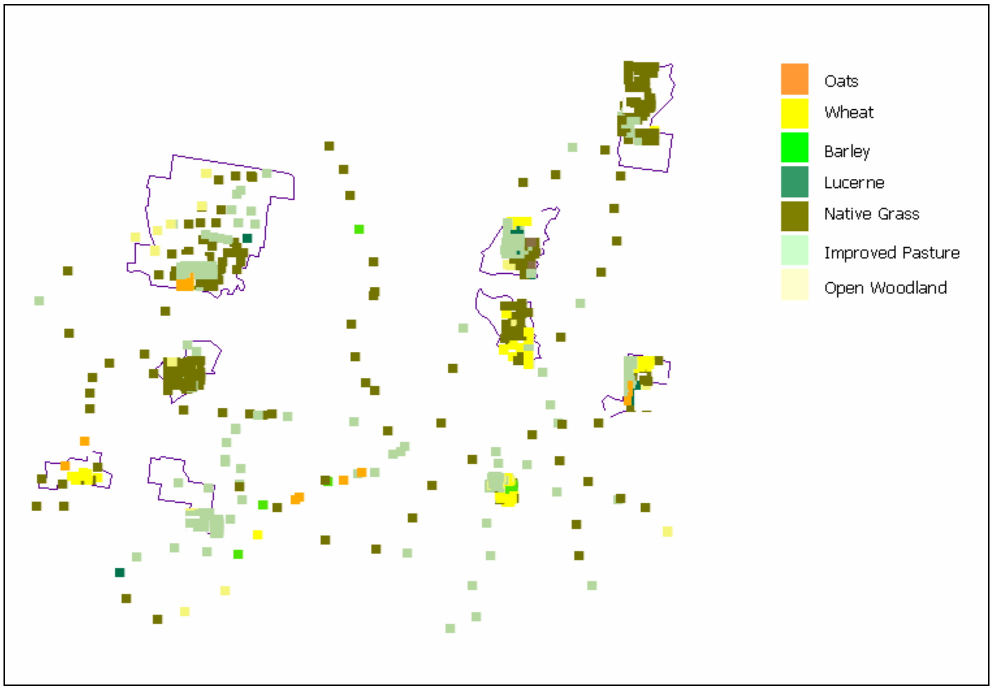

Figure 6.11: Vegetation type, ground information

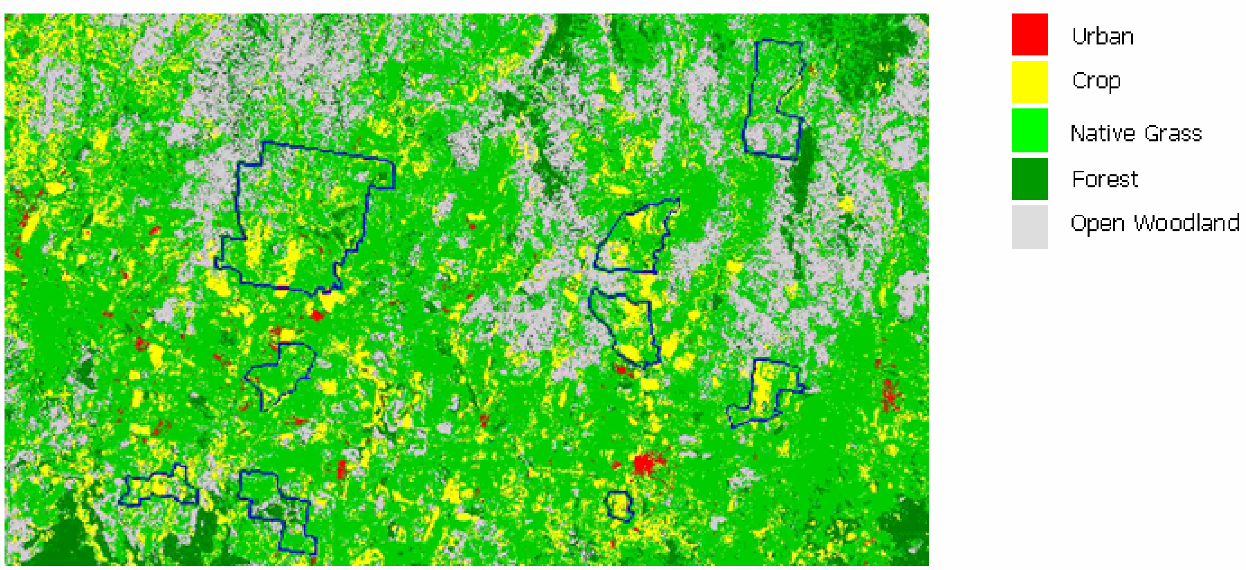

Figure 6.12: Classification of Land Cover across the Goulburn Catchment

6.7 VWC estimates

Using daily MODIS reflectance data and the land cover classification, VWC has been estimated at 500m spatial resolution across the catchment for cloud-free days, applying the two functions illustrated in paragraph 6.4 for crop and native grass.

Figure 6.13 shows examples of maps of vegetation water content estimates for four days during the field campaign. Obviously, in those areas where the land cover is different from crop or native grass, no value of vegetation water content could have been evaluated and a blank pixel has been drawn in the map.

The decreasing of vegetation moisture in time, closely connected with rainfall regime and discussed in the analysis of ground-based data collected in the areas of interest, can be here observed for the whole catchment.

Moreover, these maps show a significant difference between values of VWC for crops and for native grass. At the Illogan, Merriwa Park and Pembroke farms the areas that come out wetter than the others correspond to oats, wheat and barley crops. Areas with native grass present instead lower values of vegetation water content. This difference is more remarkable in the first map (Fig.6.13 (a)) for November 7, when the all vegetation was quite wet, however it can be observed also in the following days.

These results are very encouraging because the estimates of vegetation water content retrieved from vegetation indices based on satellite data are consistent with ground measurements; actually, they present similar patterns, both temporal and spatial.

These estimates of VWC will be the input, together with brightness temperature and soil temperature for the model showed in Chapter 3 and processed in the next chapter to calculate values of soil moisture across the area of interest.

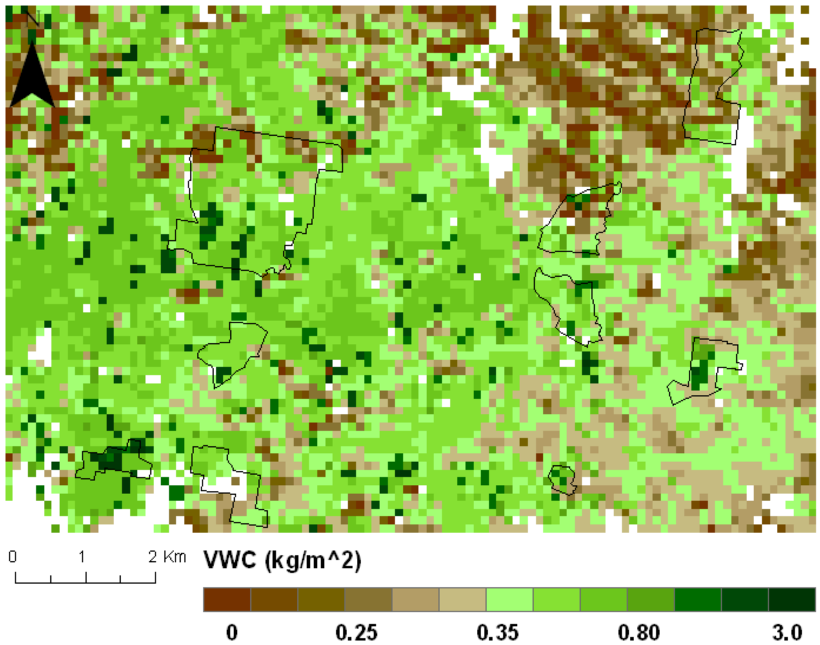

Figure 6.13 (a): VWC estimation, November 7

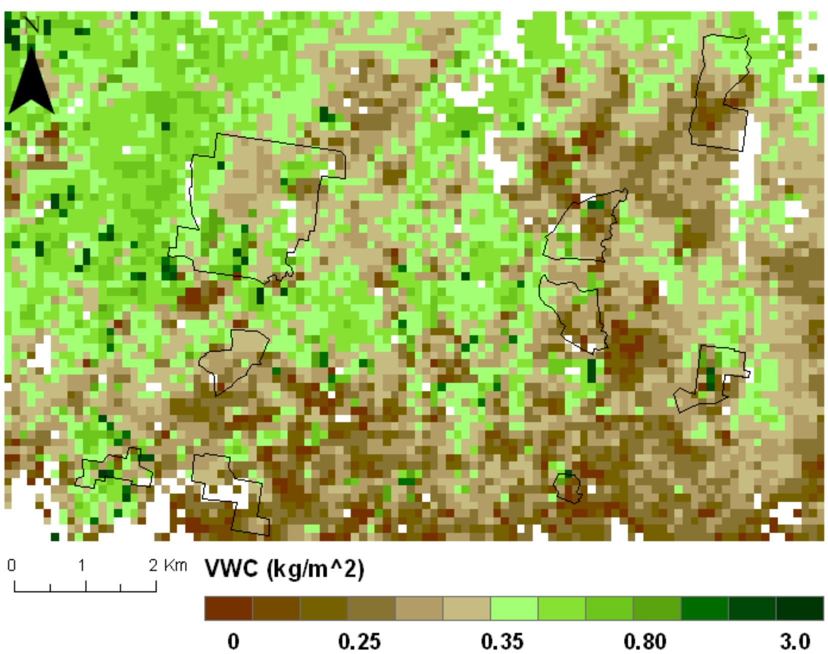

Figure 6.13 (b): VWC estimation, November 12

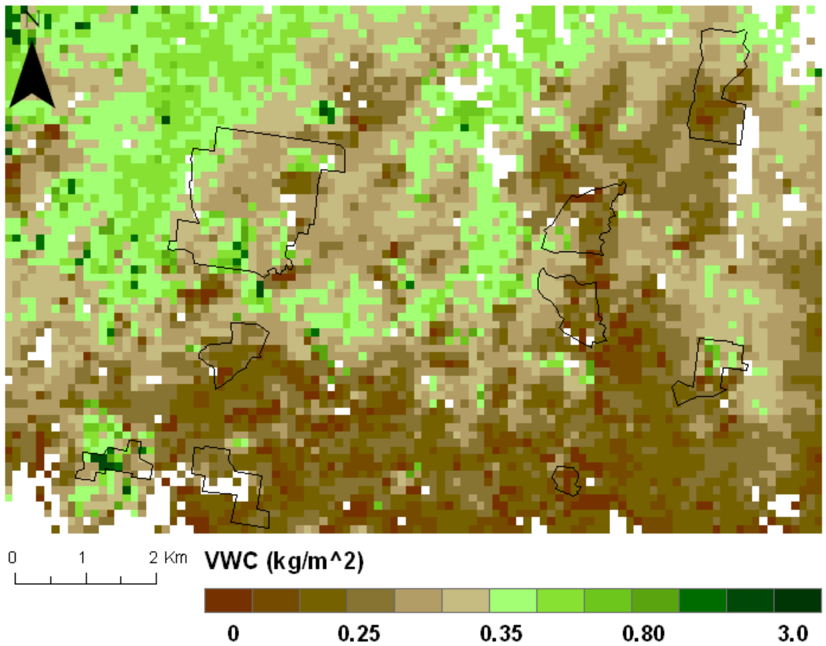

Figure 6.13 (c): VWC estimation, November 17

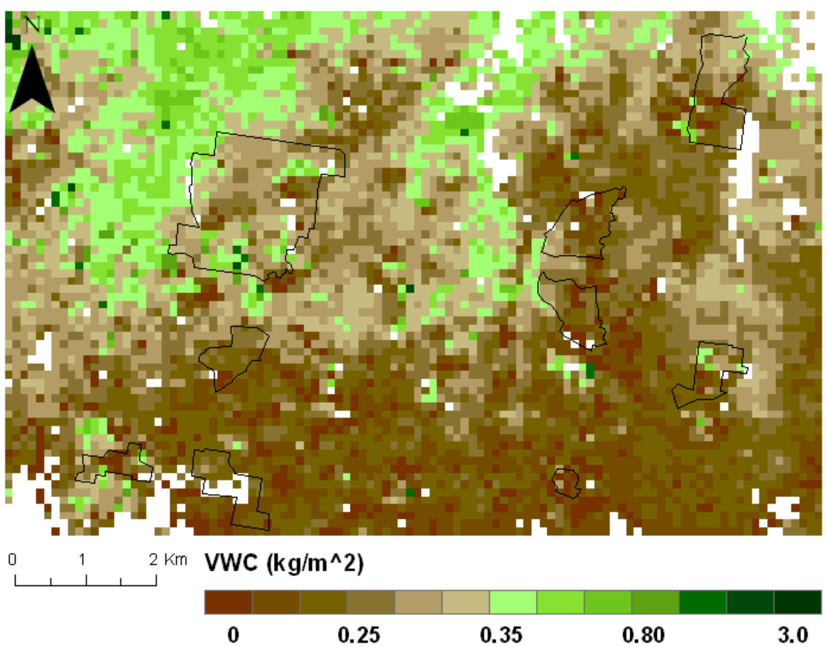

Figure 6.13 (d): VWC estimation, November 21

7

SOIL MOISTURE ESTIMATION

The model described in Chapter 3 was used to retrieve soil moisture states making use of the brightness temperature observations, soil temperature and vegetation water content estimates obtained from airborne, ground and satellite data, as described in Chapters 4, 5 and 6.

The model performance was evaluated by comparison with ground-based measurements of soil water content. Given the complexity of the NAFE'05 ground datasets, in this chapter we will present only the results obtained over the Midlothian farm in the Merriwa area and we will focus on two spatial resolutions, 250m and 500m.

The analysis of the error in the model predictions was done considering both its temporal variability during the month of the NAFE'05 field campaign and its spatial variability across the farm.

Moreover a sensitivity analysis of the model have been performed for the parameter of roughness and the *b* parameter, used for the estimation of the vegetation opacity.

7.1 The area of interest

The Midlothian study area is en extensive farm of approximately 40km^2 in area, situated in the northern half of the Goulburn catchment.

The topography is characterized by a flat alluvial area adjacent to the Merriwa River running north-south in the eastern part of the area, while gently rolling to steep hills characterize its western part. These form a north-south orientated ridge that runs along the entire farm (Fig. 7.1). The property is split into two part, of approximately the same dimension and similar topography, denominated hereby as Midlothian North and Midlothian South.

The landuse in both areas is mostly grazing and cropping (Fig. 7.1(a)). Crops are dominant in the alluvial areas adjacent to the river and are also present on the gentle hills in the southern part. Wheat, Sorghum and Lucerne are the crops present in the area. The rest of the farm is at grazing, with native grass being the predominant land cover with patches of open woodland dominating the steep areas.

Soils are mainly clays, with black earth in the alluvial area and red clays on the ridges.

This area was chosen for different reasons:

- the vegetation cover (crop and native grass) allows to make use of the relationships between Vegetation Indices and vegetation water content developed in Chapter 6 to retrieve the latter over the whole farm area;
- it has a complete dataset at different resolutions for both aircraft and ground-based observations;
- the area is flat or gently rolling (Fig. 7.1(b)), so analysis of the topography effect on the soil moisture retrieval can be done;
- the area is reasonably wide, yet suitable for a spatial analysis;
- the soil type is homogeneous across the all farm (Fig. 7.1(d)).

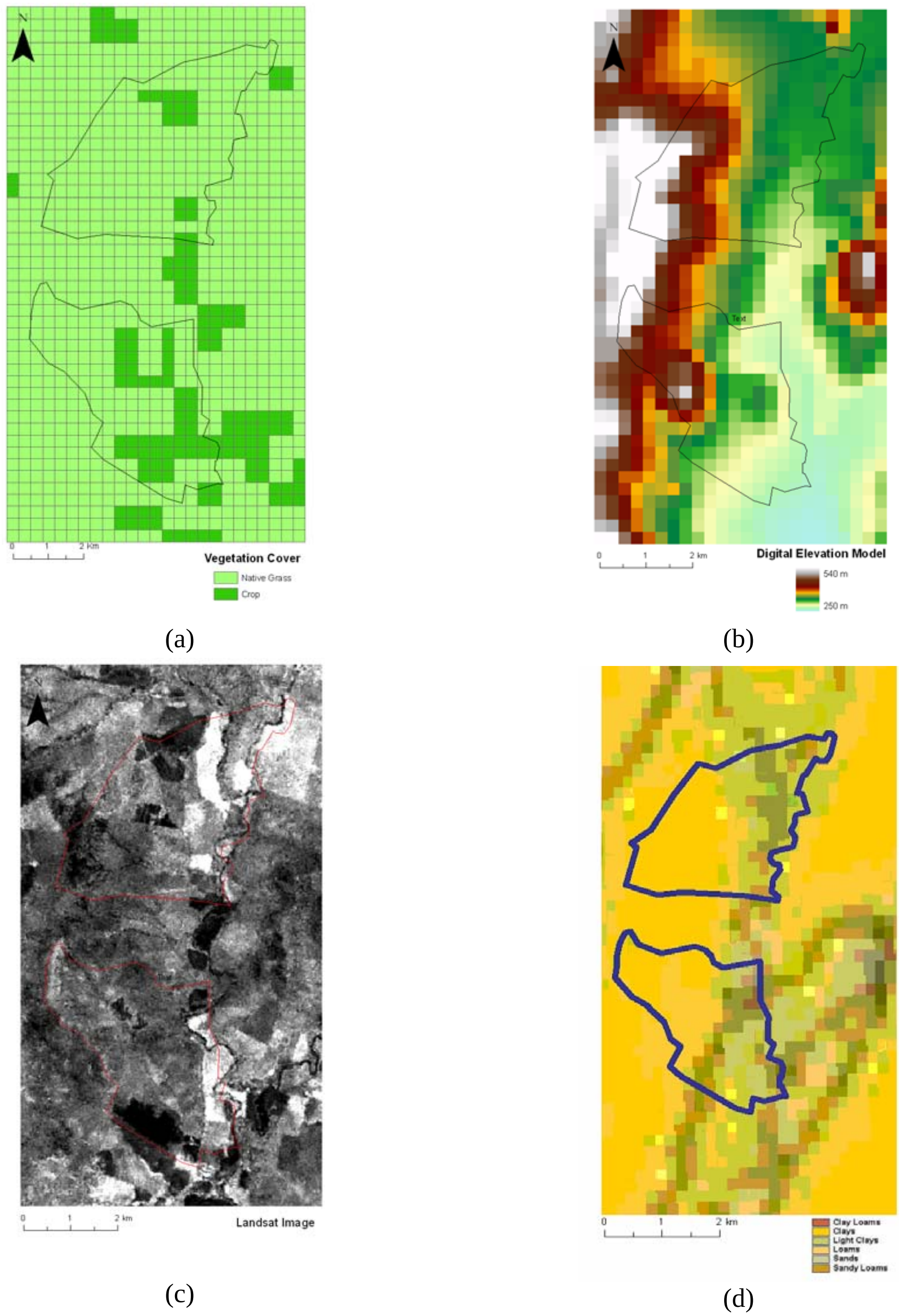

Figure 7.1: The Midlothian farm: vegetation coverage (a), topography (b), Landsat image (c), soil type (d)

7.2 Model input data

In the previous chapters, the three main input variable of the soil moisture retrieval model were obtained by different means for the whole area of interest. This section describes the pre-processing of the data to make them suitable to be fed into the algorithm.

The algorithm processes input data in the form of matrices, where each matrix element correspond to the value of the input variable in a location in space. These matrices correspond to raster representations of the variable spatial distribution. As the three input data came from different processes, some pre-processing was necessary to make the rasters homogeneous. The brightness temperature, vegetation water content and soil temperature data needed therefore to be georeferenced in the same coordinate system (Universal Transverse Mercator, UTM) and scaled to the same spatial resolution.

Two regular grids covering all the area of interest were created with the GIS software ArcMap as reference grids for all the input data. These grids divide the area of interest into square cells of respectively 250m and 500m size. Each cell of the reference grids was then assigned a value of brightness temperature, soil temperature and vegetation water content by spatial comparison with the relevant raster, using different methods of data aggregation and disaggregation. These spatial analysis spoil the precision of the model estimates, but they are necessary to implement a multi-sensor approach for soil moisture retrieval.

7.2.1 Brightness temperature

The data of brightness temperature collected from the aircraft are spatially referenced in they raw form, due to the presence of a GPS receiver on the aircraft.. The information for each observation includes latitude and longitude in Geographic Coordinate System (Geocentric Datum of Australia 1994), a brightness temperature value and the beam ID. This last data is required to the algorithm for the incident angle correction. The different angle of view of each beam of the radiometer allows covering the Midlothian farm with two swaths (Appendix D).

The result is a discrete distribution of brightness temperature values that covers most of the farm area: each point is considered representative of an area whose dimension depends on the altitude of the aircraft. For example from 5000ft and 2500ft the radiometer has a nominal ground resolution of respectively 500m and 250m.Only H polarized brightness temperature data have been used, since they are proved to be more useful in soil moisture retrieval.

After projection into the UTM Coordinate System, a value of brightness temperature for each cell of the reference grid was calculated by averaging all the points falling into each cell. The rough data measured by the airborne radiometer and their aggregation are illustrated in Figure 7.2.

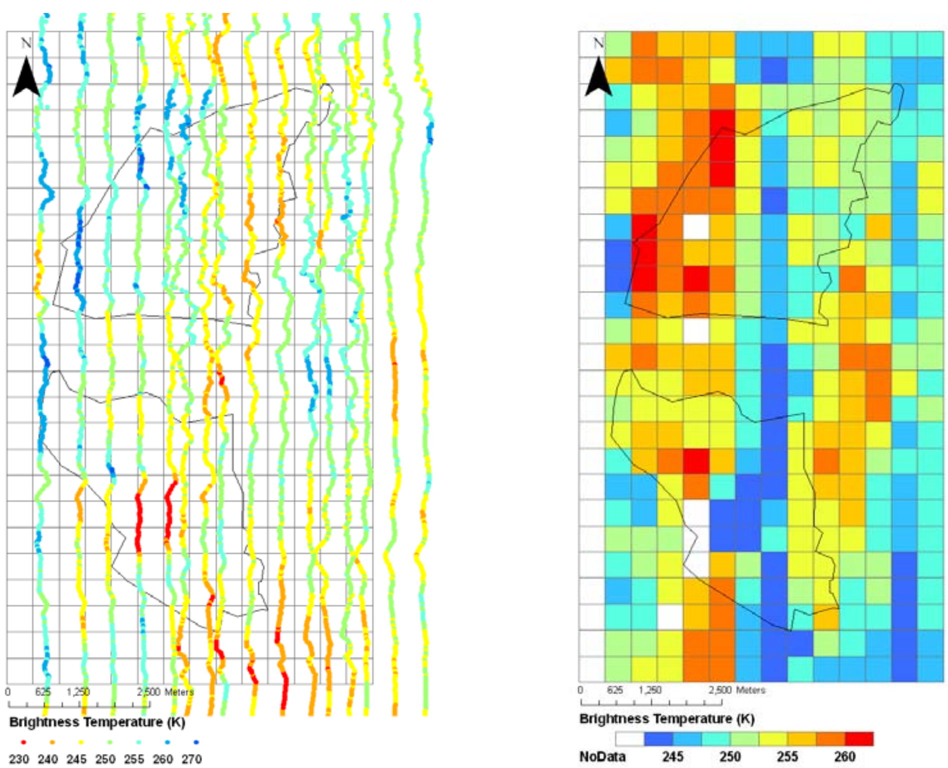

Figure 7.2: Brightness Temperature data aggregation

7.2.2 Soil temperature data

Chapter 5 described the process used to produce maps of the spatial distribution of soil temperature, georeferencing the images obtained by the thermal imager mounted on the aircraft.

The map produced with thermal data acquired at 5000ft altitude has a ground resolution of about 10m, which is much higher than that required for the purpose of the study. This data was then aggregated to the reference grid with the same method described for the brightness temperatures Some cells resulted empty because of lack of observations were left as "no data" areas. An example of the result is showed in the plot below (Fig.7.3).

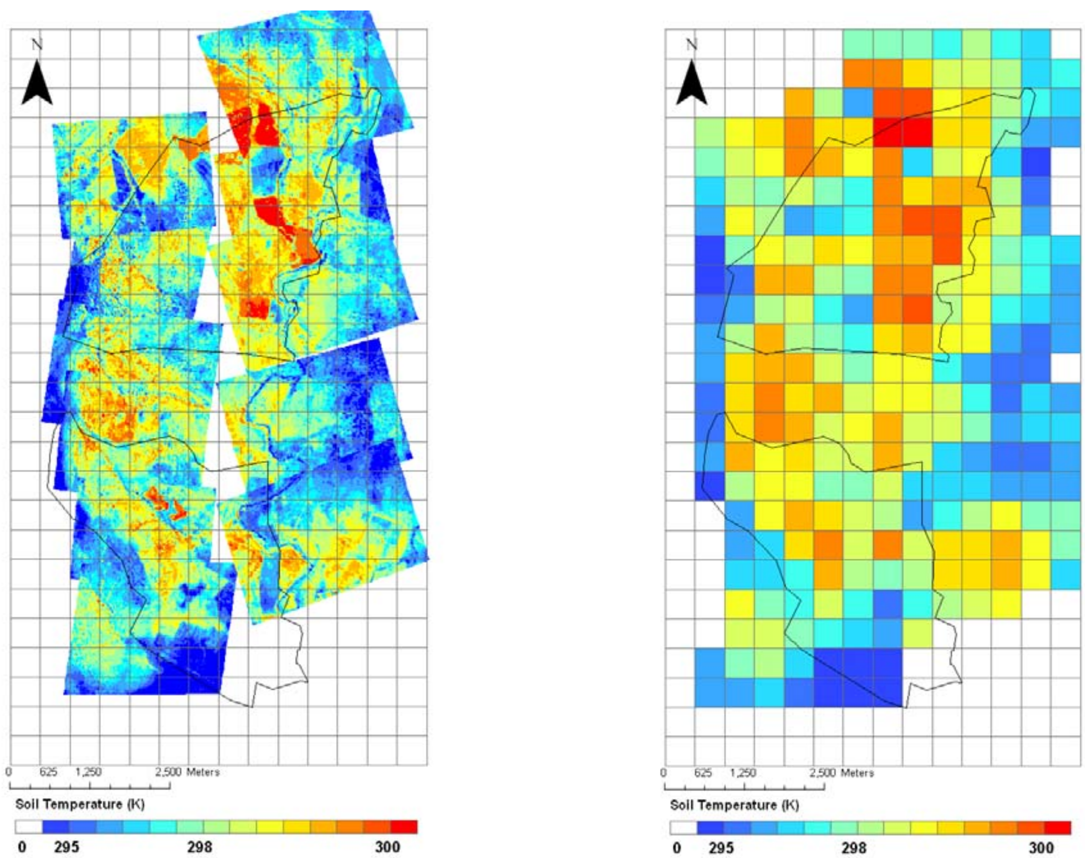

Figure 7.3: Soil Temperature data aggregation

7.2.3 Vegetation water content

The spatial distribution of vegetation water content has been estimated from vegetation indices based on MODIS reflectance data, whose resolution is 500m. To fit these data to the reference grid, the raster of VWC was converted to point data, which were then averaged up to the reference grid with the same method followed for the brightness temperature and the soil temperature. To downscale these data to the 250m, a raster with 250m resolution was interpolated from the point data using an inverse distance weighting interpolation technique. For vegetation water content there are no pixel with missing value, as Figure 7.4 shows, because MODIS satellite covers the whole area of interest.

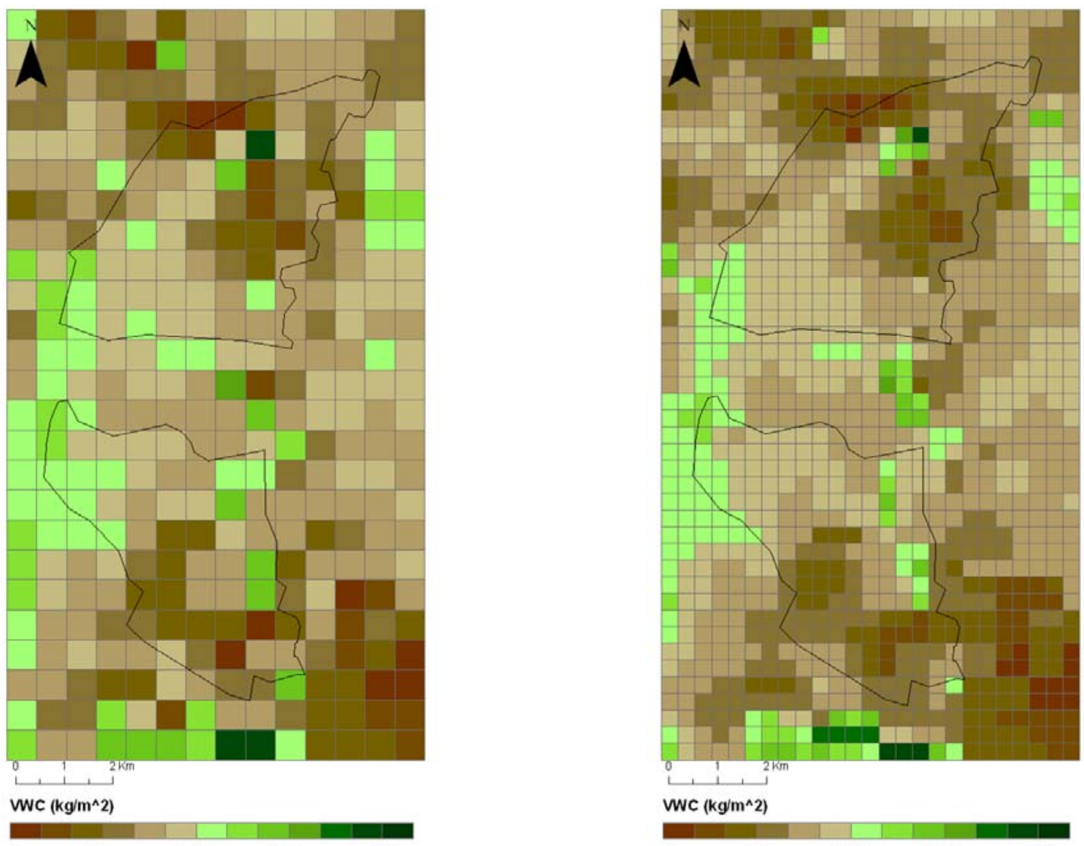

Figure 7.4: Vegetation Water Content data aggregation

7.2.4 Other parameters

Several other parameters are required in order to run the soil moisture retrieval algorithm:

- Roughness
- b parameter
- Soil textural properties

The roughness parameter *h*, which takes into account for the effect of surface roughness on the soil surface emissivity was set equal to 0.29 farm, as calculated from ground measurements (see Table 3.2).

The parameter *b* for the estimation of the vegetation optical depth depends on the vegetation cover and sensor wavelengths. *Jackson* (1993) estimated values of *b* for different vegetation types and sensor wavelength (see Fig. 3.4). In this study, a value of 0.24 was chosen. This value is adequate to the vegetation type in the area of interest.

The parameters defining the soil textural properties, necessary to calculate the transition moisture content θ_T (see Paragraph 2.2), were chosen on the base of laboratory particle analysis of the soil samples collected during the field campaign across the Midlothian farm: 69% clay content, 10% sand content and 50% porosity.

7.3 Ground soil moisture dataset

The farm of Midlothian is divided in two parts: North and South. A large number of ground soil moisture observations were collected in the North part at 250m, 125m and 62.5m scales, while the South was covered with a lower resolution (500m). The dataset includes approximatively 250 ground observations for four days, once a week during the month of November 2005. This observation has been upscaled to the polygon of reference with the same method described in paragraph 7.2 for airborne observations.

Opposite to airborne detection, for ground-based measurements the information of soil moisture is punctual. Therefore, where there was more than one observation in the cell of the reference grid, those values were averaged up; otherwise if only a measurement was available, it was upscaled and taken as representative of an area of 250m^2 or 500m^2, depending on the resolution chosen. Such approximation is necessary to perform the analysis at different scales but can bring to uncertainties in the ground datatset.

Reliability on the ground-based measurement of soil moisture taken with the Stevens Water hydra probe is guaranteed by laboratory calibration of the probes against soil samples of known water content collected in the field.

The data cover the whole range of soil moisture conditions, from very wet at the beginning, to very dry at the end of the sampling month. This is consistent with the rainfall regime, occurred mainly at the beginning of November, followed by a dry period. Figure 7.5 shows mean values of soil moisture collected across the farm and their standard deviations, the histogram of rainfalls measured by the pluviometer located in Midlothian and the soil moisture captured at the permanent SAMSAS station. In the first two weeks soil water content reaches values up to 50%, while in the second half of the sampling period it achieves values lower than 8%.

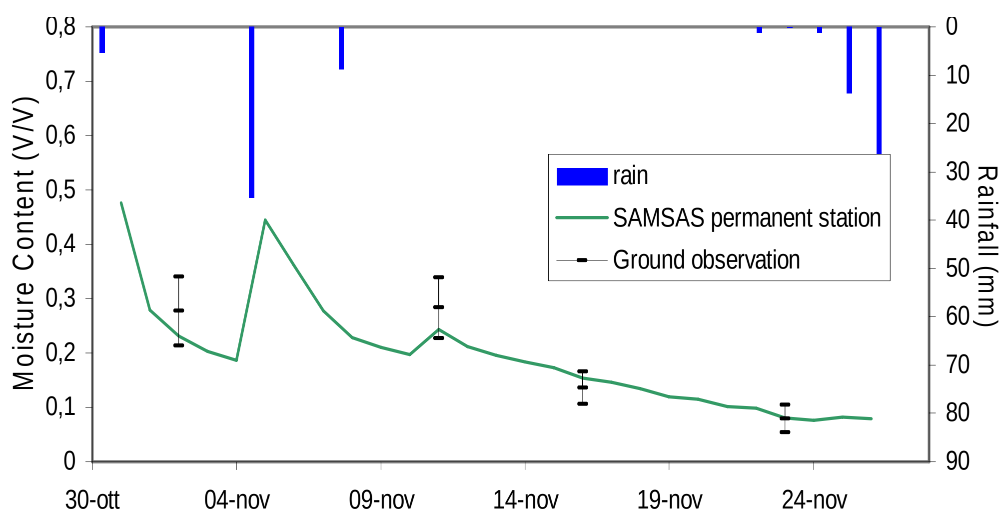

Figure 7.5: Ground soil moisture mean values and rainfalls regime

7.4 Model performance

The performance of the model was studied by comparison between the soil moisture predicted by the model and ground data collected during the NAFE campaign.

The absolute error was calculated in each pixel where both ground observation and soil moisture retrieved by the algorithm were available. Ground sampling was performed at the Midlothian farm once a week during the month of the field campaign, so only in these days it was possible to validate the outputs of the model.

Mean absolute error (MAE) and error variance are summarized for each of the four days and for both the resolutions in Table 7.1. A satisfactory error in soil moisture estimation is considered 4% of soil moisture, because this is the proposed goal for the future SMOS mission. This aim has been definitely reached on November 23, when at the two resolutions the MAE is about 3%. In all the other cases the MAE is lower than 9%. The mean absolute error over the complete dataset is 5.7% for the 250m resolution and 6.8% for the 500m resolution. The error variance shows that the dispersion of the data from the average value is quite low in all the cases analyzed.

Table 7.1: Mean Absolute Error and variance of the error

	MAE (%)		**Error Variance σ_ε (%)**	
	250m	500m	250m	500m
2-nov	5.9	6.3	0.6	0.6
11-nov	5.1	6.6	0.4	0.6
16-nov	7.9	9.3	0.6	0.5
23-nov	3.1	2.7	0.2	0.0
MEAN	5.7	6.8		

7.4.1 Correlation observed-predicted

Figure 7.6 and 7.7 illustrates all the observed and predicted soil moisture values for respectively 250m and 500m resolution. The lines plotted delimit areas where the error is below 10% and 5%.

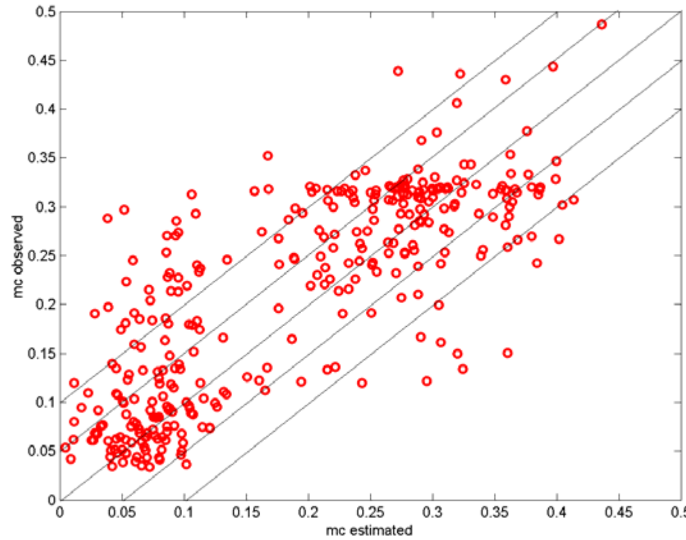

Figure 7.6: Correlation between observed and predicted soil moisture at 250m resolution

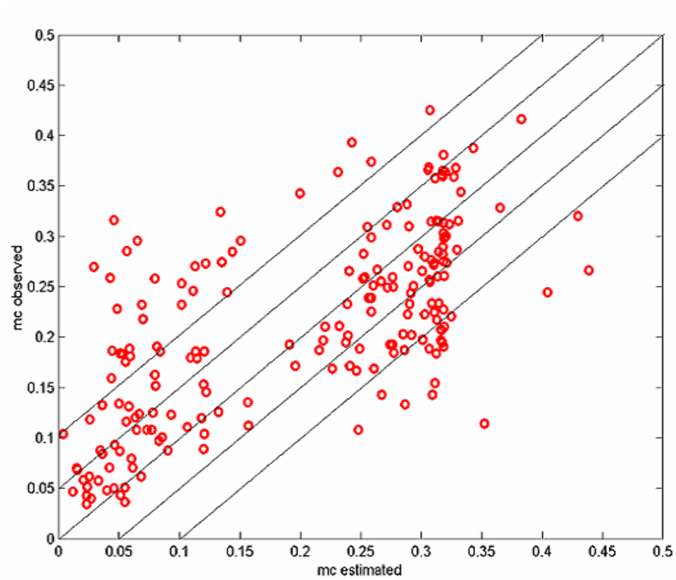

Figure 7.7: Correlation between observed and predicted soil moisture at 500m resolution

Table 7.2 shows the number of occurrences of values under 4% and 10% of error for all the predicted points.

Table 7.2: Occurrences with error lower than 4% and 10%

	Total observations		**Occurrences error<4%**		**Occurrences error<10%**	
	250m	500m	250m	500m	250m	500m
2-nov	83	59	40%	42%	84%	80%
11-nov	95	62	52%	37%	86%	73%
16-nov	89	56	37%	27%	64%	57%
23-nov	62	20	68%	80%	97%	100%
Total	329	197	48%	40%	82%	73%

7.4.2 Error Analysis

In this section the behavior of the error, intended as predicted value minus observed one, will be evaluated trough box plots. The red lines represent the median of the error, the blue ones the first and the third quartiles, the black lines are for maximum and minimum.

Figures 7.8 and 7.9 show that the model does not make any systematic overestimation or underestimation for three days out of four for both the resolutions analyzed. Only on November 16, there is a clear trend to underestimate the value of soil moisture.

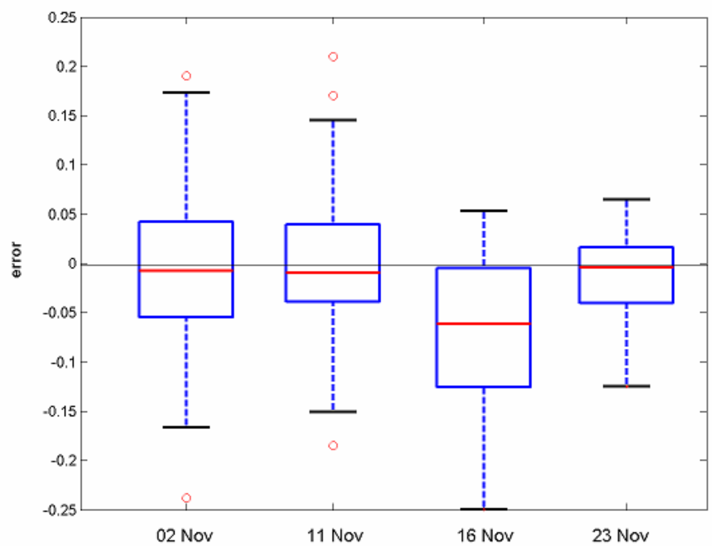

Figure 7.8: Error between predicted and observed values of soil moisture for 250m resolution points

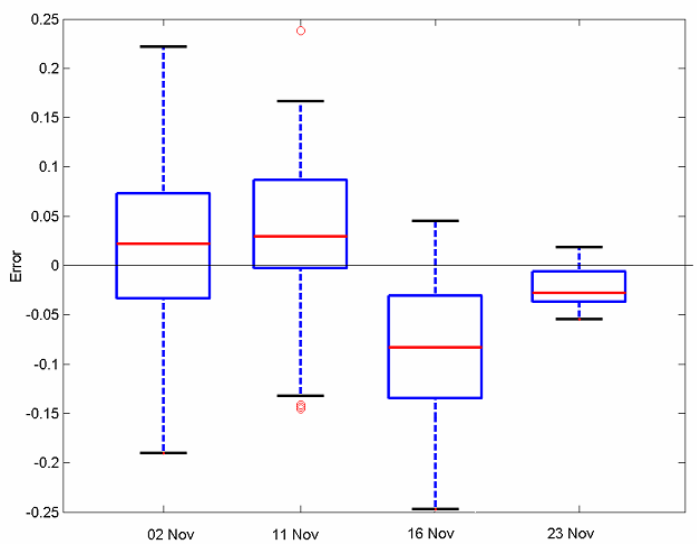

Figure 7.9: Error between predicted and observed values of soil moisture for 500m resolution points

7.5 Temporal and Spatial Analysis

Besides the global statistics, the results of the study show that the trend of the soil moisture variation during the month of the campaign was well predicted by the model. The whole range of conditions for soil moisture has been successfully retrieved from the first week, when the soil water content was closed to saturation, to the last week when soil moisture was almost zero across the all farm.

Several patterns of both temporal and spatial variability on soil moisture can be identified with an accurate analysis of the maps that illustrate the results of the study in Appendix A.

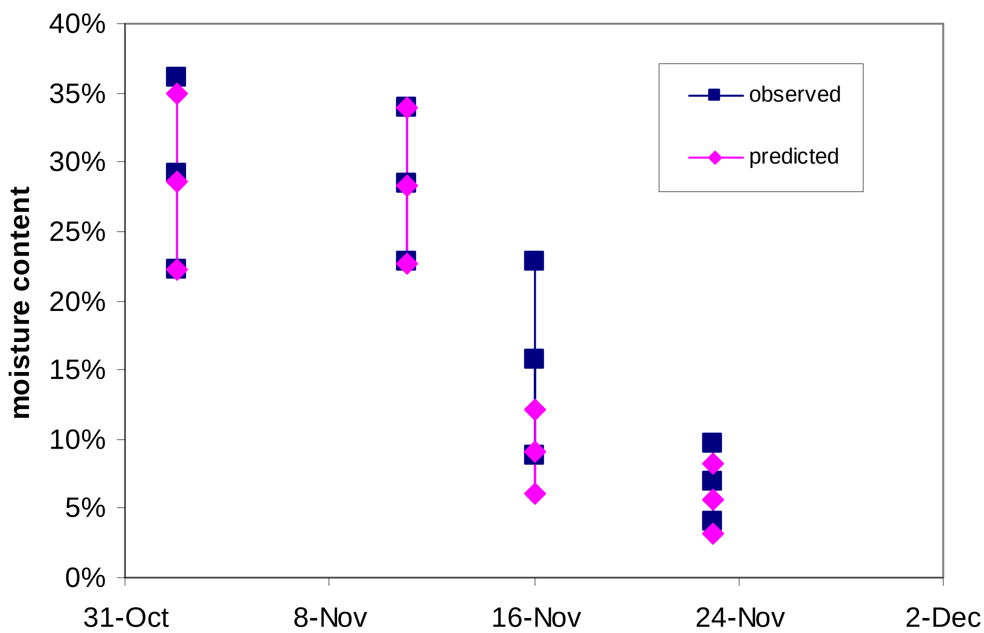

Figure 7.10 Moisture observed and predicted with standard deviation interval.

7.5.1 Sub-Grid Variability

November 16 is the most critical day for the soil moisture estimation. In particular Figure 7.8 shows how in this day the model under-estimates significantly the moisture content. This fact can be explained a priori in two ways.

The general moisture trend in the Goulburn Catchment as across the Midlothian farm can be roughly said to be decreasing. Both observed and estimated moisture agree that the average moisture over the area is about 30% in the first half of the month of November, to decrease to 15% on November 16 and to 7% on November 23.

This means that on November 16 the soil is experiencing a drying process, which is known to have inhomogeneous behaviour.

The soil moisture process has two threshold values, which are the saturation upper limit and the wilting point lower limit. After a rain event the soil tends to homogenize its moisture content to the saturation whereas after dry period the soil tend to homogenize its moisture to the wilting point. During transition periods, either a drying process or a wetting process, the soil moisture reaches a marked inhomogeneous spatial distribution, due to different soil behavior and particular conditions in each single patch. In a drying process for instance those patches that are more sun exposed will start drying much sooner and much faster than the patches in the shadow.

The lack of homogeneity can affect mainly the ground soil moisture observations, since in inhomogeneous conditions a punctual measure is not representative of the moisture content within a patch. This is an effect of sub-grid variability and it increases with the pixel dimension. In fact, error values (Table 7.1) at 500m resolution are higher than those estimated at 250m scale for the first three days, when spatial distribution of soil moisture was remarkable. Differently, airborne observations collect average information over areas, and then the low level spatial inhomogeneity is not caught.

An example is shown in Fig 7.11: ground soil moisture data present a weird variability, not confirmed by airborne measurements. This configuration is more remarkable in the southern part of the farm where some cells are particularly wet, opposite to airborne pixels. This can be explained by the ground sampling strategy because Midlothian South was sampled at only 500m scale; this means that the punctual measurements upscaled to the 500m pixel could not be representative of the effective conditions of the soil moisture.

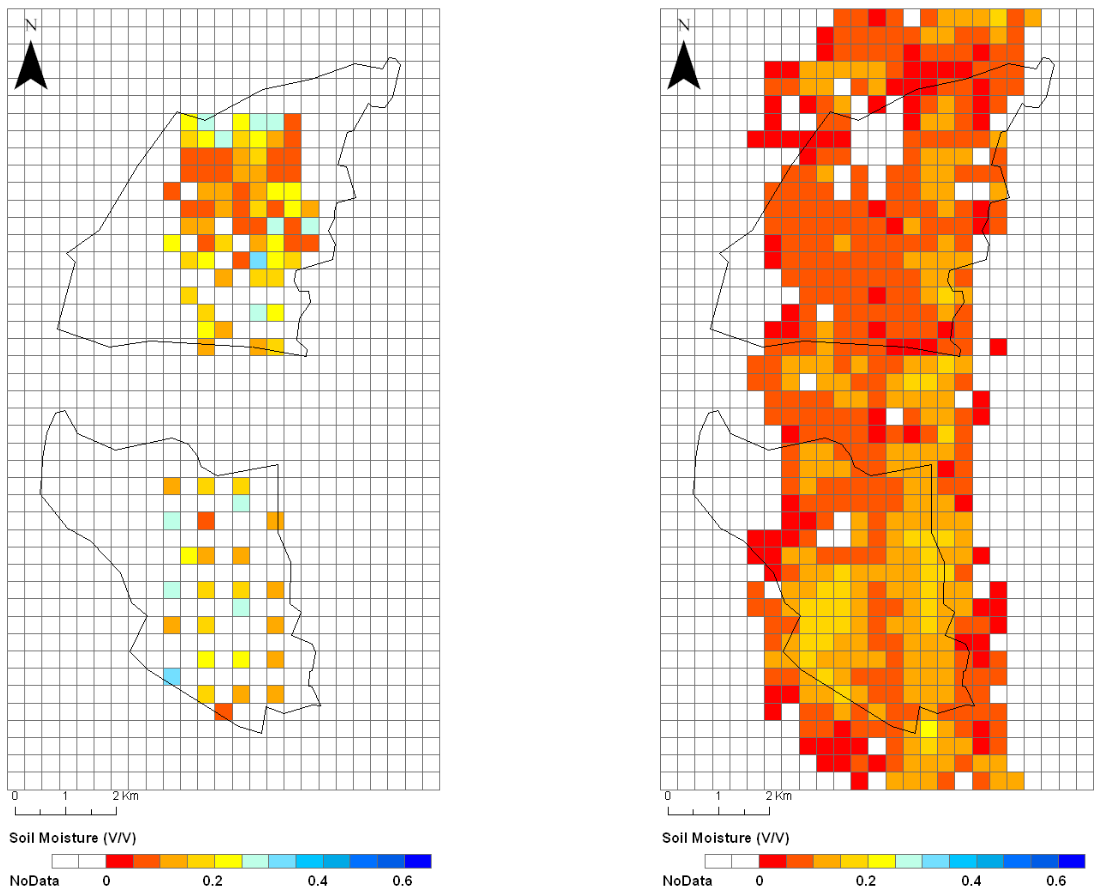

(a) (b)

Figure 7.11: Ground -based (a) and predicted (b) soil moisture on November 16

7.5.2 Topographic effect

The topography of the Midlothian farm is characterized by a flat area in the eastern part of the catchment adjacent to the Merriwa River running north-south and by gently rolling to steep hills in the western part. These form a north-south orientated ridge that runs along the entire farm.

Topography affects the spatial distribution of soil moisture: in the western part soil came out to be drier than in the alluvional area because of the surface runoff. This behavior is well described by the maps of retrieved soil moisture as well as by ground observations for the first three weeks (see Appendix A). On November 23 the soil is dry all over the area, so the topographic effect can not be noticed. Figure 7.12 shows an example of how this topographic effect is well predicted by the algorithm. In the south-western part a wetter area can be identified: this is due to its location at the bottom of the steep hills.

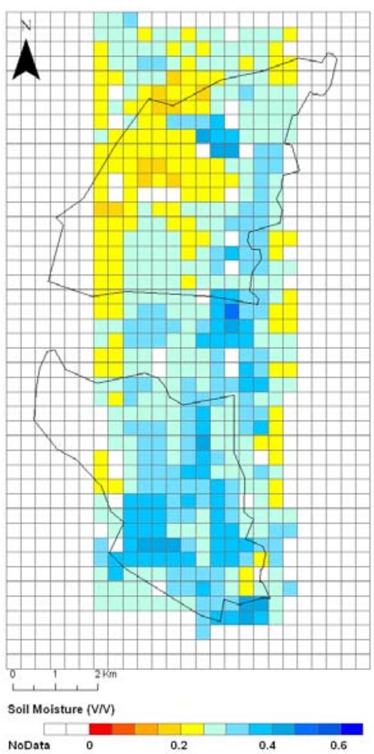

(a)

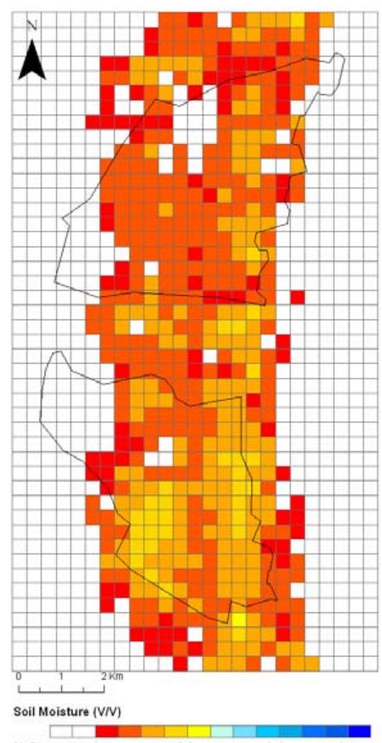

(b)

Figure 7.12: Soil moisture retrieved by the model on November 2 (a) and November 11 (b)

7.6 Sensitivity analysis

Among the input variables of the soil moisture retrieval model brightness temperature, soil temperature and vegetation water content have been widely investigated. The other parameters have been assumed constant, with typical values found in literature or average values measured during the field campaign.

7.5.3 Soil roughness

As already described the roughness parameter has been kept constant at 0.29 over the whole Midlothian farm, as estimated during the field campaign. Nevertheless the ground measure of roughness is a hard issue and uncertainty can be expected. Figure 7.13 analyses what influence a different roughness parameter can have on the daily mean absolute error in soil moisture estimation.

The figure shows that soil roughness has a big weight on soil moisture retrieval. In the case of this study a higher estimate of soil roughness (up to 0.5) could have given slightly better soil moisture estimation for November 16, whereas for the 2nd, 11th and November 23 the ground estimate of soil roughness seems to produce the smallest error in soil moisture retrieval.

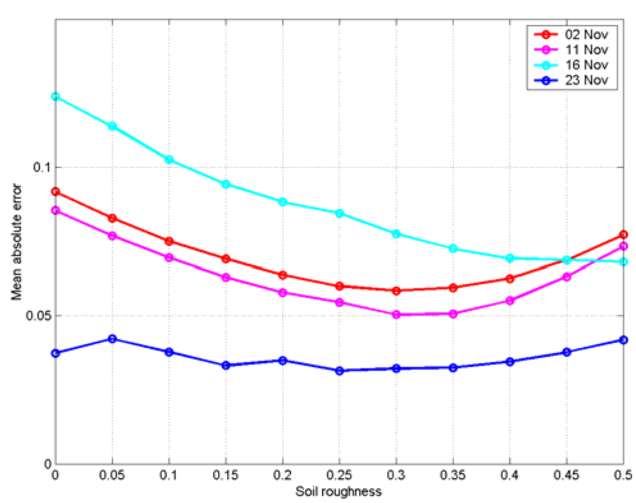

Figure 7.13: Mean absolute error function of the roughness parameter

7.5.4 *b*-parameter

Sensitivity analysis was also performed on the parameter *b* which connect the vegetation water content with the optical depth in the soil moisture retrieval algorithm (see Chapter 3). To run the model, it was set to the value of 0.24. Figure 7.14 shows that the mean absolute error has not considerably variation due to the choice of the value of *b*. This behavior is appreciable on the whole dataset for values of *b* smaller than 0.5, that represents a threshold value for the Midlothian farm. In fact higher values of *b* are only used for areas where the vegetation coverage is dense native grass.

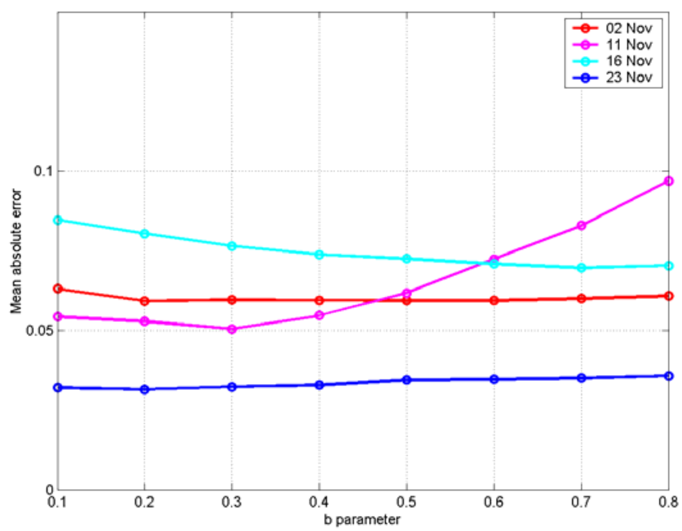

Figure 7.14: Mean absolute error function of *b* parameter

8

CONCLUSIONS

The main issue of this study is the estimation of surface soil moisture with a multi sensor approach.

Data for this purpose were collected during the NAFE 05 field campaign, in November 2005 in Eastern Australia. The Department of Civil & Environmental Engineering of the University of Melbourne was the main organizer of the experiment, with the collaboration of the University of Newcastle and the European Space Agency.

During that time, contributions have been made by the authors of this study towards the planning, execution and analysis of the month-long intensive field campaign.

The scientific objectives and data requirements of NAFE ’05 have been met by coordinating an aircraft remote sensing campaign with a ground data collection campaign. The aircraft remote sensing campaign made use of a small environmental aircraft equipped with passive microwave, infrared and visible sensors to map the whole study area. Ground measurements included near-surface soil moisture for direct validation of the passive microwave remote sensors observations, as well as ancillary data such as vegetation biomass, land cover information, soil temperature and surface roughness.

Remote sensing of soil moisture requires i) calibrated brightness temperature data, ii) information on vegetation water content and iii) information on soil temperature. This study presents results from aircraft and satellite data during the intensive field campaign, addressing these three important issues.

The brightness L-Band temperature was obtained after a calibration assessment, which implied observation of sky, water and blackbody target. Soil temperature of the top 5cm was estimated applying an empirical relationship to soil surface thermal infrared measurements performed by a thermal camera, mounted under the aircraft wing. Vegetation water content was estimated by using vegetation indices based on MODIS satellite reflectance data, for two different vegetation coverage, native grass and crops. Moreover, findings from these three components have been combined to yield a remotely sensed soil moisture estimate with a physically based model and comparisons made with field measured soil moisture.

The Midlothian farm was chosen in the whole area interested by the campaign as pilot site to perform the study, due to its favorable characteristics: the uniform clay soil type, the vegetation coverage mainly of native grass and crop, the wide extension which makes it suitable for spatial analysis, the gently hilly tendency that allows to perform assessment about the effect of topography on soil moisture. Ground and airborne observations on this area were performed once a week during the field campaign. Two spatial resolution, 250m and 500m, have been chosen to perform the analysis.

The results are encouraging and even if a proposed goal of 4% v/v of error was not reached in this preliminary study, the performance of the model was more than satisfactory. Results indicate a very good agreement of the retrieved and measured soil moisture spatial distribution, with an overall absolute retrieval error not higher than 5.7% v/v.

The model does not present any systematic overestimation or underestimation for three days out of four for both the resolutions analyzed. Only on November 16, there is a clear trend to underestimate the value of soil moisture. This can be due to the drying process the soil was experiencing on that day, since this process is known to have inhomogeneous behaviour. The lack of homogeneity can affect mainly the ground soil moisture observations, since in inhomogeneous conditions a punctual measure is not representative of the moisture content within a patch. This is known as sub-grid variability effect and it is one of the mainly causes of error. A ground sampling at higher resolution could correct this kind of effect and better describe the spatial variability.

A spatial analysis has been done comparing topography of the focus area to the spatial distribution of soil moisture: in the hilly area, soil is drier than in the alluvional one because of the surface runoff. This behavior is well described by the model as well as by ground observations.

The temporal trend of the soil moisture variation during the month of the campaign was well predicted by the model, since there is consistency between soil moisture estimated by the algorithm and the rainfall regime.

The whole range of conditions for soil moisture has been successfully retrieved from the first week, when the soil water content was closed to saturation, to the last week when soil moisture was almost zero across the all farm.

The results are encouraging toward the use of PLMR-derived soil moisture for further studies; therefore, more analysis is required.

A first step could be an extension of the procedure here presented to the whole dataset collected during the NAFE 05 campaign, exploring the entire Goulburn Catchment and all the spatial resolutions investigated.

Moreover, the accuracy of the input parameters of the model can be improved by:

- increasing the accuracy in the aggregation process from measured brightness temperature to grid cells.
- improving the relationship to estimate soil temperature including auxiliary data easily available (e.g. air temperature) and analysing the atmospheric effect on the thermal images from the aircraft;
- extending the relationships between vegetation water content and satellite-derived vegetation indices to a more complete range of vegetation types, including bare soil; this requires a landuse classification with more thematic classes;
- using also V polarized brightness temperature, which is known to show better the effects of the vegetation layer.

REFERENCES

Chen D, Huang J., Jackson T. J. 2005. Vegetation water content estimation for corn and soybeans using spectral indices derived from MODIS near- and short-wave infrared bands. *Remote sensing of Environment 98* (225-236).

Choudhury B., Schmugge T. J., Chang A., Newton R. 1979. Effect of surface roughness on the microwave emission from soil. *Journal of Geophysical Research 84* (5699-5706).

Choudhury B., Schmugge T. J., Mo T. 1982. A parameterization of effective soil temperature for microwave emission. *Journal of Geophysical Research 87* (1301-1304).

Coll C., Caselles V., Galve J., Valor E., Niclos R., Sanchez J., Rivas R. 2005. Ground measurements for the validation of land surface temperatures derived from AATSR and MODIS data. *Remote sensing of Environment 97* (288-300).

Crosson W., Limaye A., Laymon C. 2005. Parameter sensitivity of soil moisture retrievals from airborne L-band radiometer measurements in SMEX02. *IEEE Transactions on Geoscience and Remote Sensing 43* (1517-1528).

Dash P., Göttsche F., Olesen F., Fisher H. 2002. Land Surface temperature and emissivity estimation from passive sensor data: theory and practice-current trends. *International Journal of Remote Sensing 23* (2563-2594).

Dash P., Göttsche F., Olesen F., Fisher H. 2005. Separating surface emissivity and temperature using two channel spectral indices and emissivity composites and comparison with a vegetation fraction method. *Remote sensing of Environment 96* (1-17).

Diadong R., Ming X. 2004. 4DVAR assimilation of ground temperature for the estimation of soil moisture and temperature. *16th Conf. Numerical Weather Prediction American Meteorology Society, Seattle, Washington.*

Doraiswamy P., Sinclair T., Hollinger S., Akhmedov B., Stern A., Prueger J. 2005. Application of MODIS derived parameters for regional crop yield assessment. *Remote sensing of Environment 97* (192-202).

Exotic incorporated. 1994. Model 100BX held radiometer: instruction manual. Exotec Incorporated, Gaithersburg, Maryland, USA.

French A., Norman J., Anderson M. 2003. A simple and fast atmospheric correction for spaceborne remote sensing of surface temperature. *Remote sensing of Environment 87* (326-197).

Gallo K., Ji L., Reed B., Eidenshink J., Dwyer J. 2005. Multi-platform comparisons of MODIS and AVHRR normalized difference vegetation index data. *Remote sensing of Environment 99* (221-231).

Gao B. 1996. NDWI-A normalized difference water index for remote sensing of vegetation liquid water from space. *Remote sensing of Environment 58* (257-266).

Goward S., Xue Y., Czajkowski K. 2002. Evaluating land surface moisture conditions from the remotely sensed temperature/vegetation index measurements. An exploration with the simplified simple biosphere model. *Remote sensing of Environment 79* (225-242).

de Rosnay P., Calvet J.-C., Kerr Y., Wigneron J.-P., Lemaître F. Escorihuela M. J., Muñoz Sabater J., Saleh K., Barri J., Bouhours G., Coret L., Cherel G., Dedieu G., Durbe R., Fritz N.E.D., Friossard F., Hoedjes J., Kruszewski A., Lavenu F., Suquia D., Waldteufel P. 2005. A long term field campaign experiment for soil moisture and land surface processes remote sensing . *Remote sensing of Environment,* submitted.

Jackson T., Chen D., Cosh M., Li F., Anderson M., Watlthall C., Doriaswamy P., Hunt E. 2004. Vegetation water content mapping using Landsat data derived normalized difference water index for corn and soybeans. *Remote sensing of Environment, Article in press* (1-8).

Jackson T. J., Le Vine D. 1996. Mapping surface soil moisture using an aircraft-based passive microwave instrument: algorithm and example. *Journal of Hydrology 184* (85-99).

Jackson T. J., Le Vine D., Swift C., Schmugge T. J., Schiebe F. 1995. Large area mapping of soil moisture using the ESTAR passive microwave radiometer in Washita '92. *Remote sensing of Environment 53* (23-37).

Jackson T. J., Schmugge T. J. 1994. Surface soil moisture measurement with microwave radiometry. *Acta Astronautica 35* (477-482).

Jackson T. J., Schmugge T. J. 1991. Vegetation effects on the microwave emission of soils. *Remote sensing of Environment 36* (203-212).

Kang S., Kim S., Oh S., Lee D. 2000. Predicting spatial and temporal patterns of soil temperature based on topography, surface cover and air temperature. *Forest Ecology and Management 136* (173-184).

Keryn I. P., Polglase P. J., Smethurst P. J., O'Connell A. M., Carlyle C. J., Khannaa P. K. 2004. Soil temperature under forests: a simple model for predicting soil temperature under a range of forest types. *Agricultural and Forest Meteorology 121* (167-182).

Klein L., Swift C. 1977. An improved model for the dielectric constant of sea water at microwave frequencies. *IEEE Transactions on Antennas and Propagation 25* (104-111).

Li Z.-L., Becker F., Stoll M. P., Wan Z. 1999. Evaluation of six methods for extracting relative emissivity spectra from thermal infrared images. *Remote sensing of Environment 69* (122-138).

Li F., Jackson T., Kustas W., Schmugge T., French A., Cosh M., Bindlish R. 2004. Deriving land surface temperature from Landsat 5 and 7 during SMEX02/SMACEX. *Remote sensing of Environment 92* (521-534).

Lin J. 1980. On the force-restore method for prediction of ground surface temperature. *Journal of Geophysical Research 85* (3251-3245).

Njoku E., Entekhabi D. 1996. Passive microwave remote sensing of soil moisture. *Journal of Hydrology 184* (101-129).

Ogawa K., Schmugge T, Jacob F., French A. 2002. Estimation of broadband land surface emissivity from spectral thermal infrared remote sensing. *Agronomie 22.*

Owe M., de Jeu R., Walker J. 2001. A methodology for surface soil moisture and vegetation optical depht retrieval using the microwave polarization difference index. *IEEE Transactions on Geoscience and Remote Sensing 39* (1643-1654).

ProSensing System Engineering for Environmental Remote Sensing. Polarametric L-band microwave radiometer (PLMR) Technical Report.2005. ProSensing Inc. Amherst, Massachusetts USA.

Sedano F., Gong P., Ferrão M. 2005. Land cover assessment with MODIS imaginery in southern African Miombo ecosystems. *Remote sensing of Environment 98* (429-441).

Schmugge T. J. 1998. Applications of passive microwave observations of surface soil moisture. *Journal of Hydrology 212* (188-197).

Schneeberger K., Stamm C., Mätzler C., Flühler H. 2004. Ground-based dual-frequency radiometry of bare soil at high temporal resolution. *IEEE Transactions on Geoscience and Remote Sensing 42* (588-595).

Skou N., Hoffman-Bang D. 2005. L-band radiometers measuring salinity from space: atmospheric propagation effects. *IEEE Transactions on Geoscience and Remote Sensing 43* (2210-2217).

Sobrino J. A., Muñoz J. C., Paolini L. 2004. Land surface temperature retrieval from Landsat TM 5. *Remote sensing of Environment 90* (434-440).

Tian Y., Woodcock C., Wang Y., Privette J., Shabanov N., Zhou L., Zhang Y., Buermann W., Dong J., Veikkanen B., Häme T., Andersson K., Ozdogan M., Knyazikhin Y., Myneni R. 2002. Multiscale analysis and validation of the MODIS LAI product I. Uncertainty assessment. *Remote sensing of Environment 83* (414-430).

Timlin D., Pachepsky Y., Acock B., Sǐmunek J., Flerchinger, Whisler F. 2002. Error analysis of soil temperature simulations using measured and estimated hourly weather data with 2DSOIL. *Agricoltural Systems 72* (215-239).

Ulaby F., Moore R., Fung T. 1986. Microwave remote sensing: active and passive, vol I and III, Artech House, Dedham, MA.

Van Niel, McVicar T., Fang H., Liang S. 2003. Calculating environmental moisture for per-field discrimination of rice crops. *International Journal of Remote Sensing 24* (885-890).

Van Niel, McVicar T. 2004. Current and potential uses of optical remote sensing in rice-based irrigation systems: a review. *Australian Journal of Agricultural Research 55* (155-185).

Verhoef A., Fernández-Gálvez J., Diaz-Espejo A., Main B., El-Bishti M. 2005. The diurnal course of soil moisture as measured by various dielectric sensors: effect of soil temperature and the implications for evaporation estimates. *Journal of Hydrology, Article in press* (1-16).

Xiao J., Moody A. 2005. A comparison of methods for estimating fractional green vegetation cover within a desert-to-upland transition zone in central New Mexico, USA. *Remote sensing of Environment 98* (237-250).

Yu Y., Privette J.L., Pinheiro A.C. 2005. Analysis of the NPOESS VIIRS land surface temperature algorithm using MODIS data. *IEEE Transactions on Geoscience and Remote Sensing 43* (2340-2349).

Walker J. 2000. Estimating soil moisture profile dynamics from near-surface soil moisture measurements and standard meteorological data. *PhD Thesis, University of Newcastle, Australia.*

Walker J., Panciera R. 2005. National Airborne Field Experiment 2005: Experiment Plan.

Wigneron J.-P., Calvet J.-C., de Rosnay P., Kerr Y., Waldteufel P., Saleh K., Escorihuela M.J., Kruszewski A. 2004. Soil moisture retrievals from biangular L-band passive microwave observations. *IEEE Transactions on Geoscience and Remote Sensing 1* (277-281).

Wigneron J.-P., Calvet J.-C., Pellarin T., Van de Griend A., Berger M., Ferrazzoli P. 2003. Retrieving near-surface soil moisture from microwave radiometric observations: current status and future plans. *Remote sensing of Environment 85* (489-506).

Zarco-Tejeada P., Rueda C., Ustin S. 2003. Water Content estimation in vegetation with MODIS reflectance data and model inversion methods. *Remote sensing of Environment 85* (109-124).

APPENDIX A

SUMMARY OF THE MAPS

Appendix A shows maps of the three inputs of the soil moisture retrieval model, brightness temperature, soil temperature and vegetation water content, for the whole period of NAFE 2005 field campaign across the Midlothian farm at both the resolutions explored (250m and 500m).

Maps of ground measured soil moisture and soil moisture retrieved by the algorithm are illustrated together with maps of the absolute error, calculated as absolute value of the difference between observed and predicted soil moisture.

Results are presented for four days during the month of November, specifically on those days in which ground measurements were available.

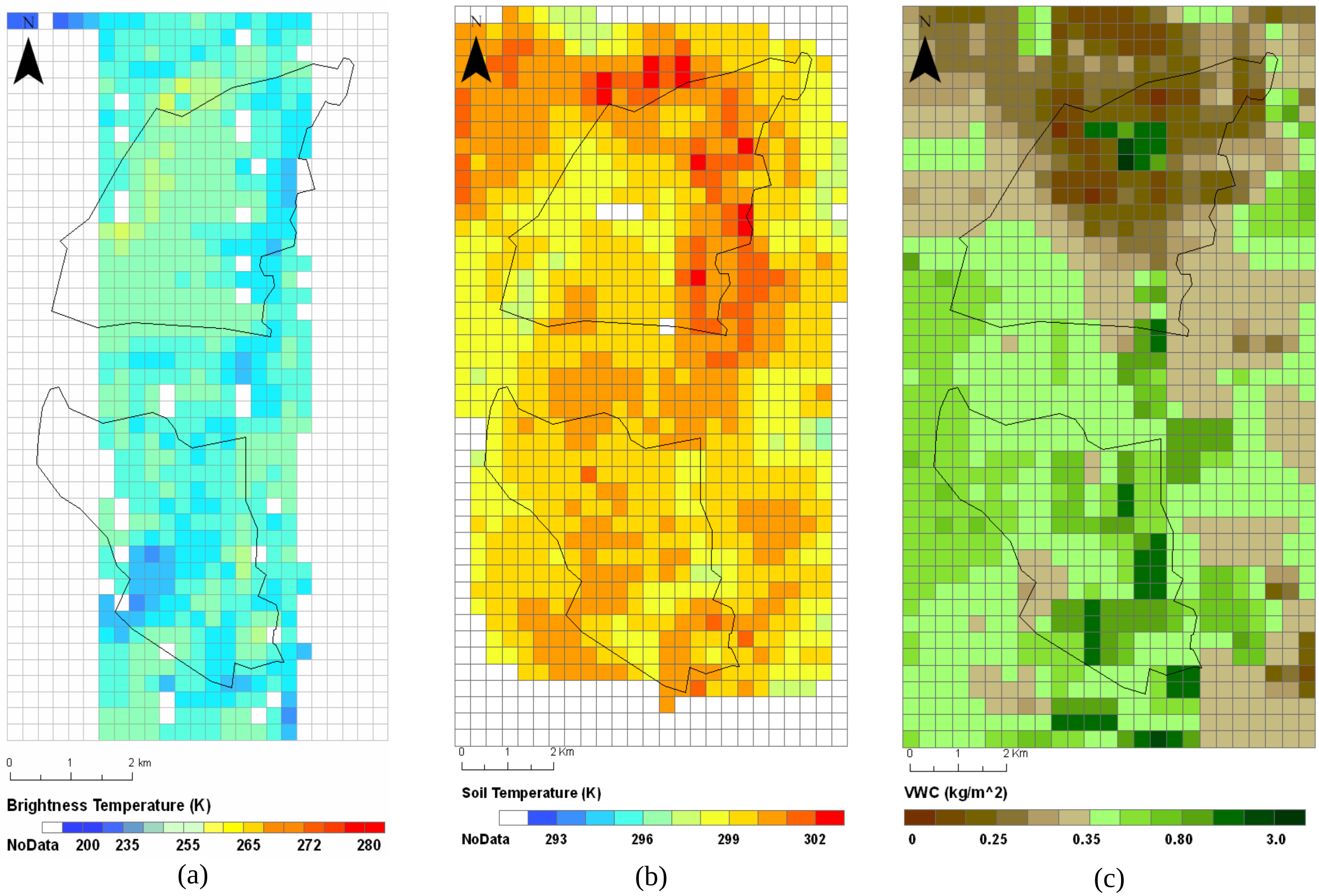

Figure A.1: 2nd November 2005, 250 m resolution: Brightness Temperature (a), Soil Temperature (b), Vegetation Water Content (c)

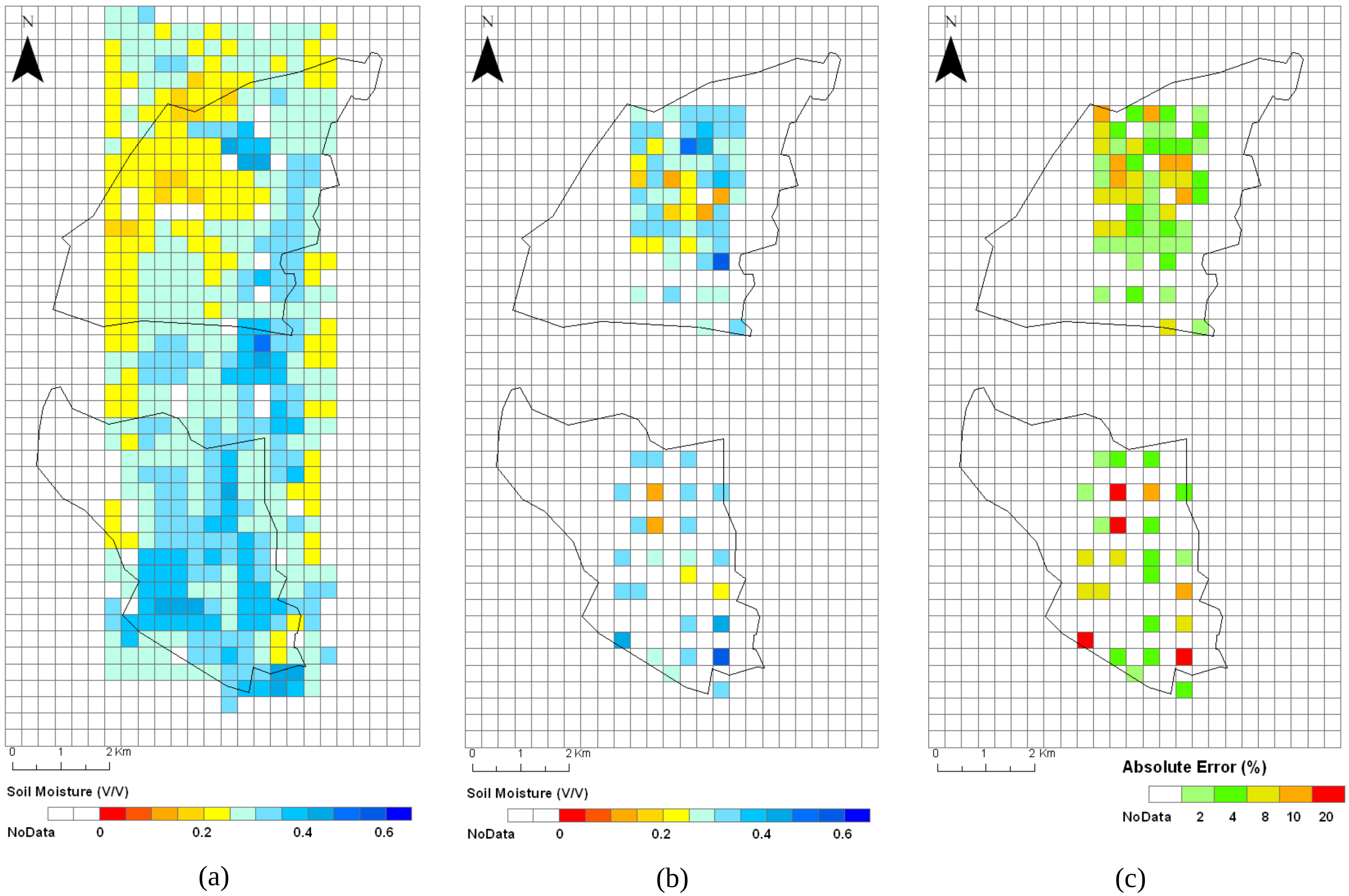

Figure A.2: 2nd November 2005, 250 m resolution: Predicted Soil Moisture (a), Ground-measured Soil Moisture (b), Absolute Error (c)

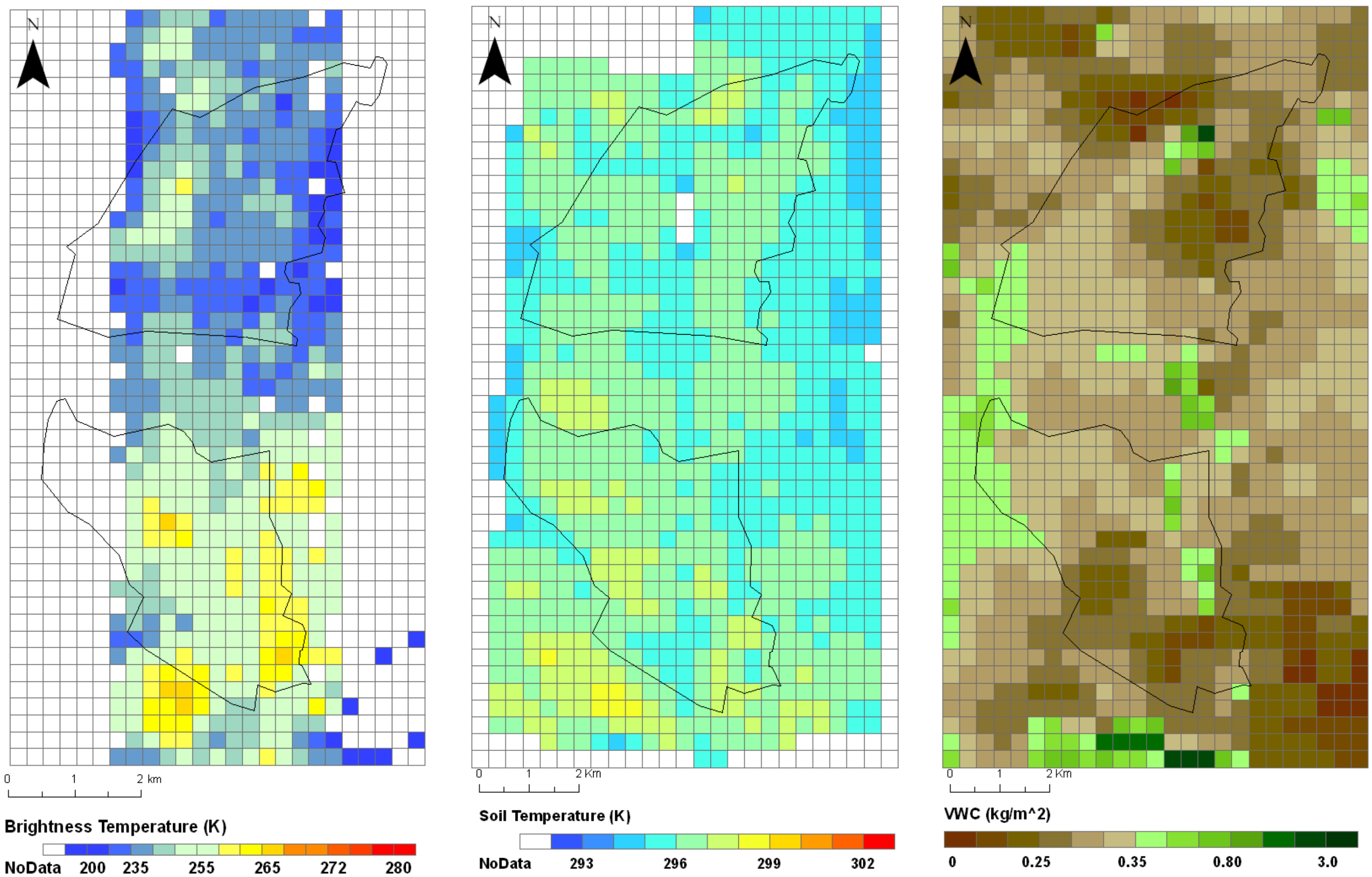

(a) (b) (c)

Figure A.3: 11th November 2005, 250 m resolution: Brightness Temperature (a), Soil Temperature (b), Vegetation Water Content (c)

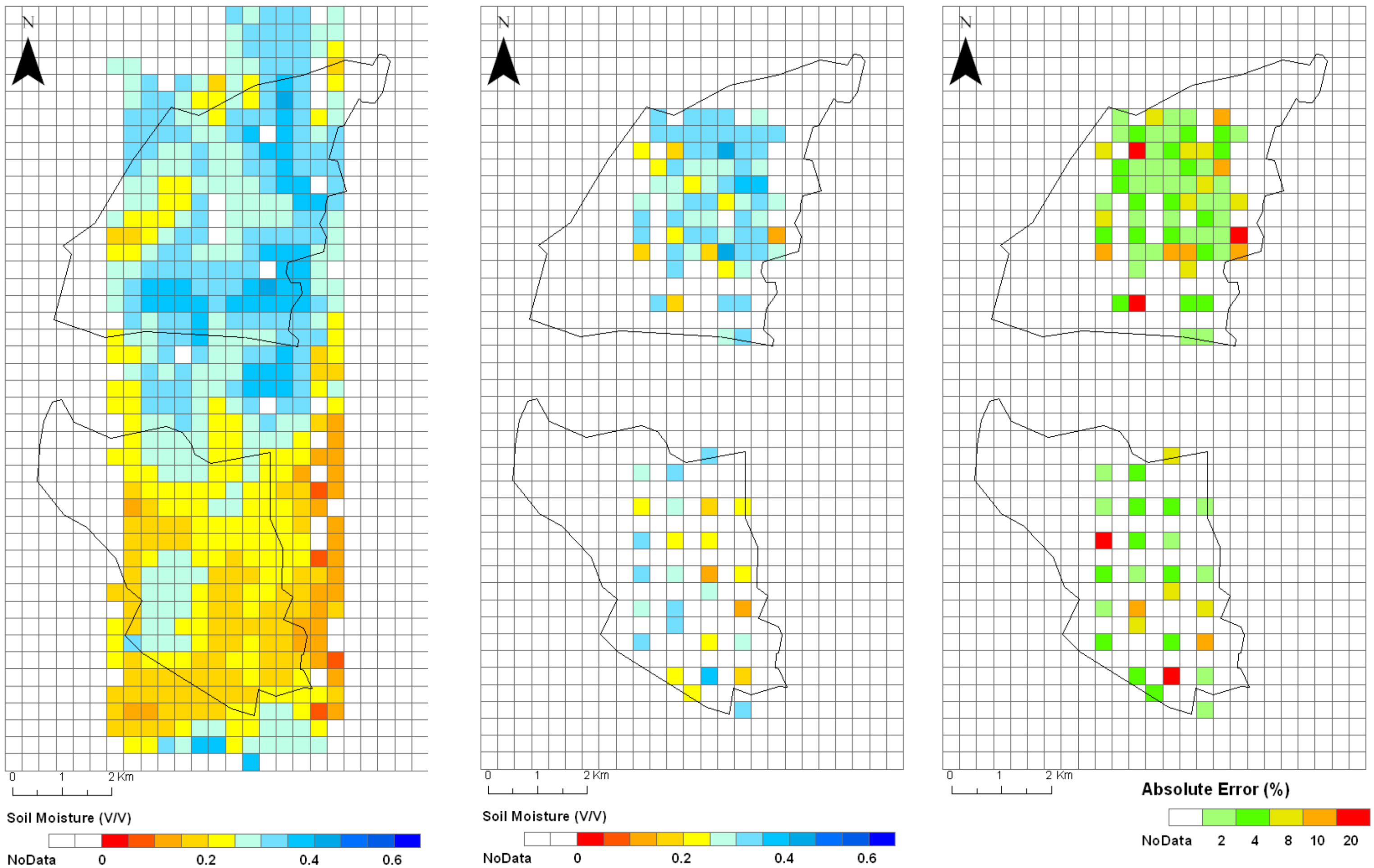

(a) (b) (c)

Figure A43: 11th November 2005, 250 m resolution: Predicted Soil Moisture (a), Ground-measured Soil Moisture (b), Absolute Error (c)

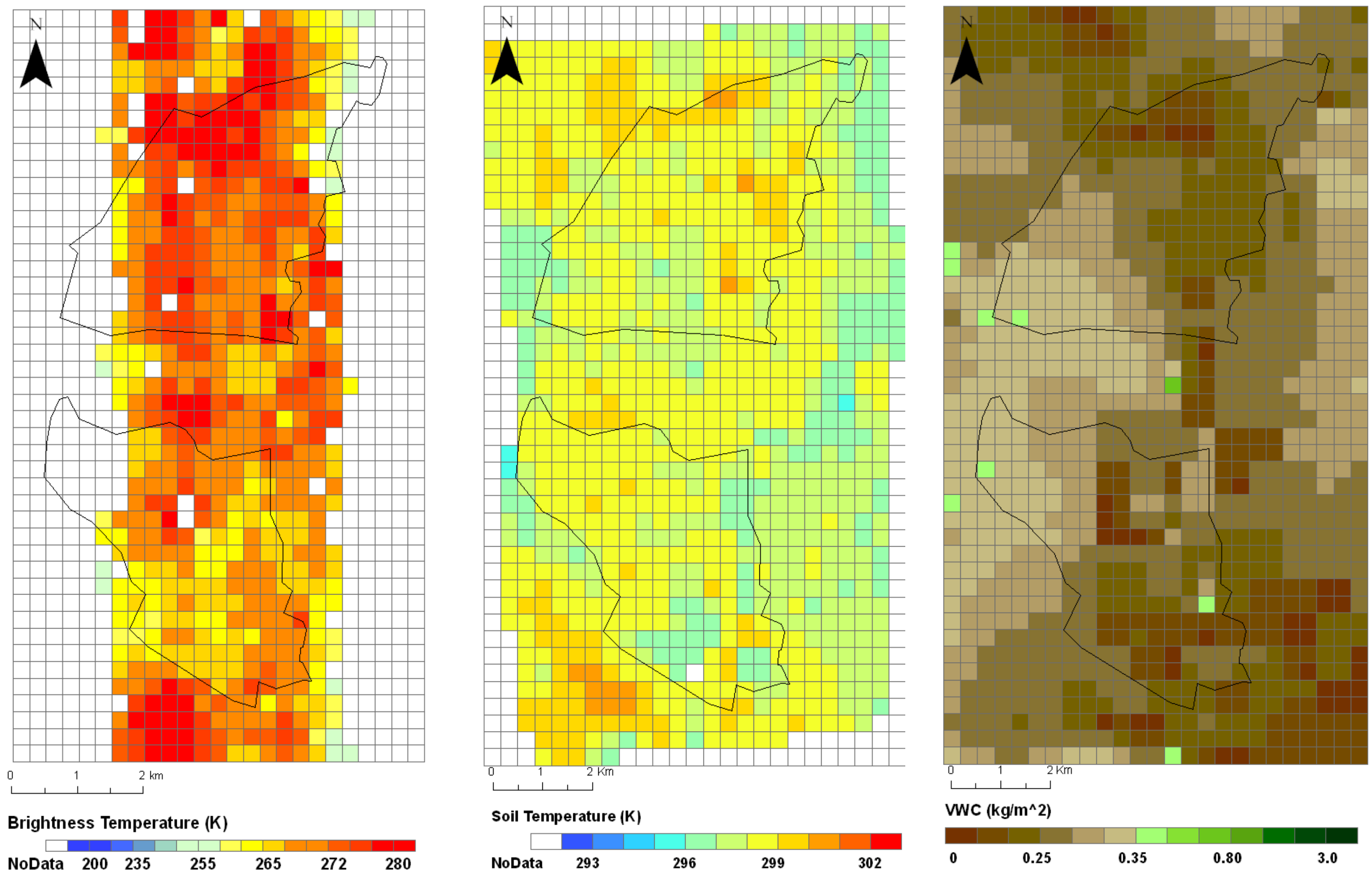

(a) (b) (c)

Figure A.5: 16th November 2005, 250 m resolution: Brightness Temperature (a), Soil Temperature (b), Vegetation Water Content (c)

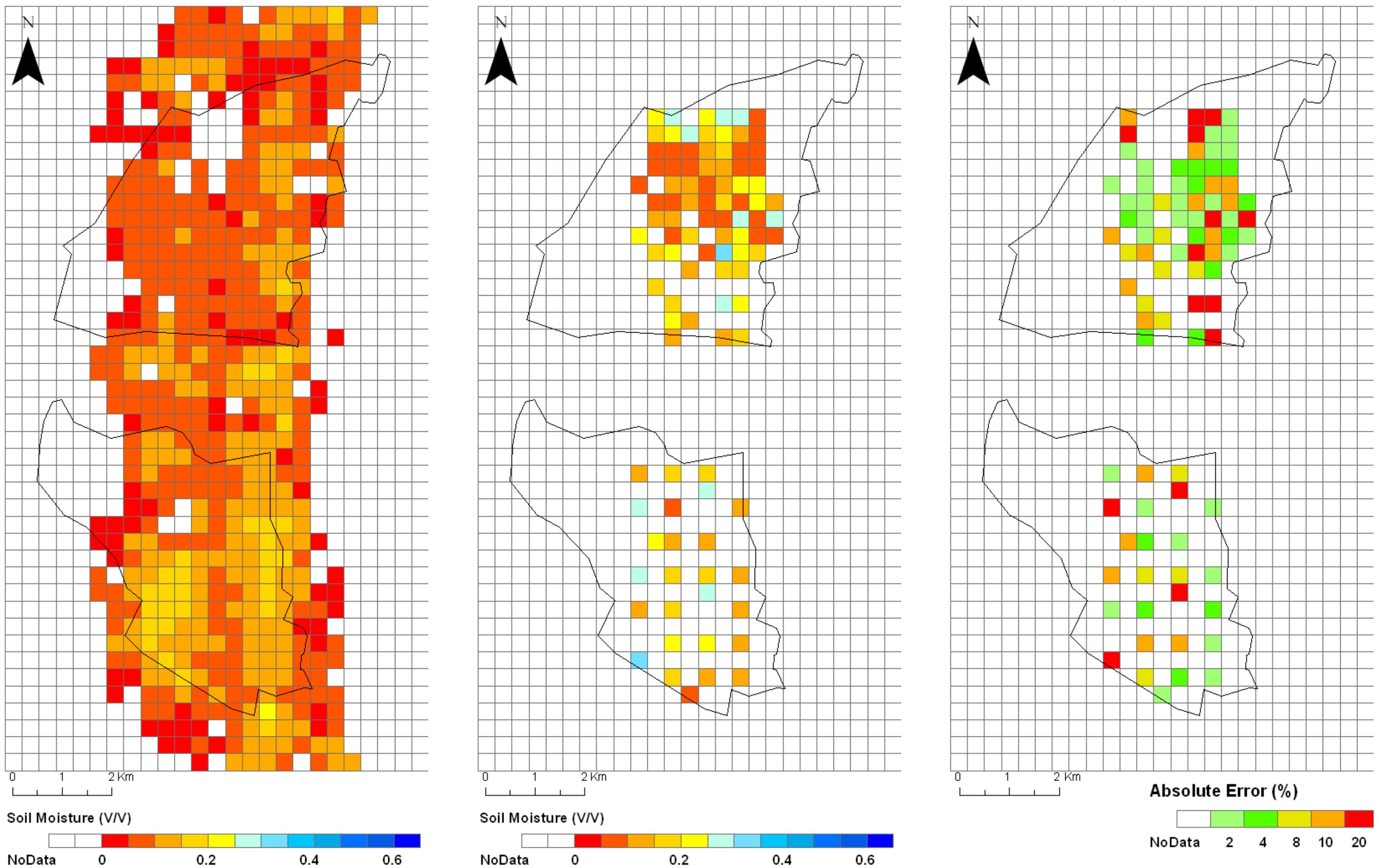

(a) (b) (c)

Figure A.6: 16th November 2005, 250 m resolution: Predicted Soil Moisture (a), Ground-measured Soil Moisture (b), Absolute Error (c)

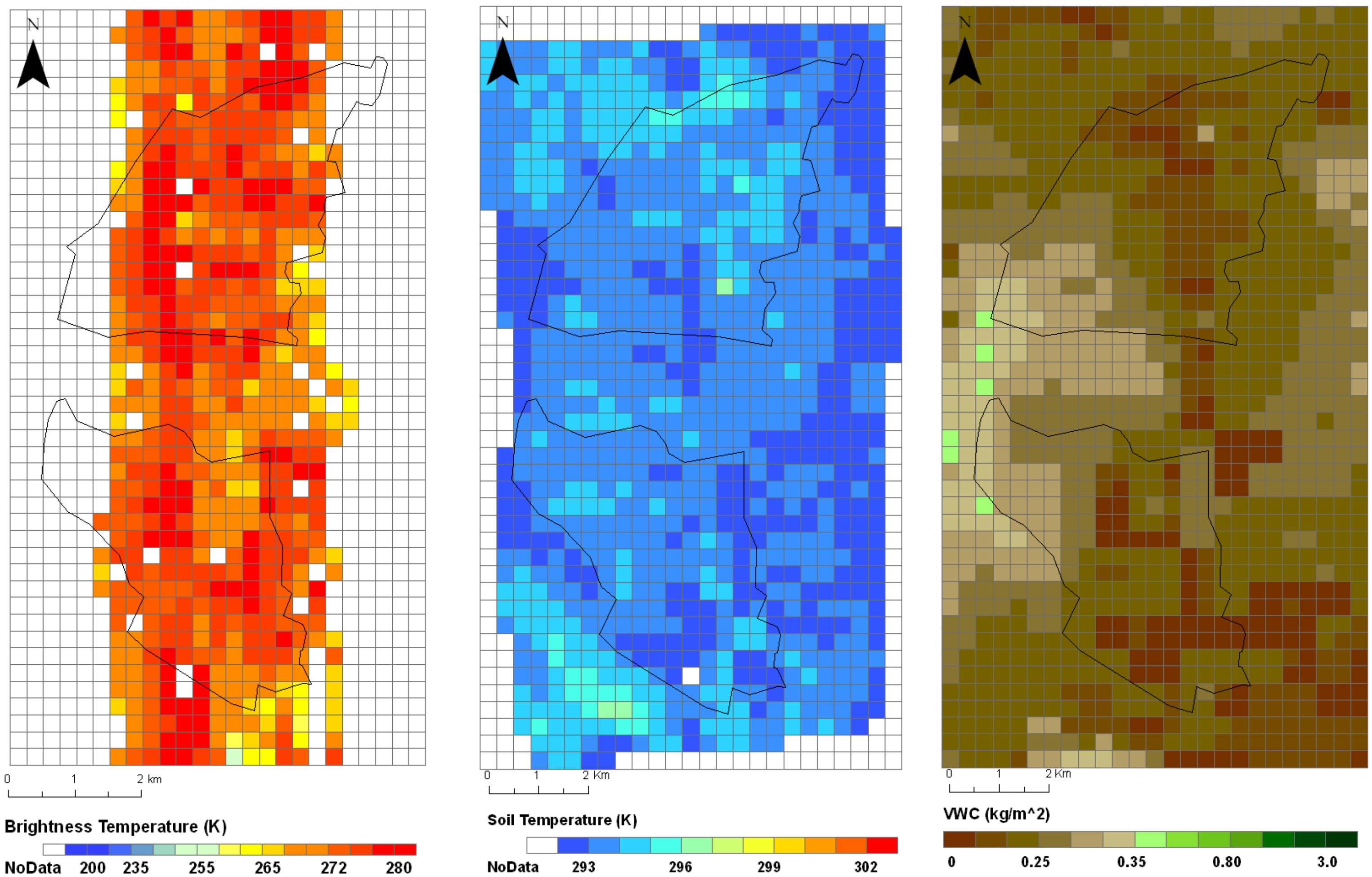

(a) (b) (c)

Figure A.7: 23rd November 2005, 250 m resolution: Brightness Temperature (a), Soil Temperature (b), Vegetation Water Content (c)

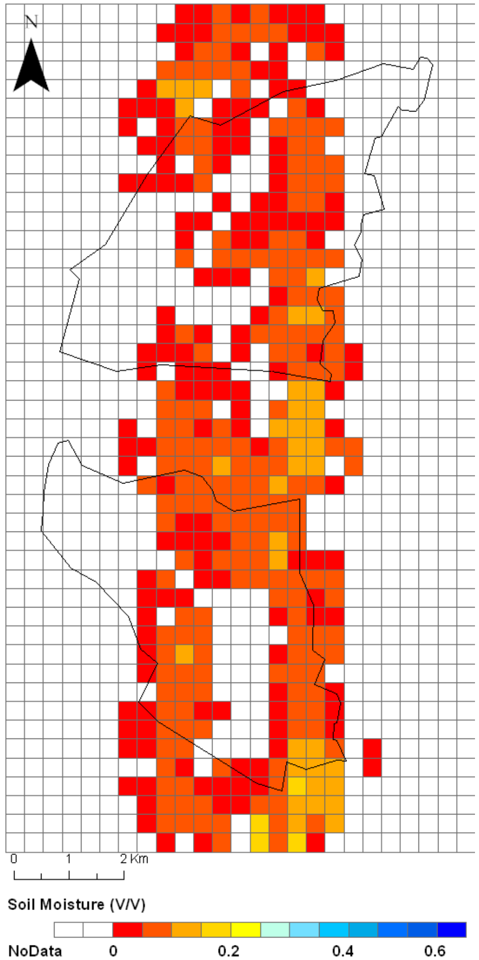

(a)

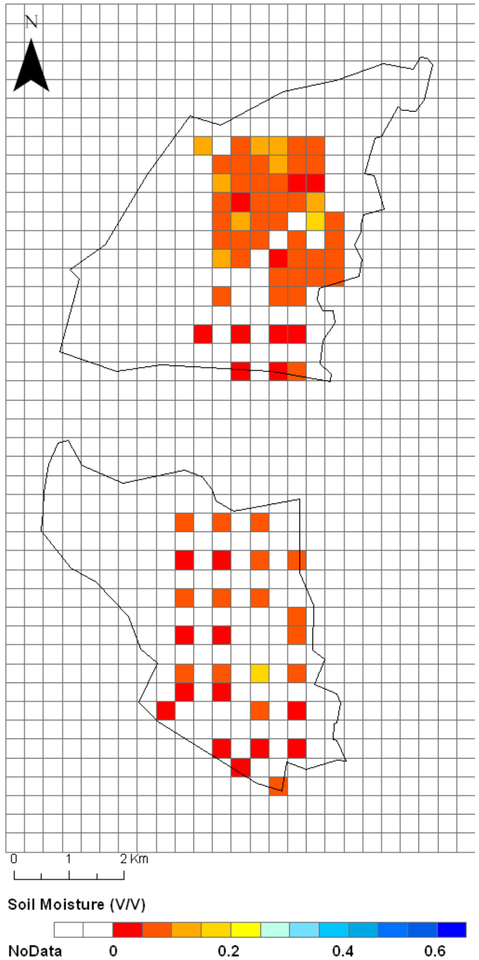

(b)

(c)

Figure A.8: 23rd November 2005, 250 m resolution: Predicted Soil Moisture (a), Ground-measured Soil Moisture (b), Absolute Error (c)

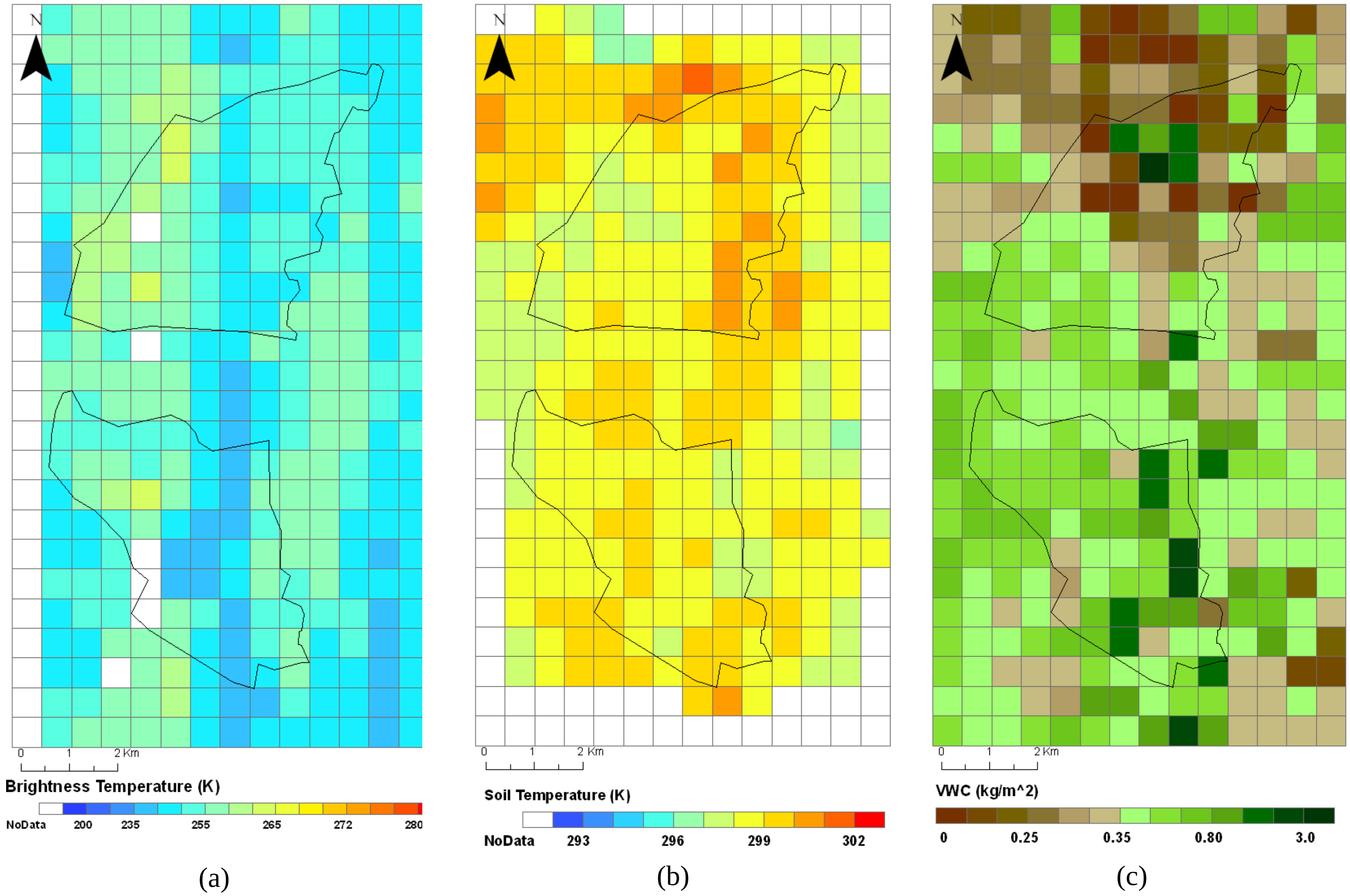

Figure A.9: 2nd November 2005, 500 m resolution: Brightness Temperature (a), Soil Temperature (b), Vegetation Water Content (c)

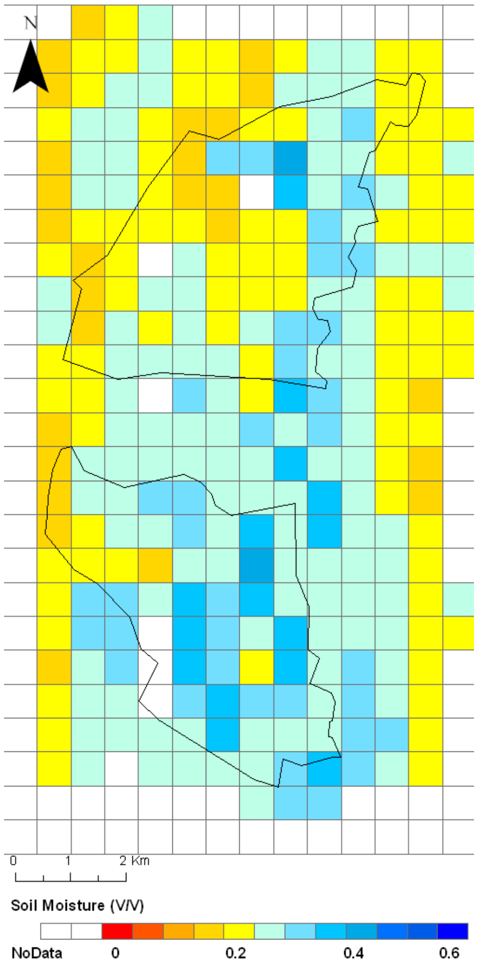

(a)

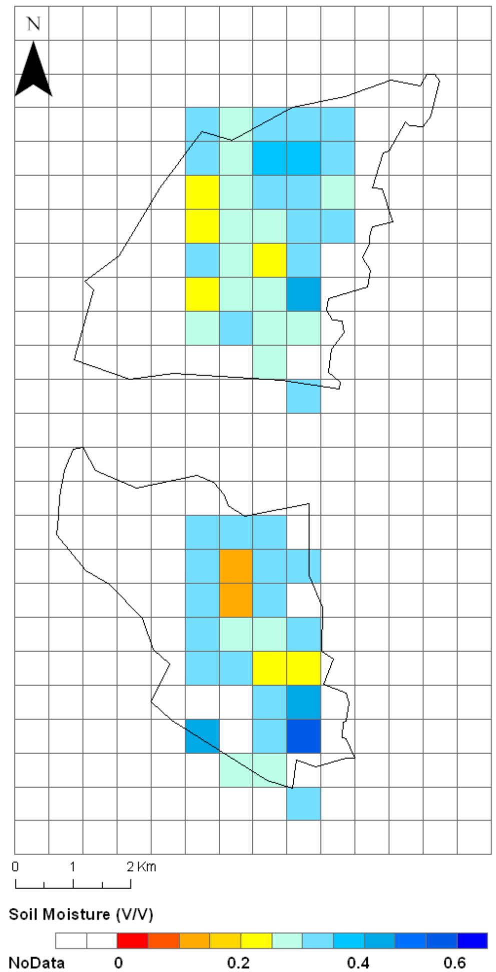

(b)

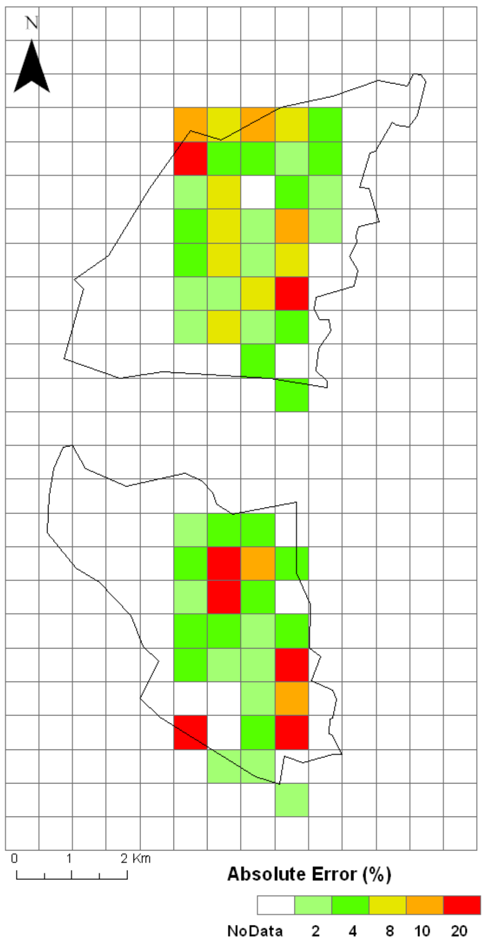

(c)

Figure A.10: 2nd November 2005, 500 m resolution: Predicted Soil Moisture (a), Ground-measured Soil Moisture (b), Absolute Error (c)

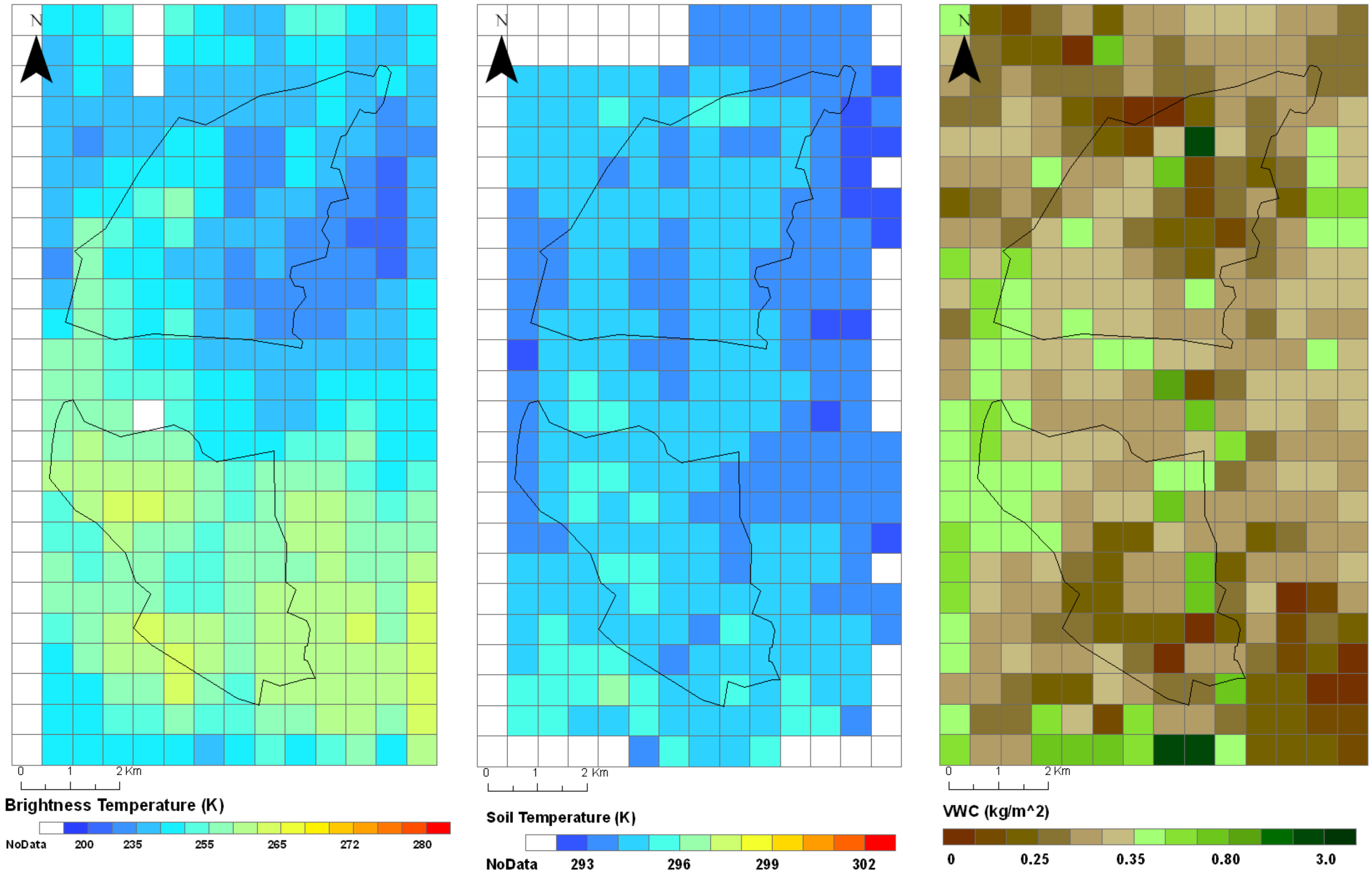

(a) (b) (c)

Figure A.11: 11th November 2005, 500 m resolution: Brightness Temperature (a), Soil Temperature (b), Vegetation Water Content (c)

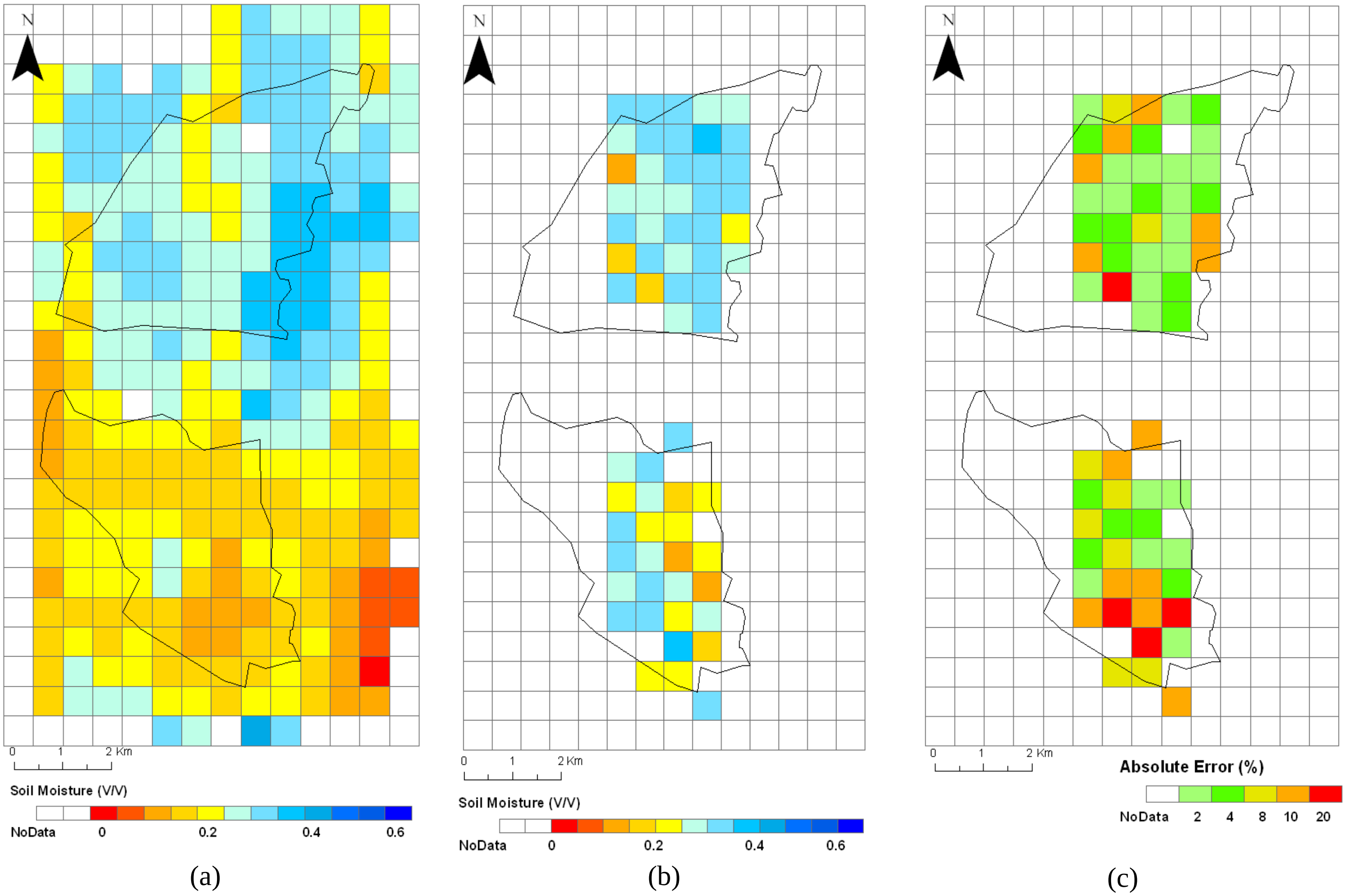

Figure A.12: 11th November 2005, 500 m resolution: Predicted Soil Moisture (a), Ground-measured Soil Moisture (b), Absolute Error (c)

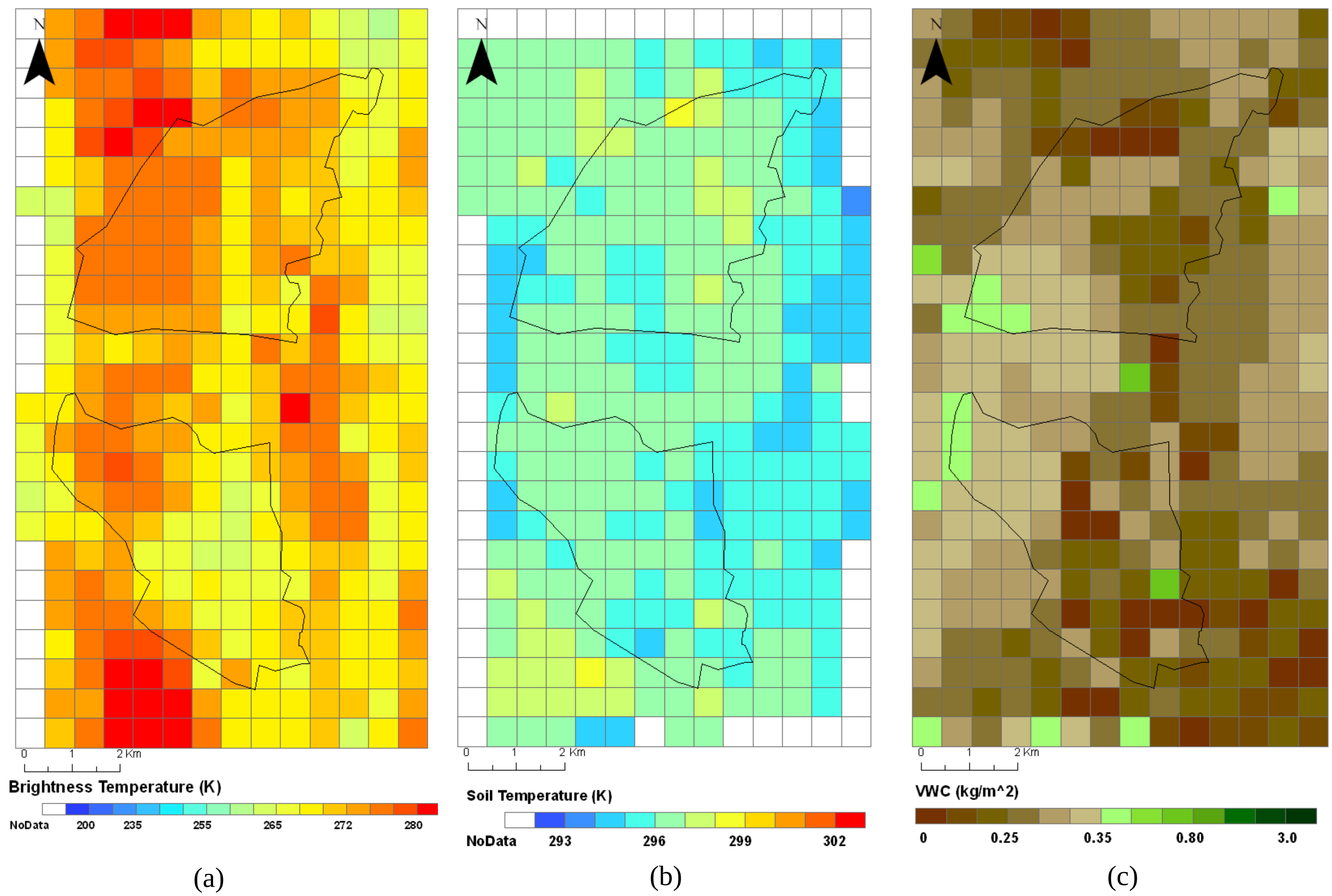

Figure A.13: 16th November 2005, 500 m resolution: Brightness Temperature (a), Soil Temperature (b), Vegetation Water Content (c)

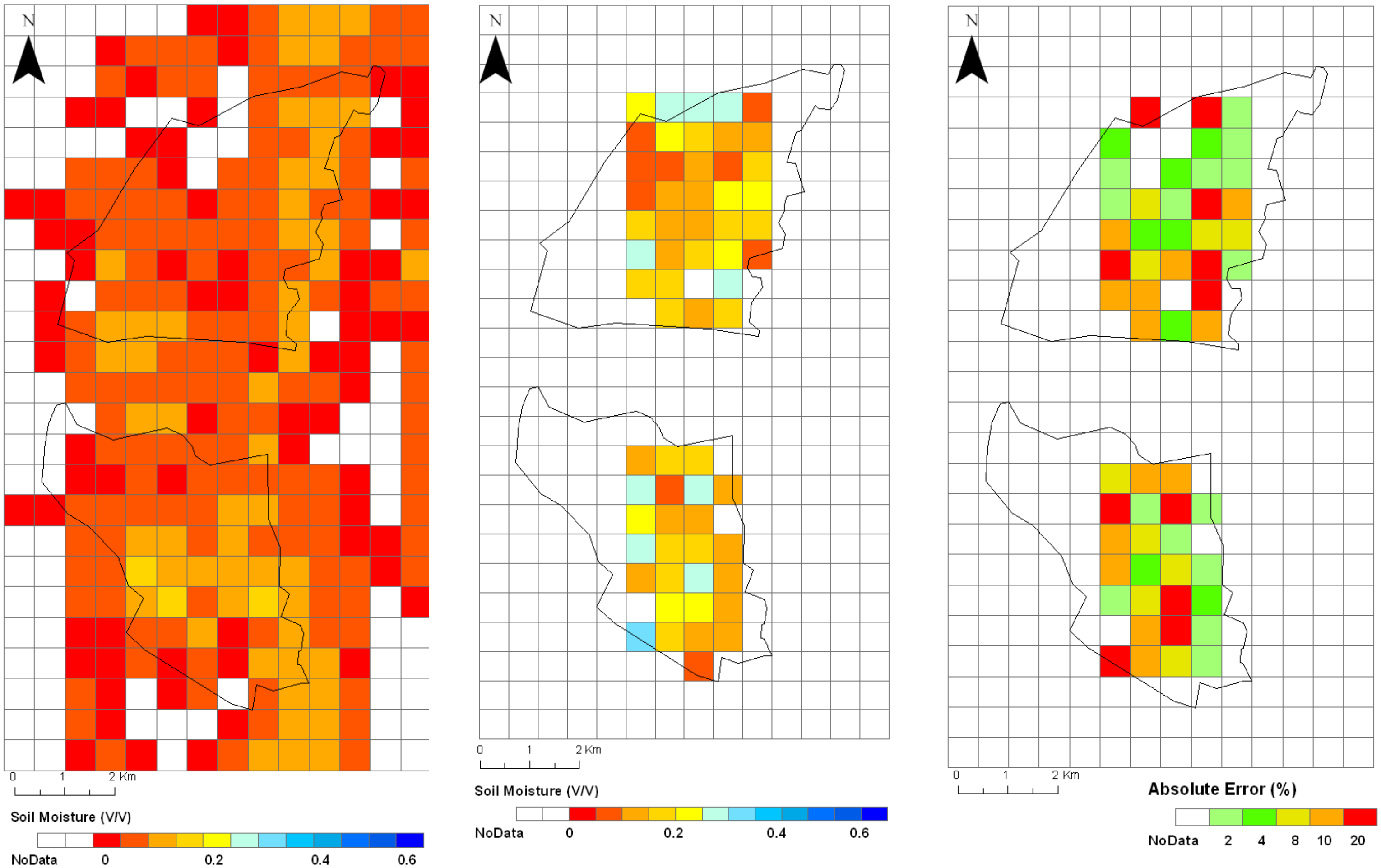

(a) (b) (c)

Figure A.14: 16th November 2005, 500 m resolution: Predicted Soil Moisture (a), Ground-measured Soil Moisture (b), Absolute Error (c)

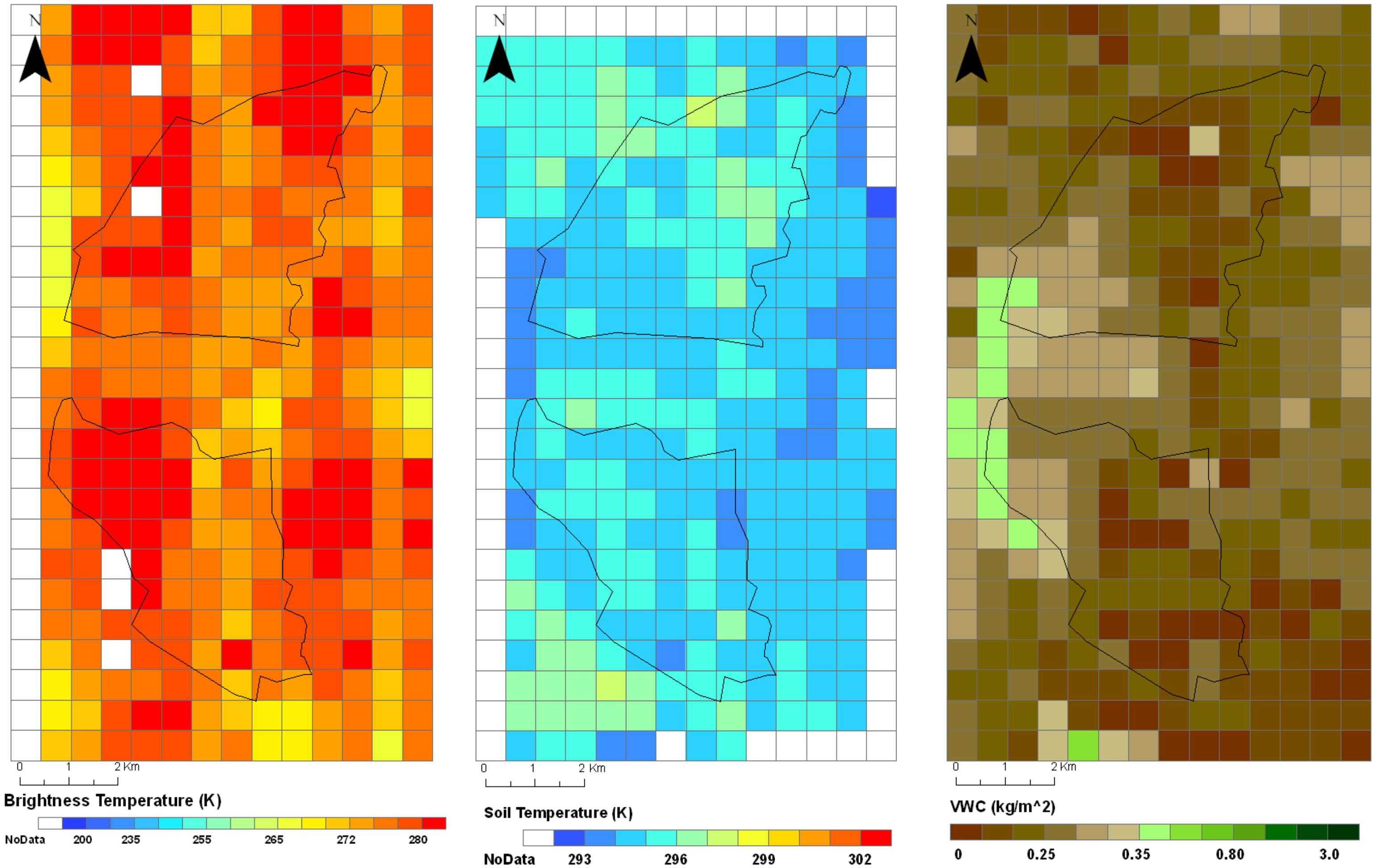

(a) (b) (c)

Figure A.15: 23rd November 2005, 500 m resolution: Brightness Temperature (a), Soil Temperature (b), Vegetation Water Content (c)

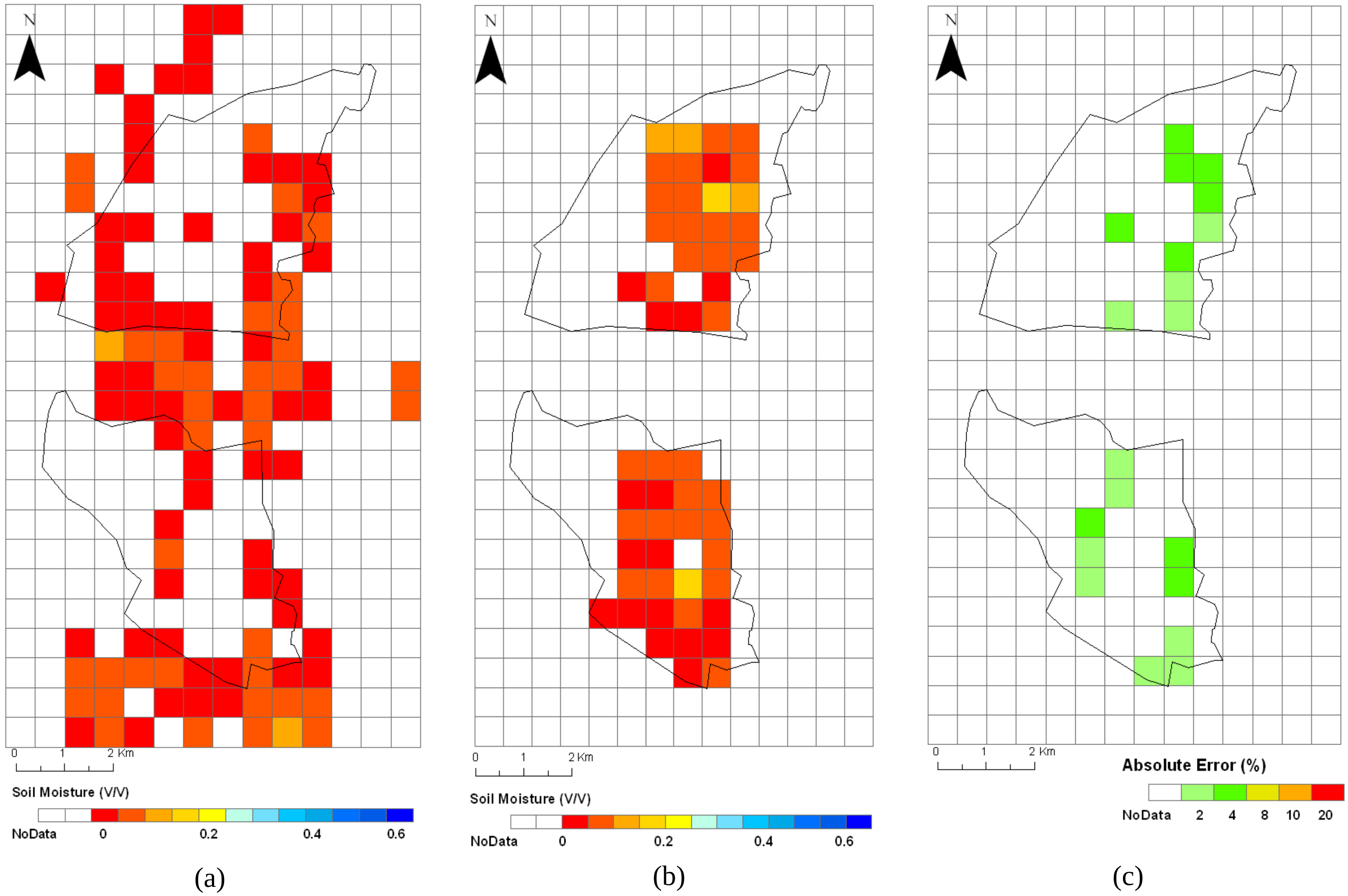

Figure A.16: 23rd November 2005, 500 m resolution: Predicted Soil Moisture (a), Ground-measured Soil Moisture (b), Absolute Error (c)

APPENDIX B

FLIGHT LINES

Appendix B shows the flight lines over the Merriwa Area where the Midlothian farm is located. These flights have been performed twice a week at 2500ft and 5000ft altitude during the NAFE 05 campaign. It can be noticed that for both the flights, the Midlothian farm data have been collected in two lines.

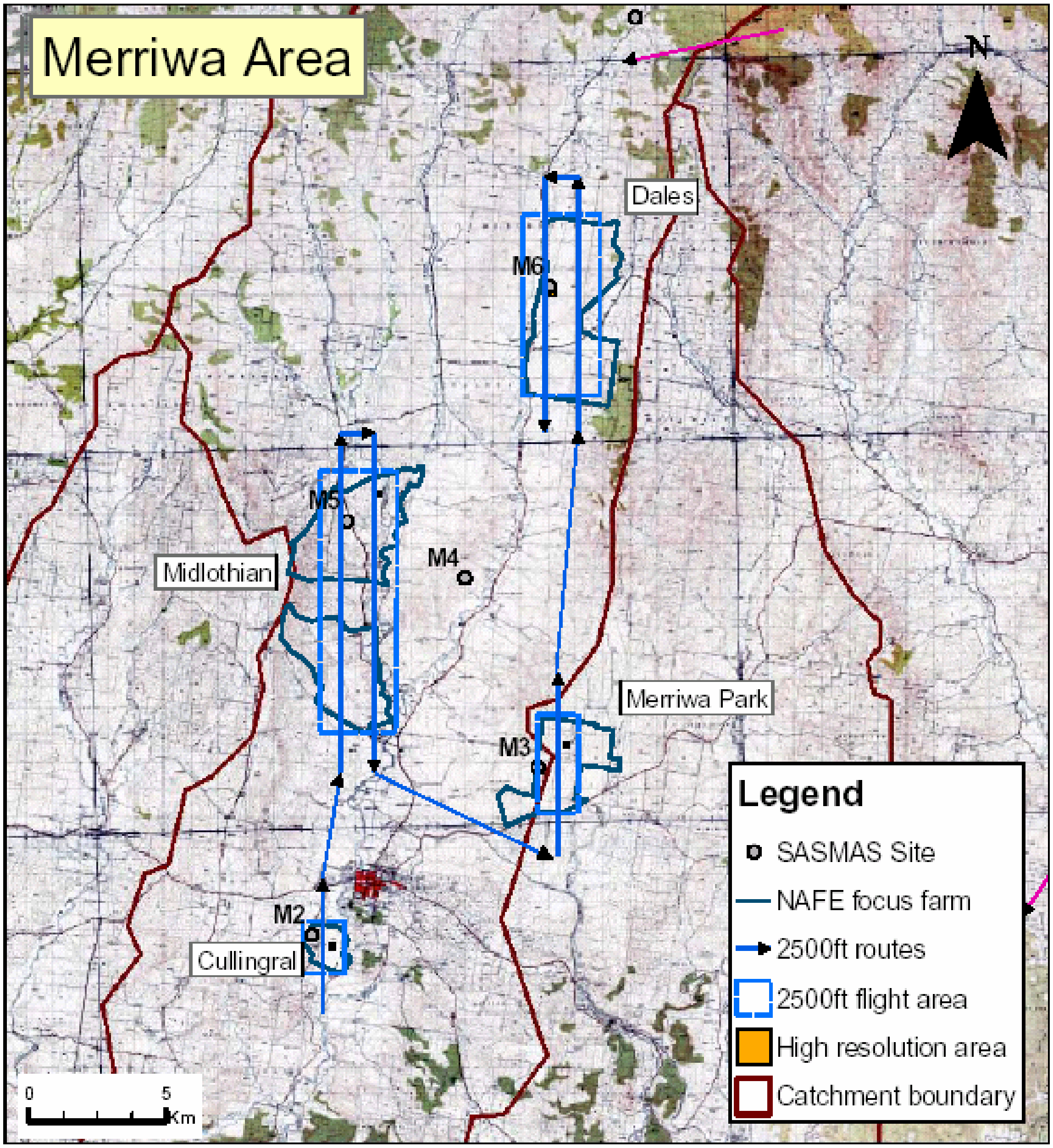

Figure B.1: Flight lines at 2500ft altitude over the Merriwa area

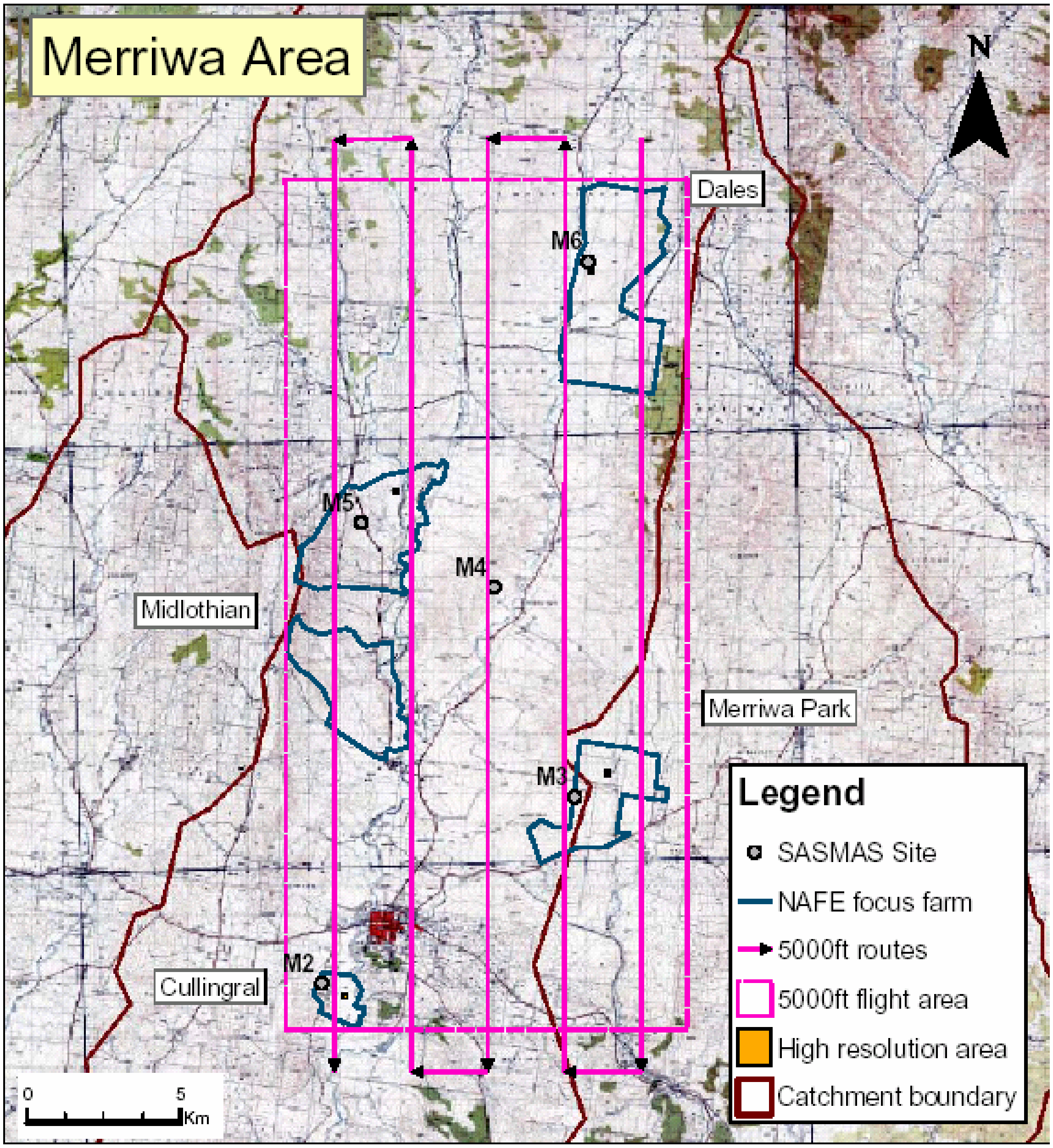

Figure B.2: Flight lines at 5000ft altitude over the Merriwa area

APPENDIX C

VEGETATION DATA

Appendix C shows graphs of ground vegetation data collected during the field campaign NAFE 2005.

Figure C.1 illustrates vegetation dry biomass values during the period of the field campaign in the Krui Catchment: some statistics of these data, as the median, the minimum and the maximum values of dry biomass and in some cases also the 25^{th}, 75^{th} percentiles are displayed for each farm.

Figure C.2 illustrates values of vegetation water content, calculated from wet and dry vegetation biomass of samples collected in the farms of Stanley, Roscommon, Cullingral and Merriwa Park for the month of November.

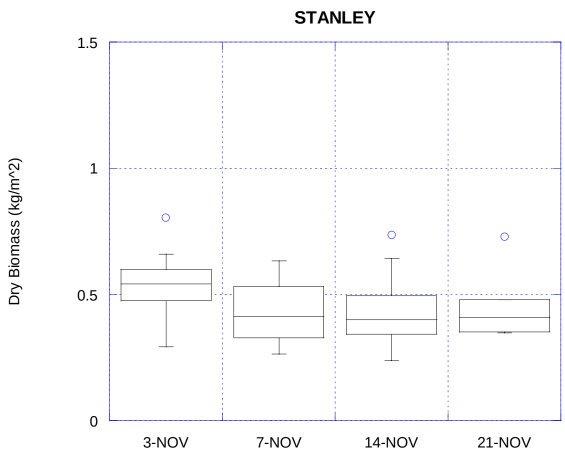

(a)

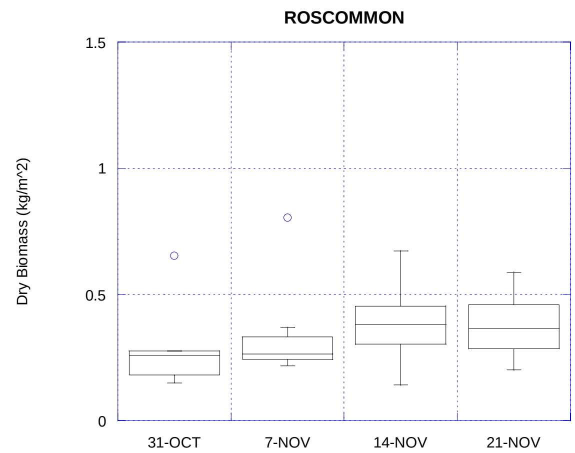

(b)

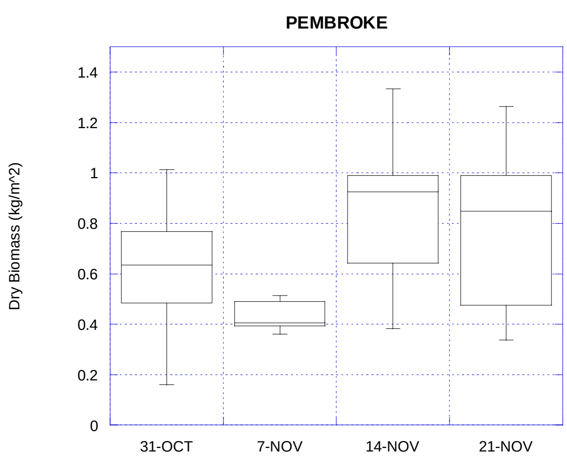

(c)

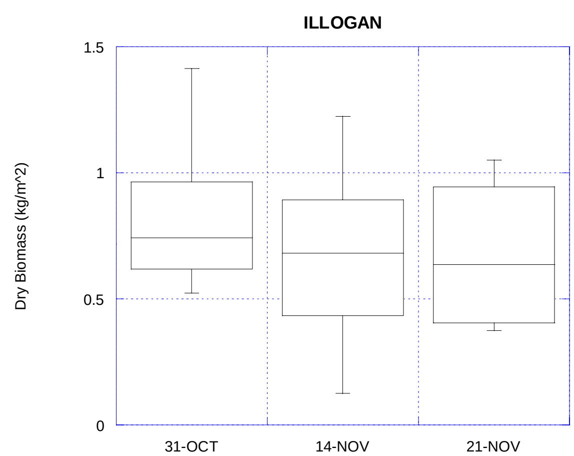

(d)

Figure C.1: Dry Biomass measured during the month of November 2005 at the farms of Stanley (a), Roscommon (b), Pembroke (c) and Illogan (d).

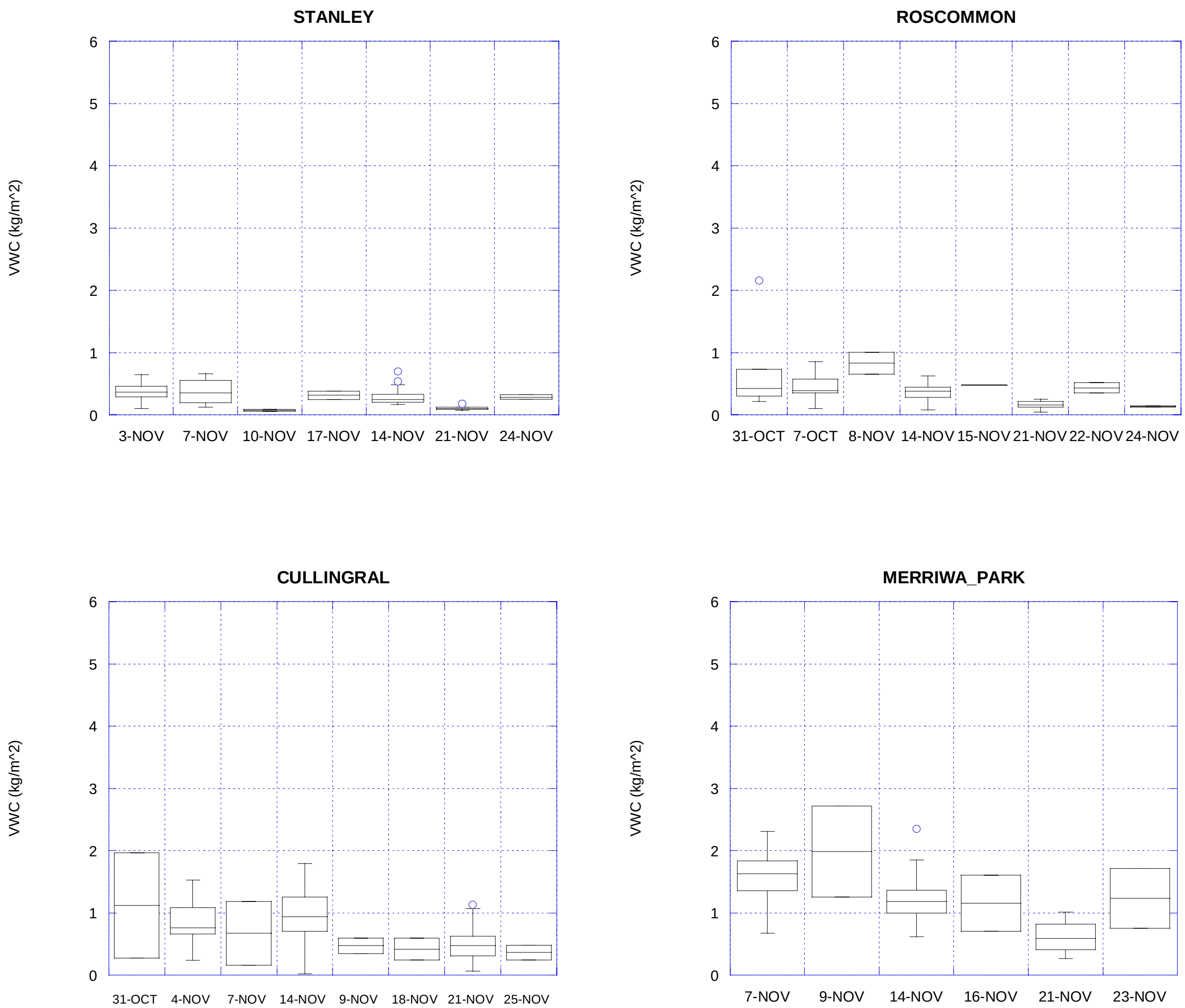

Figure C.2: Vegetation water content measured during the month of November 2005 for the farms of Stanley (a), Roscommon (b), Cullingral (c) and Merriwa Park (d).

APPENDIX C

VEGETATION DATA

Appendix C shows graphs of ground vegetation data collected during the field campaign NAFE 2005.

Figure C.1 illustrates vegetation dry biomass values during the period of the field campaign in the Krui Catchment: some statistics of these data, as the median, the minimum and the maximum values of dry biomass and in some cases also the 25^{th}, 75^{th} percentiles are displayed for each farm.

Figure C.2 illustrates values of vegetation water content, calculated from wet and dry vegetation biomass of samples collected in the farms of Stanley, Roscommon, Cullingral and Merriwa Park for the month of November.

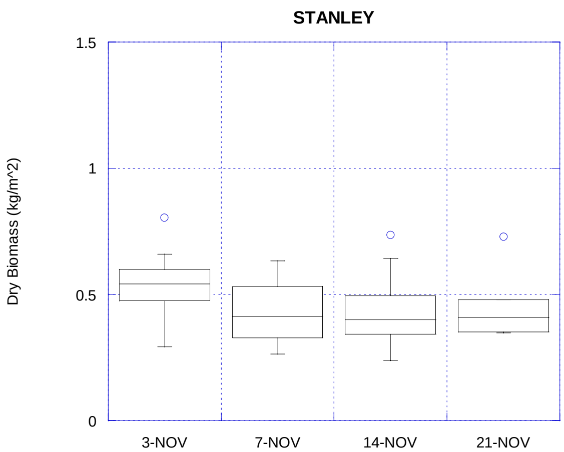

(a)

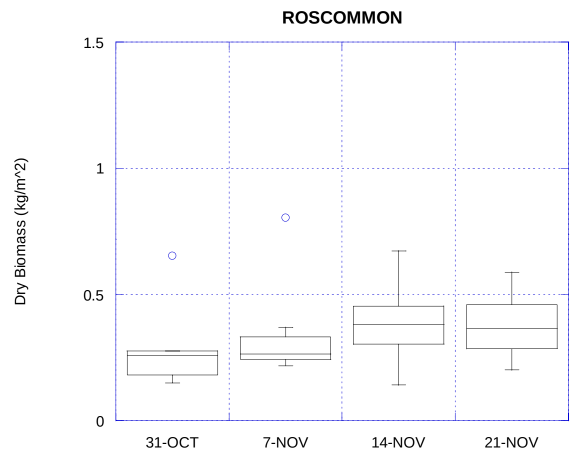

(b)

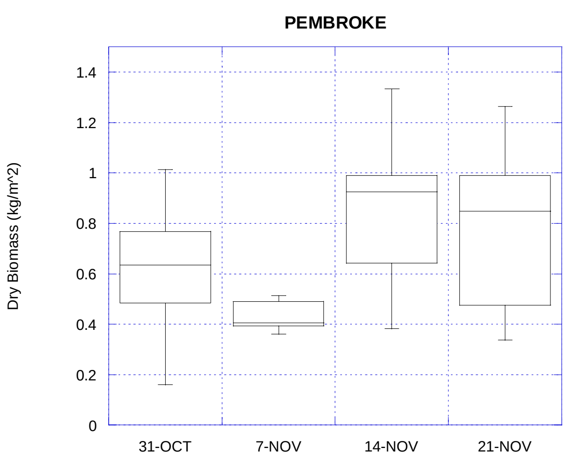

(c)

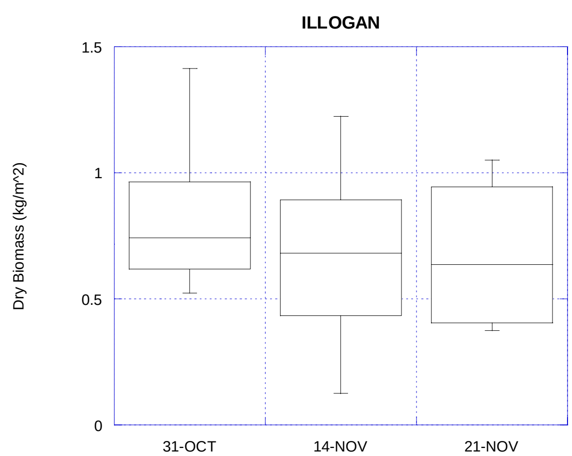

(d)

Figure C.1: Dry Biomass measured during the month of November 2005 at the farms of Stanley (a), Roscommon (b), Pembroke (c) and Illogan (d).

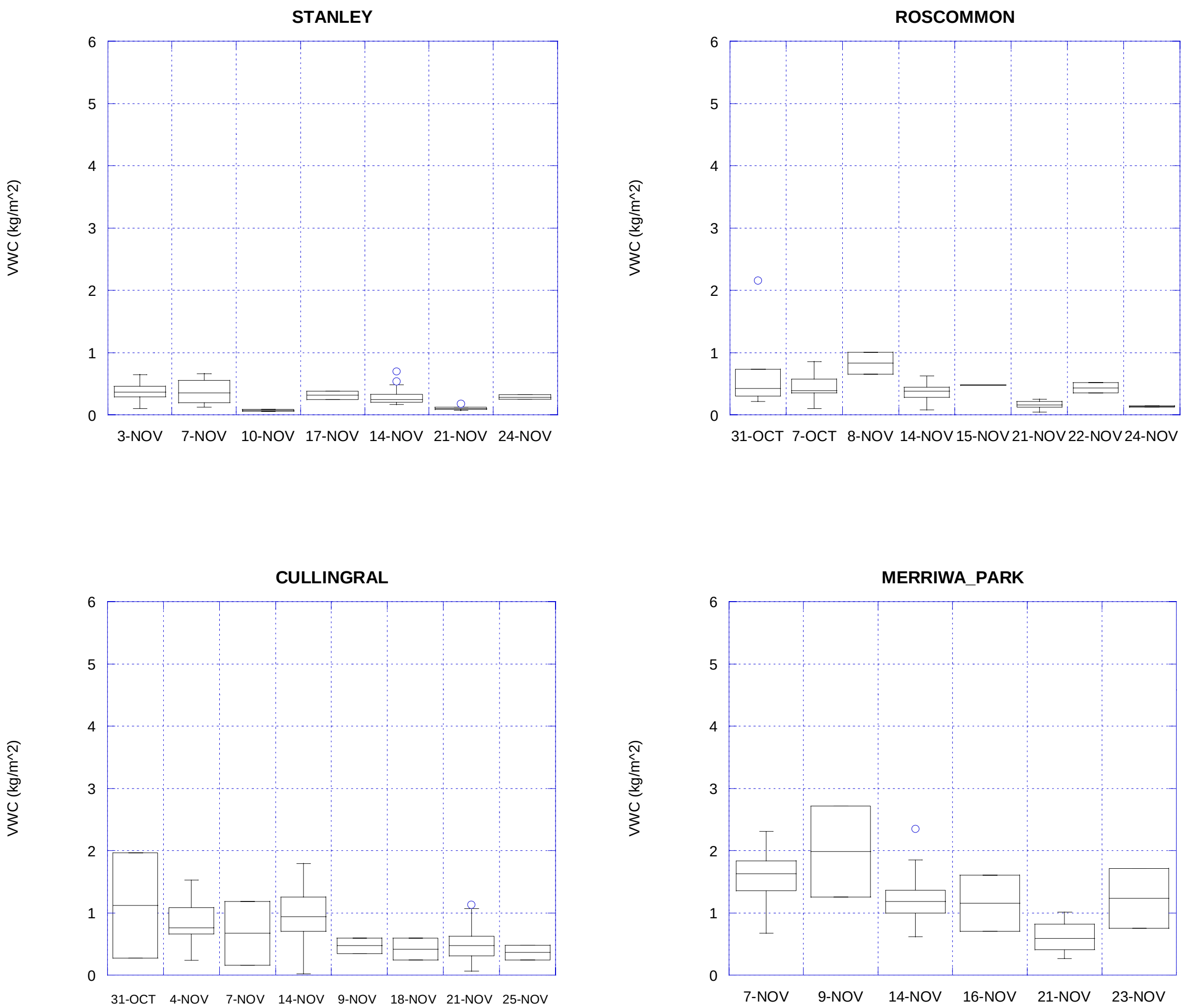

Figure C.2: Vegetation water content measured during the month of November 2005 for the farms of Stanley (a), Roscommon (b), Cullingral (c) and Merriwa Park (d).

APPENDIX D

INCIDENCE ANGLE

Appendix D shows maps of the incidence angles for the two proposed resolutions (250m in Fig. D1 and 500m in Fig. D2) and for the period of the field campaign.

These maps have been obtained following the same procedure described in Chapter 7 to obtain brightness temperature maps.

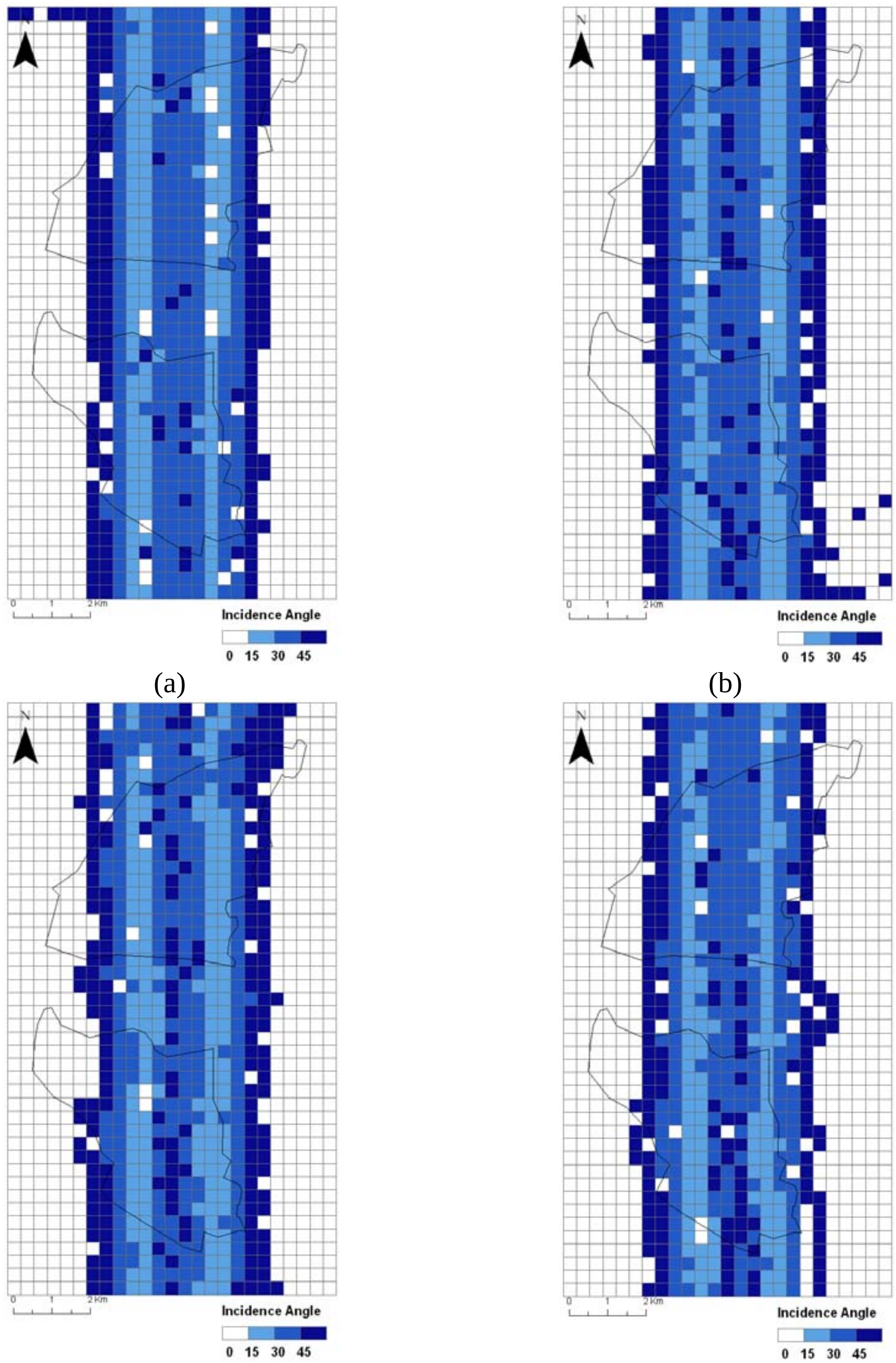

Figure D.1: Incidence angles of the 2500ft flights over the farm of Midlothian on November 2 (a), November 11 (b), November 16 (c) and November 23 (d).

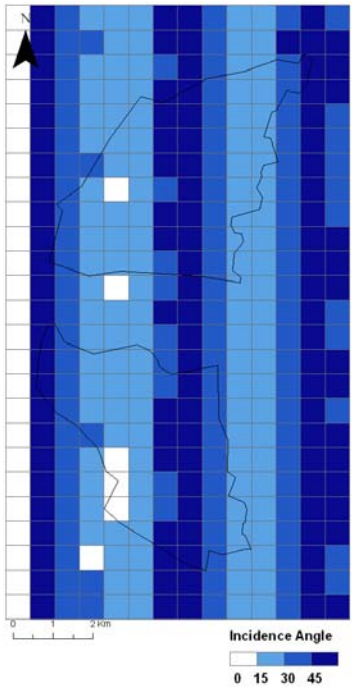

(a)

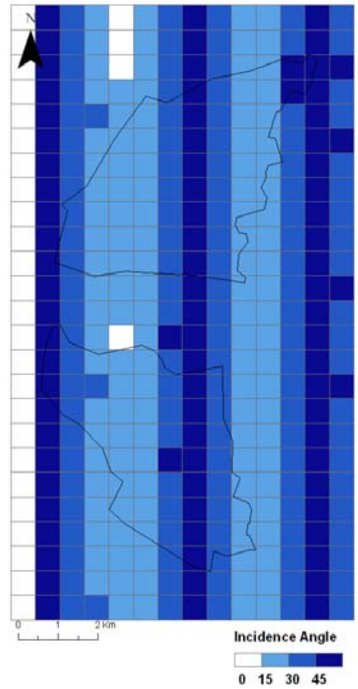

(b)

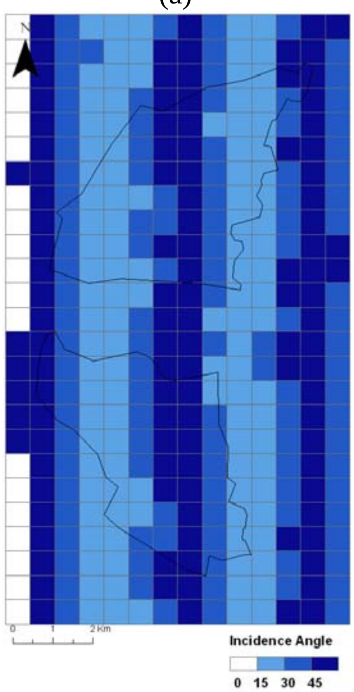

(c)

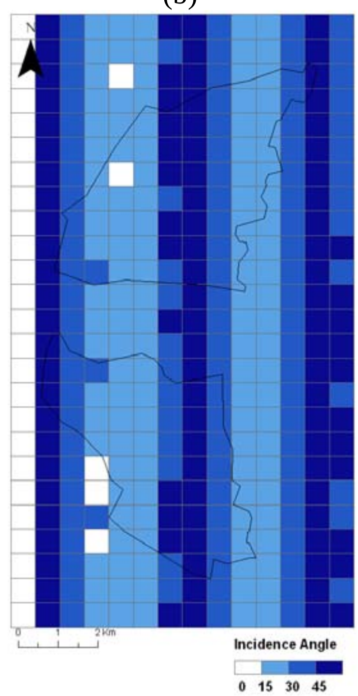

(d)

Figure D.2: Incidence angles of the 5000ft flights over the farm of Midlothian on November 2 (a), November 11 (b), November 16 (c) and November 23 (d).

APPENDIX E

SOIL TEMPERATURE

Appendix E shows the rough data of temperature collected at the four stations with thermal infrared devices and thermometers in the ground.

The malfunctioning occurred some days during the field campaign can be noticed, especially at the farms of Midlothian (Fig. E3) and Stanley (Fig. E4). The stations placed at the farms of Illogan (Fig. E1) and Merriwa Park (Fig, E2) recorded data successfully almost for the whole month of November.

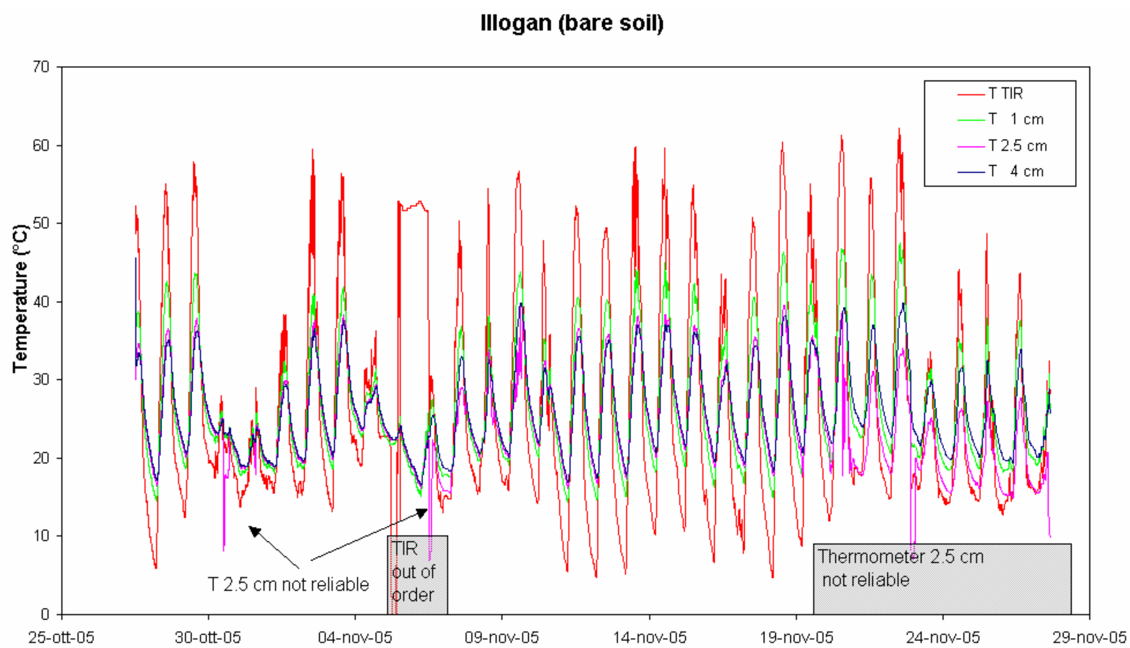

Figure E.1: Temperature data collected at the Illogan farm (land cover: bare soil)

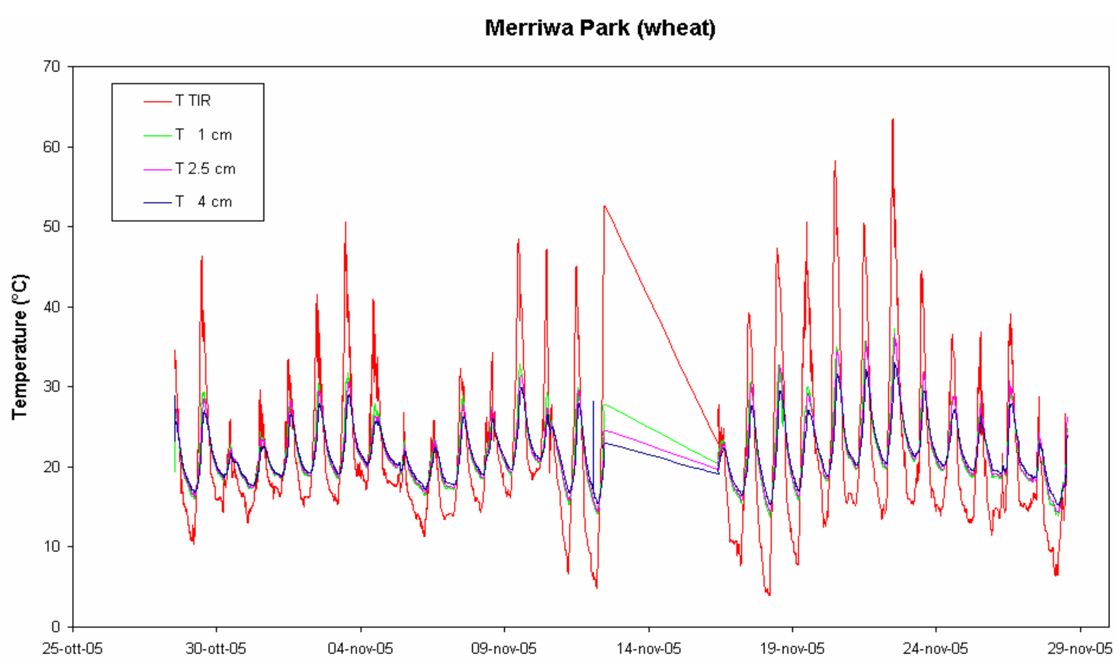

Figure E.2: Temperature data collected at the Merriwa Park farm (land cover: wheat)

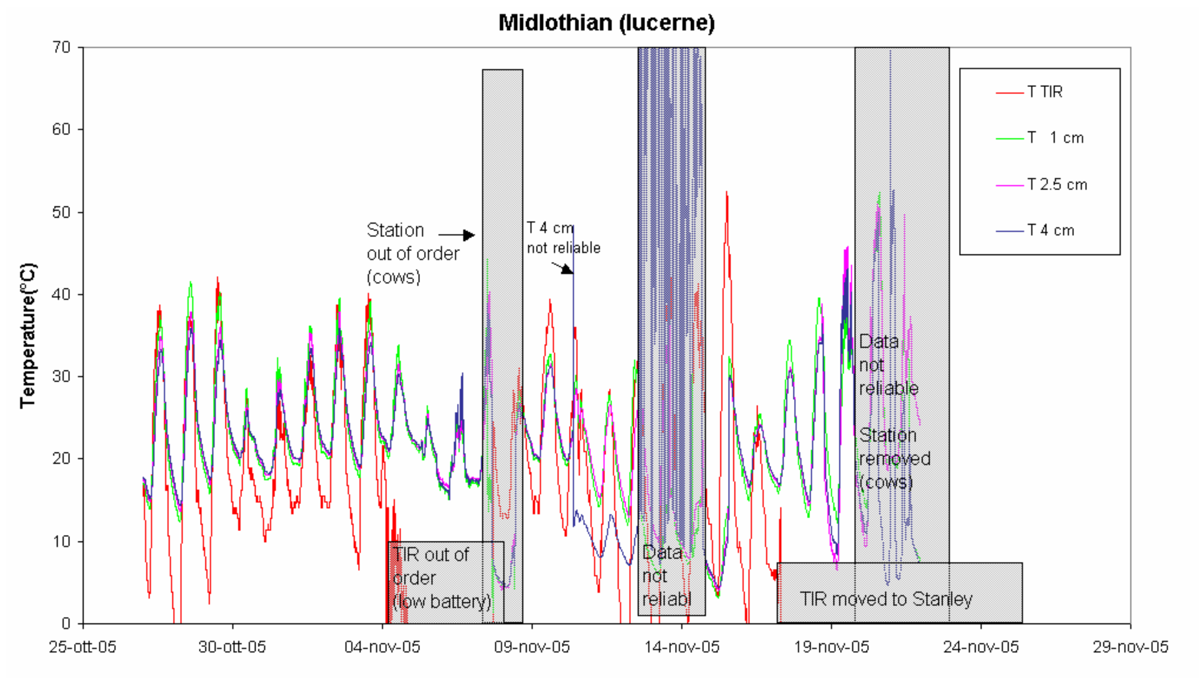

Figure E.3: Temperature data collected at the Midlothian farm (land cover: lucerne)

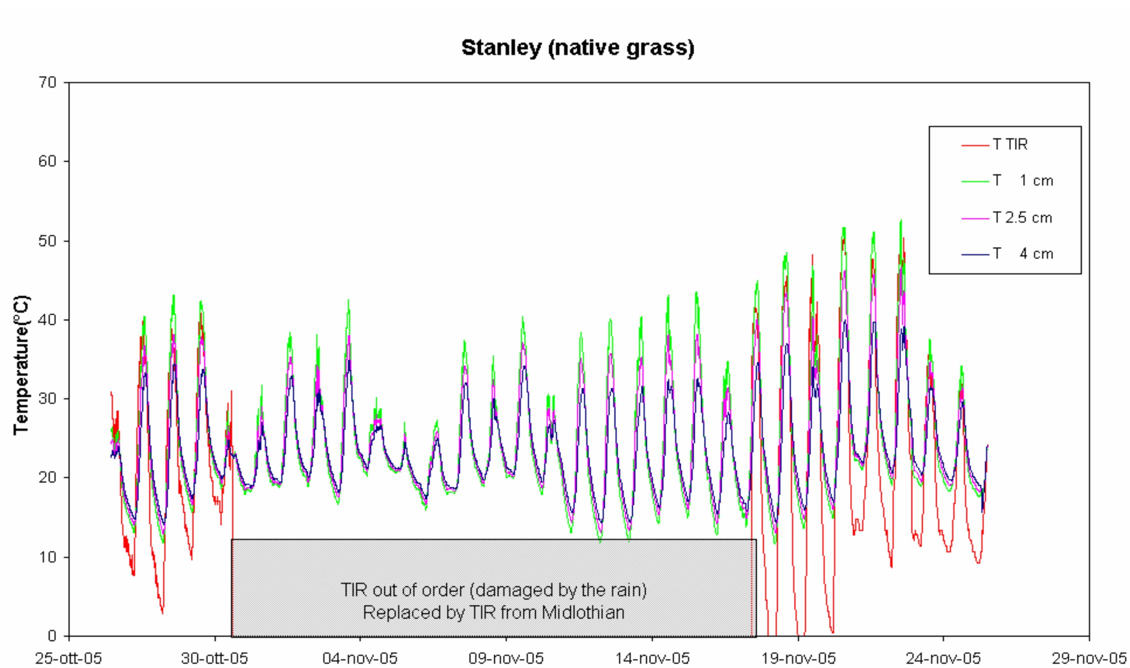

Figure E.4: Temperature data collected at the Stanley farm (land cover: native grass)